Antiferromagnetic quantum phase transitions:
continuous tuning and direct probes of competing states

Thesis by
Yishu Wang

In Partial Fulfillment of the Requirements for the
Degree of
Doctor of Philosophy in Physics

Caltech

CALIFORNIA INSTITUTE OF TECHNOLOGY
Pasadena, California

2018
Defended May 3, 2018

ACKNOWLEDGEMENTS

Looking back at the five years of my graduate school, I feel blessed to have been nurtured in an environment full of wisdom and virtue. From Chicago to Pasadena, the two prominent institutes together with people I met have shaped me intellectually and spiritually. Finally, I come to where I am today, with deep respect for the past and endless courage for the future.

I am most grateful to my Ph. D. advisor Prof. Thomas Rosenbaum, a great scientist and educator and the best advisor one could ever expect. His research philosophy and scientific insights always set a high standard of good science for me to pursue. His patience and appreciation allowed me freedom to explore the unknown, while he was always there to provide sharp guidance and warm encouragement when I was frustrated. His firm support continuously raised me up to more than I could have been and reinforced my pursuit for a career in research. Most profoundly, his passion towards science and education will remain a lifelong inspiration, and I hope to pass it down.

I am indebted to my best partner, Prof. Yejun Feng, without whom my years in graduate school wouldn't have been so fruitful and so much fun. I appreciated his most detailed instructions during my junior stage, as well as his trust and treating me as a peer in my senior years. We have shared the most stressful and exciting moments at the x-ray beamline. His perseverance and enthusiasm have lightened me up more than he could imagine. Thanks to his creativity and perfectionism, I enjoyed experiments so much even during the most exhausting hours. I cherish the moments we talked about science and art over coffee and drinks, with my whole heart.

I have been lucky to have Prof. Daniel Silevitch around to talk with at any time, from the most urgent problems of cryogenics and electronics to brainstorming experiments in the distant future. Dan has always been helpful to answer all my questions and has witnessed my growth in graduate school day by day. I would also like to thank Alex Palmer for teaching me experimental skills with infinite patience during the first two years, and Nayoon Woo for always being ready to give me a hug when I was down. I enjoyed daily interaction with my labmates Jian Xu, Christopher Tang, and Matthew Libersky. They have brought diversified perspectives to my research and everyday life.

iv

I was fortunate to have scientific collaboration with Prof. David Hsieh and I was inspired by his vision and energy as a brilliant young scientist. I am grateful to Prof. Jason Alicea and Prof. Stevan Nadj-Perge for their service on my candidacy and defense committee, providing insightful assessment and suggestions for my thesis topic. My communication with Alon Ron and Hao Chu from Hsieh's lab have always been pleasant and informative. I appreciated their sharing of knowledge and scientific ideas.

A great part of my thesis work has been done at 4-ID-D, Advanced Photon Source. The beamtime allocation over years has secured my productivity in graduate school. My special thanks goes to Jonathan Lang, Daniel Haskel, Yongseong Choi, Gilberto Fabbris, and Joerg Strempfer for constant support of my experiments on magnetic diffraction. I am grateful for the continuously tremendous help from Antonino Miceli, Jong-Woo Kim, Douglas Robinson, Yang Ren, Vitali Prakapenka, and Sergey Tkachev. They have made experiments away from base camp so much easier. I have also used user facilities of MRSEC in The University of Chicago, where I would like to thank Qiti Guo and Justin Jureller for the strong support.

During these five years, I appreciated all the occurrence in my life, for good and for bad. They have enriched my exploration of the world and contributed to my memories in various ways. I am grateful to my friends who never stopped trusting and supporting me. In particular, I would like to thank Jiyang Chu for his love over my young years in the 20s. It used to be part of my belief in life and would stay inspiring in the long way ahead. I owe deepest thanks to Haoran Xu, Mochen Yang, and Nelson Leung for the unconditional support and accompanying me at my most depressed moments. This world is so beloved with them around.

My gratitude to my mom, Yanping Wang, is more than words can ever express. This whole life of mine is nourished from her strong mind and tender heart. At last, I dedicate this thesis to my grandparents, Weiyun Wang and Guilan Zhu. Their love will always be with me, wherever I am heading.

ABSTRACT

Antiferromagnets are choice systems to study quantum critical behavior. Unlike ferromagnets, they can experience continuous quantum phase transitions when tuned by pressure. However, the lack of a net magnetization renders experimental approaches difficult and often indirect. Here I demonstrate that both non-resonant and resonant x-ray magnetic diffraction under pressure provide the highly-desired direct probe for microscopic insights into the disappearance of the magnetic order, as well as the evolution of the charge and structural degrees of freedom. In Mo_3Sb_7, where spins are itinerant with small magnetic moments, we have discovered the doubling of the superconducting transition temperature under pressure and relate it to a lattice change from tetragonal to cubic structure. In MnP, a spiral magnetic order with tightened pitch was revealed in the high-pressure phase near a superconducting state at ~7 GPa. As the spiral pitch changes, fluctuations move from antiferromagnetic to ferromagnetic at long and short wavelengths, respectively, thereby potentially promoting spin-fluctuation-mediated superconductivity of different symmetries. In the all-in-all-out (AIAO) pyrochlore antiferromagnet $Cd_2Os_2O_7$, we discovered an antiferromagnetic quantum critical point at 35.8 GPa using new techniques for resonant x-ray magnetic diffraction under pressure. The continuous suppression of AIAO antiferromagnetic order to zero temperature is accompanied by inversion symmetry breaking of the lattice, dividing the $P - T$ phase space into three regions of different time reversal and spatial inversion symmetries. While phase lines of opposite curvature indicate a striking departure from a mean-field form at high pressure, the intertwined spin, charge, and phonon fluctuation modes point to a strong-coupled scenario of quantum criticality.

PUBLISHED CONTENT AND CONTRIBUTIONS

[1] Yejun Feng, Yishu Wang, A. Palmer, Ling Li, D. M. Silevitch, S. Calder, and T. F. Rosenbaum. "Multiple Superconducting States Induced by Pressure in Mo_3Sb_7". *Physical Review B* 95.125102 (2017). DOI: `10.1103/PhysRevB.95.125102`.
Y. Wang conducted experiments and participated in preparing the manuscript.

[2] Yishu Wang, Yejun Feng, J.-G. Cheng, W. Wu, J. L. Luo, and T. F. Rosenbaum. "Spiral Magnetic Order and Pressure-Induced Superconductivity in Transition Metal Compouns". *Nature Communications* 7.13037 (2016). DOI: `10.1038/ncomms13037`.
Y. Wang conducted experiments, analyzed data and prepared the manuscript.

[3] Yejun Feng, A. Palmer, Yishu Wang, D. M. Silevitch, and T. F. Rosenbaum. "Direct probe of Fermi surface evolution across a pressure-tuned quantum phase transition". *Physical Review B* 91.155142 (2015). DOI: `10.1103/PhysRevB.91.155142`.
Y. Wang conducted experiments and participated in preparation of the manuscript.

[4] A. Palmer, D. M. Silevitch, Yejun Feng, Yishu Wang, R. Jaramillo, A. Banerjee, Y. Ren, and T. F. Rosenbaum. "Sub-Kelvin magnetic and electrical measurements in a diamond anvil cell with in situ tunability". *Review of Scientific Instrument* 86.093901 (2015). DOI: `10.1063/1.4929861`.
Y. Wang conducted experiments and commented on the manuscript.

TABLE OF CONTENTS

LIST OF ILLUSTRATIONS

LIST OF TABLES

Chapter 1

INTRODUCTION

From the origin of the universe to boiling water in the kettle, phase transitions stand out as one of the most fundamental and fascinating topics in physics. In the past several decades, the focus has shifted to two major interests in condensed matter physic. The first is about competition between emergent phases involving topics such as magnetism, superconductivity, fractional quantum hall states, and topological order as major model systems. The second focus is on phase transitions at zero temperature, so-called quantum phase transitions (QPTs), where quantum mechanical effects become part of the puzzle in comparison to classical phase transitions at a finite temperature.

Phase transitions in a wide variety of phenomena were unified by Landau's mean-field theory [1], where the general concepts of order parameters and the character of spontaneous symmetry breaking were introduced. This theory was further developed into Landau-Ginzburg-Wilson (LGW) theory [2, 3] , incorporating an adequate consideration of fluctuation effects, and the establishment of renormalization group (RG) theory, which gives a clear physical understanding of universality and scaling laws in critical behavior. A natural extension of the LGW paradigm [4] maps QPTs to classical phase transitions with a modified (higher) dimensionality introduced by an additional imaginary time dimension in quantum mechanical systems. Although quantum criticality is theoretically predicted, both quantum fluctuations and quantum universality classes remain experimentally unresolved, mainly due to the difficulty of establishing model systems and effective tuning in a clean and continuous fashion.

While metallic ferromagnets have been proved to categorically host first-order QPTs [5, 6], several cases of antiferromagnets, such as heavy fermions [7] and density wave systems [8], have been experimentally established to exhibit continuous quantum phase transitions under athermal tuning. Varying a control parameter, such as chemical doping, pressure, and electrical and magnetic fields, at zero temperature can tune the competing interactions, and effectively drive the system towards a QPT. Enhanced spin fluctuation effects [9, 10] in the critical regime are manifested not only by novel phenomena such as non-Fermi liquid behavior [11], but also by

generating new ground states as a consequence of entropy accumulation [12]. Hence probing non-classical signatures and ground states while establishing the underlying mechanism of intertwined interactions has emerged as the central theme of studies of continuous QPTs.

This thesis focuses on the experimental study of pressure-induced antiferromagnetic QPTs in transition-metal compounds from $3d$ to $5d$ electrons, providing insights into competing interactions from spin, charge, orbit and structural degrees of freedom at both weakly- and strongly-coupled quantum critical points. By directly measuring the antiferromagnetic order parameter and the underlying lattice, we have investigated a wide spectra of competing ground states, including metal and insulator, magnetism and superconductivity, as well as characterizing the global and local symmetry changes.

1.1 Phase transitions and Landau-Ginzburg-Wilson (LGW) theory

Landau's theory of phase transitions starts from the free energy as an analytic function of a mean-field variable m:

$$F_L(m) = rm^2 + vm^3 + um^4 + O(m^5), \qquad (1.1)$$

where r, v, u are parameters depending on all the degrees of freedom in the system other than m. The physical value of m minimizes F_L, as required by thermodynamics. For sufficiently large r, F is always minimized by $m = 0$; while for sufficiently small r, the minimum of F is located at $m \neq 0$ (Fig. 1.1). Depending on v and u, the transition from a zero to nonzero value of m at a critical value $r = r_c$ could be either discontinuous ($v \neq 0$) or continuous ($v = 0, u > 0$), where the latter is of more interest with its analytic properties. The mean-field variable m is referred to as the order parameter. Its acquisition of a nonzero value characterizes a spontaneous symmetry breaking of the system's Hamiltonian by the ground state, which is the central principle of Landau's phase transition theory. For the topic of antiferromagnetic orders in this thesis, the order parameter is the staggered moments with the form of $m = \sum_i e^{iQ \cdot r_i} s_i$, where Q is the antiferromagnetic wavevector and s_i is spin on the ith site. Spins discussed in the thesis varies from itinerant to local limits and are of Ising- or Heisenberg- types. In addition, r can be regarded as any control parameter, whether thermal or nonthermal, making the Landau paradigm versatile enough to be generalized to phase transitions at zero temperature.

The most prominent prediction from Landau's theory is critical behavior governed by a scaling law, which is universal for all systems in the mean-field limit. For
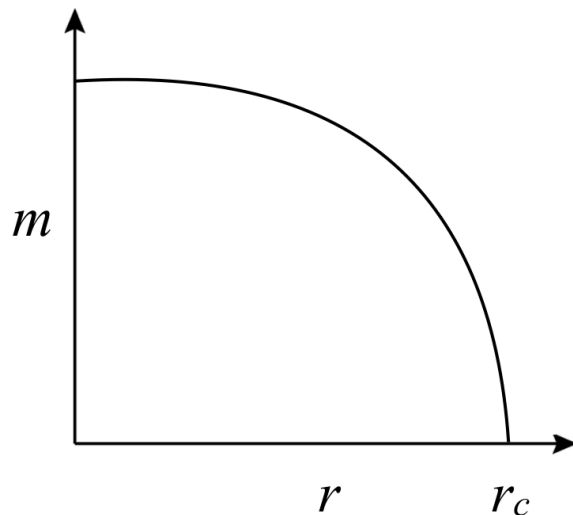
Figure 1.1: Generic diagram of phase transitions. By varying the control parameter r, such as temperature, pressure, chemical doping, field, etc., the order parameter m is tuned from zero to nonzero at critical point $r = r_c$.

example, it predicts that the critical exponent β, defined as $m \propto |r|^\beta$, has a value of $\beta = 0.5$. However, the universality observed experimentally is much weaker. Different categories of materials manifest different values of the critical exponent and they can fall beyond the predicted value of 0.5. Dimensionality also seems to be a factor, which is in contrast to the prediction of Landau theory. For instance, bulk Ising ferromagnets share a common $\beta \approx 0.32$, but in the two-dimensional Ising case, $\beta = 1/8$ [13, 14].

The reason that Landau theory fails to predict the critical behavior in real materials turns out to be the inadequate consideration of fluctuation effects. This also explains the fact that deviations are larger in low-dimensional systems since fluctuations more strongly deviates from a Gaussian distribution for lower dimensionality. In general, there is an upper critical dimensionality, where for $d > d_c^+$, Landau theory gives the correct answer as the interactions are essentially mean field, but for $d < d_c^+$, fluctuations have to be taken into account. This problem was solved by Wilson [2] who generalized Eq.(1.1) by writing the partition function $Z = e^{-F/T}$ as a functional integral:

$$Z = e^{-F/T} = \int D[\phi]e^{-S(\phi)}, \tag{1.2}$$

where

$$S(\phi) = \frac{1}{TV} \int dx[F_L(\phi(x)) + c(\nabla\phi(x))^2]. \tag{1.3}$$

Here, $\phi(x)$ is a fluctuation field whose mean value weighted by e^{-S} is m in Eq.(1.1). V is the volume and T refers to temperature. With the additional $(\nabla\phi(x))^2$ term, this Landau-Ginzburg-Wilson functional integral takes account of fluctuation effects.

The renormalization group (RG) analysis of Eq.(1.3) takes advantage of the features of critical points, where all fluctuations on smaller length scales are averaged, making it possible for the first time to prove scaling laws near criticality. Basically, the critical behavior is characterized by two thermodynamic exponents ν and η, and one dynamic exponent, z, which are defined as:

$$\xi \propto |r|^{-\nu}, \chi_m(r=0) \propto |k|^{-2+\eta}, \tau_\xi \propto |\xi|^z, \tag{1.4}$$

where $r \propto |T - T_c|$ is the reduced temperature, ξ is the correlation length, χ_m is the static order-parameter susceptibility, and τ is the correlation time.

The thermodynamic quantities follow the RG transformation:

$$f(r, h) = b^{-d} f(rb^{1/\nu}, hb^{y_h}), \tag{1.5}$$

where d is the dimensionality, $f = -(T/V)\ln Z$ is the free-energy density, h is the field conjugate to the order parameter, and y_h is related to η by $y_h = (d + 2 - \eta)/2$. Here, $b > 1$ is the RG scaling factor. A similar RG iteration for the time correlation function is given by:

$$C(k, \Omega; r, h) = b^{x_C} C(kb, \Omega b^z; rb^{1/\nu}, hb^{y_h}), \tag{1.6}$$

where Ω is frequency and x_C characterizes the correlation function C.

The critical exponents defined in Eq.(1.4), i.e., (ν, η, z), uniquely characterize the critical behavior of a physical system and define a universality class.

1.2 Quantum phase transitions (QPTs)

There is a clear distinction between thermodynamic and dynamic critical behavior. As the correlation length ξ always diverges at critical point, the renormalization transformation Eq.(1.5) can always be extended to infinity. However, for a quantum mechanical state in equilibrium, the correlation time τ is upper bounded by inverse temperature $1/kT$, which only goes to infinity for $T = 0$. Such a difference marks the fundamental difference between phase transitions at finite temperature and those at zero temperature, so-called quantum phase transitions.

This distinction is most clearly manifested by statistical mechanics. A classical canonical partition function with no velocity-dependent potential for a system of N

particles is given by:

$$
\begin{aligned}
Z &= \frac{1}{N!} \int dp dq \exp(-\beta H(p,q)) \\
&= \frac{1}{N!} \int dp \exp(-\beta H_k(p)) \int dq \exp(-\beta H_p(q)).
\end{aligned}
\tag{1.7}
$$

Here $\beta = 1/kT$ is the inverse temperature. H is the Hamiltonian that could be factorized to a phase-space integral with H_k and H_p as the kinetic and potential energies respectively. Thus one can integrate over momenta and leave the spatial integral alone to solve for thermodynamic critical behavior, and vice versa. Therefore, the thermodynamic and dynamic parts are independent.

For quantum statistical mechanics, however, $\hat{H}_k$ and $\hat{H}_p$ are operators that do not commute. Therefore, the grand canonical partition function,

$$
Z = Tr \exp(-\beta(\hat{H}_k + \hat{H}_p - \mu\hat{N})),
\tag{1.8}
$$

doesn't factorize, yielding a mutual dependence of dynamics and thermodynamics. The fundamental difference between Eq. (1.7) and (1.8) is the uncertainty relationship between momentum and space, distinguishing quantum and classical statistics. This is also manifested by the equivalent uncertainty relationship between energy and time, which is why the fluctuating time scale is cut off by $\beta = 1/kT$. This coupling modifies scaling relation Eq. (1.4) to [15]:

$$
f(r, h, T) = b^{-(d+z)} f(rb^{1/\nu}, hb^{y_h}, Tb^z).
\tag{1.9}
$$

There are three features directly reflected by the revised relation Eq.(1.9). First, temperature becomes a relevant operator for a $T = 0$ critical point. Second, temperature and frequency are expected to scale in the same way, taking into account Eq.(1.6). Last, and most remarkably, the dynamic critical exponent z modifies the dimensionality d to $d_{\text{eff}} = d + z$, as a consequence of imaginary time τ effectively acting as an extra dimension. Notably, when $\tau_\xi > 1/kT_c$, this only leads to a finite-size scaling effect. Only for transitions at $T_c = 0$ will it add an extra dimension.

Consequently, QPTs at zero temperature are fundamentally different with respect to their classical counterparts in dimensionality and in the coupling of dynamic criticality with the thermodynamics, thus forming different universality classes. There is essentially a crossover region between quantum criticality and classical criticality, with the boundary defined by $|r|^{\nu z}$ (Fig. 1.2).

Fluctuations in the quantum critical region are manifested in various ways. On one hand, they can help build up new ground states. One example, which has been
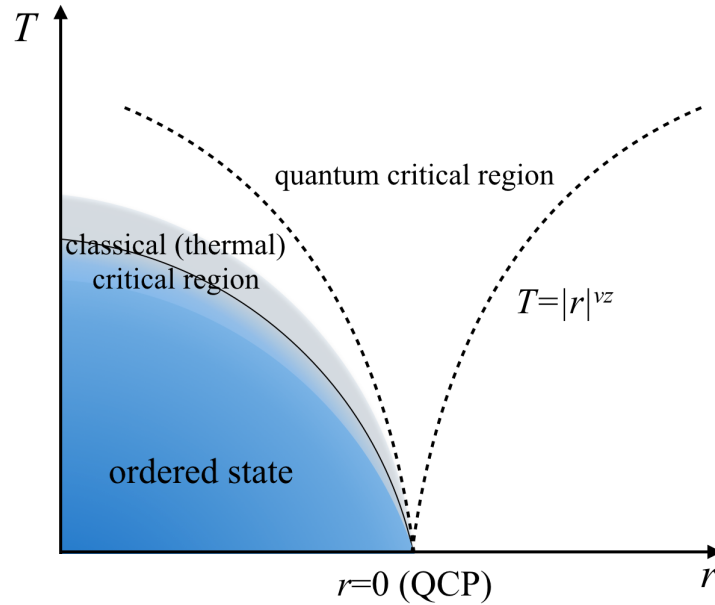
Figure 1.2: A generic phase diagram of quantum criticality. The $T - r$ phase line separates the ordered and disordered states, with the thermal critical region bounding it. The quantum critical region is set by $T \geq |r|^{\nu z}$, where the critical behavior is dominated cooperatively by dynamic and thermodynamic properties. For region $T \leq |r|^{\nu z}$, only thermodynamic critical behavior matters. The region outside both the asymptotic classical and quantum scaling regimes is characterized by crossover scaling governed by both classical and quantum fixed points.

under intensive investigation for decades, is high-T_{c} superconductivity in cuprates, potentially mediated by spin fluctuations as a residue from the ordered antiferro-magnetic state. On the other hand, novel phenomena such as non-Fermi liquid states and asymptotic behavior deviating from mean-field predictions could be induced by fluctuations. As mentioned earlier, fluctuation effects on critical behavior will be weaker with increased dimensionality, which finally ends up in a mean-field regime when $d > d_c^+$. Since quantum phase transitions can be mapped to classical phase transitions with higher effective dimensionality, it will tend to approach mean-field predictions, especially for 3-dimensional materials. This, however, is based on one assumption dating back to Landau theory, i.e. order parameter fluctuation is the only mode that extends over infinitely large length and time scales. In fact, such fluctuations, so-called soft modes, could have other origins. In addition, they could be coupled under certain circumstances [16, 17], providing one potential venue to-wards quantum criticality beyond the mean-field regime in 3-dimensional systems. Experiments related to this perspective will be discussed in Chapter 5.

1.3 Antiferromagnetic QPTs and competing ground states

QPTs in magnetic materials

As a common ground state, magnetism manifests connections to many other correlated states, thus providing one of the best platforms for characterizing phase transitions. Especially in ferromagnetic materials, where the spontaneous magnetization has a macroscopic effect with a net moment, the direct measurement of the order parameter is very accessible.
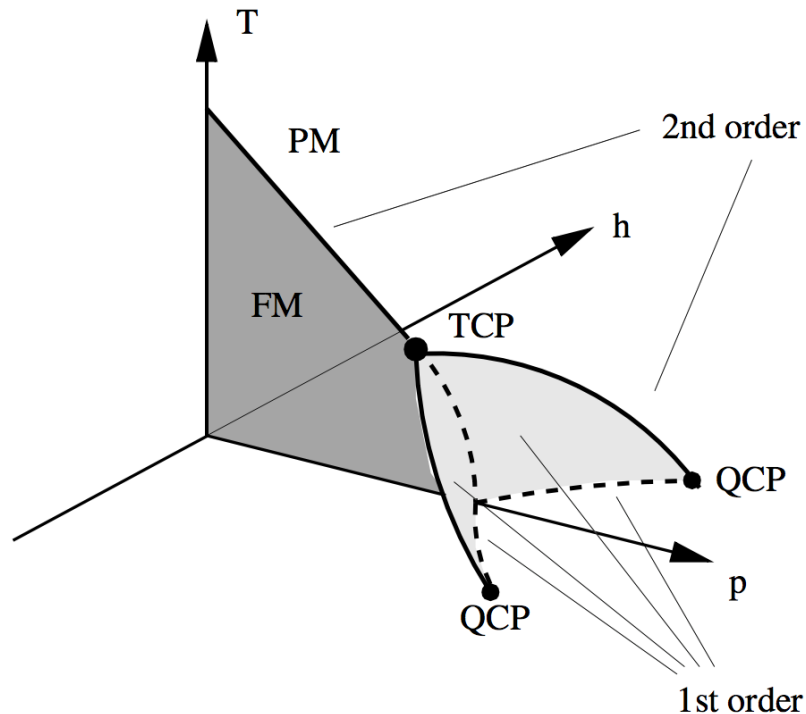
Figure 1.3: Schematic phase diagram of ferromagnetic metals in $T - P - H$ phase space. Shown are the ferromagnetic (FM, dark shaded) and paramagnetic (PM) phases at $H = 0$, the tricritical point (TCP), and the two quantum critical points (QCPs). Also shown are various lines of first-order (dashed lines) and second-order (solid lines) phase transitions, and the "wing" surfaces of first-order transitions (light shading). From Ref. [5].

The ferromagnetic transition temperature (Curie temperature) T_C can be effectively suppressed to zero by applying pressure and magnetic field (Fig. 1.3). Disappointingly, it has been observed in a multitude of ferromagnetic metals that although transitions at finite temperature are second order, transitions in the $T = 0$ plane are all first-order except for two isolated quantum critical points (Fig. 1.3) [5, 6]. This diagram has later been proved for all metallic ferromagnets and can be un-

derstood as fluctuation-induced first-order behavior due to a coupling between the magnetization and the electronic soft modes [5].

Hence quantum phase transitions in antiferromagnetic materials become of more interest. In spite of the apparent inconvenience of directly measuring the staggered moment, antiferromagnetism turns out to be a playground with significant tunability and diversity. Unlike ferromagnetism, where spins are aligned in the same direction, antiferromagnetism, either in ordered or disordered phases, manifests spin configurations in various kinds of geometries, facilitating versatile fluctuation modes that could be linked to new correlated states. For example, the resonant valence bond (RVB) state [18], or quantum spin liquid, was initially proposed as a ground state for antiferromagnetically coupled $S = 1/2$ spins on a frustrated lattice in low dimension, and was later connected to the pre-paired singlet for high-T_c superconductivity in cuprates [19]. Both the fractional excitation in quantum spin liquids and its connection to novel superconductivity are long standing topics of fundamental interest with continuous input from new quantum materials [20].

One case of antiferromagnetic QPTs that has been intensively studied and well established occurs in heavy fermion materials, where the antiferromagnetic ground state can be tuned by pressure and small magnetic field (Fig. 1.4) [11, 21]. In intermetallic $CePd_2Si_2$, the antiferromagnetic order temperature T_N is reduced by applying pressure and the system finally becomes a paramagnetic metal. The critical point, however, is not directly observed. It is instead buried in a pressure-tuned superconducting dome (Fig. 1.4) [21]. Manifesting the similarity to the phase diagram of cuprates are organic superconductors and the recently discovered iron pnictides. Together, these examples exemplify a general proposal that antiferromagnetic quantum criticality provides a mechanism for unconventional superconductivity beyond the Bardeen-Cooper-Schrieffer (BCS) theory. Quantum criticality is more clearly revealed in another heavy fermion material, $YbRh_2Si_2$ [11]. At finite temperature above the QCP at zero temperature, where the antiferromagnetic state is suppressed by a small magnetic field ($< 1T$), the electrical resistivity shows a linear dependence on temperature, which is an anomalous metallic state beyond Fermi-liquid theory. This non-Fermi liquid behavior is another relevant feature potentially emerging from quantum criticality. Similar quantum criticality has been observed in many other heavy fermion materials, such as $CeCu_2Si_2$, $CeRhIn_5$, and β-$YbAlB_4$ [7].

In addition to the series of fascinating phenomena around QCPs, quantum criticality in heavy fermions deviates from the Landau paradigm due to an effect called Kondo-
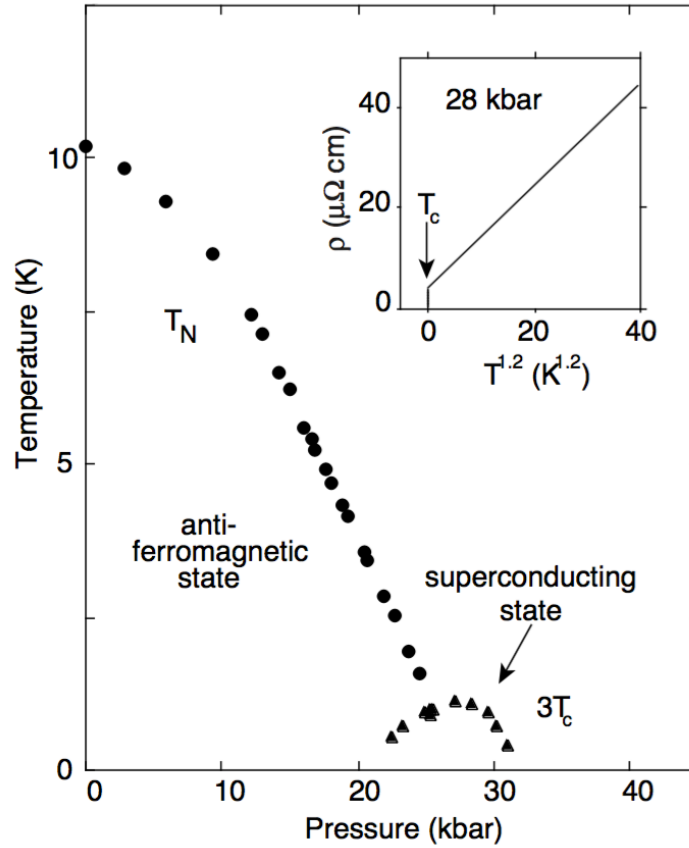
Figure 1.4: $P - T$ phase diagram of CePd$_2$Si$_2$ [21]. T_N, the antiferromagnetic transition temperature, is suppressed by pressure. At the boundary of the magnetic ordered state, superconductivity arises with transition temperature T_c, which is scaled by three times for clarity. inset: $\rho - T$ curve at 2.8 GPa, with $\rho \sim T^{1.2}$ above T_c over nearly two decades, and a sharp drop at 500 mK indicating the superconducting transition. From Ref. [21].

exchange coupling, which introduces quantum coherence between local moments of $4f$ electrons to conduction electrons. While approaching the QCP from the paramagnetic side, Kondo screening will lead to an effective ground state where local moments and conduction electrons are entangled, which has its own QCP [7, 22]. Whether the two QCPs marking breakdown of antiferromagnetic order and Kondo effect are locked or separated is still an open question, but it provides one venue to break out from Landau phase transition theory by introducing local criticality. With the combination of superconductivity, non-Fermi liquid behavior, and novel quantum criticality, heavy fermion compounds demonstrate the richness of phenomena related to antiferromagnetic QCPs.
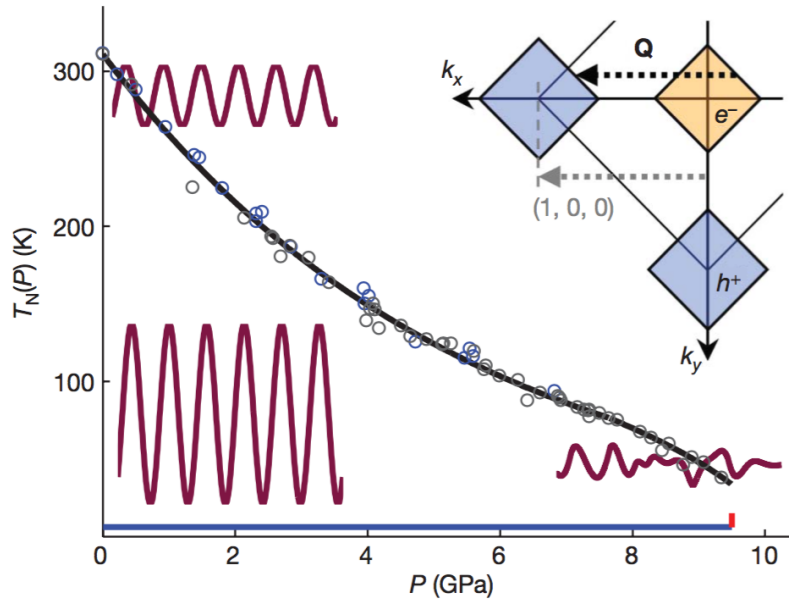
Figure 1.5: Phase diagram and Brillouin zone schematic for magnetism in chromium [23]. Spin density wave transition temperature T_N is suppressed by application of pressure. Inset: schematic of the first Brillouin zone, showing the incommensurate wave vector Q. From Ref. [23].

Another well established case of a continuous QPT is the spin density wave (SDW) in Cr [23, 24], which breaks down under pressure $P_c \sim 10$ GPa (Fig. 1.5), discovered by high-resolution x-ray magnetic diffraction. Unlike heavy fermions, where the magnetism is manifested by local moments, instabilities in Cr at the QCP of the SDW is of an itinerant nature located at an incommensurate Q. A non-monotonic evolution of Q with pressure along with the limiting sinusoidal form of the density wave reveals the dominant role of this itinerant instability in the vicinity of the critical points, with little influence from the lattice [24]. The magnetotransport measurement in Cr around the critical pressure demonstrates a non-mean-field feature [25], which reveals reconstruction of the magnetic Fermi surface and is distinct from the critical scaling measured in chemically disordered Cr:V under pressure [25]. So far, no new ground state has been discovered in the magnetically disordered phase, in contrast to heavy fermions. Nevertheless, as a clean elemental metal, Cr sets the benchmark for itinerant metals with signatures of strong coupling [26], which can be compared with other experimental cases.

Spin-fluctuation mediated superconductivity

As has been demonstrated earlier, antiferromagnetic quantum criticality could facilitate superconductivity alternative to the phonon-mediated BCS mechanism [27]. First proposed for heavy fermion superconductors [28, 29] and high-T_c cuprates, this scenario has been revived in iron pnictides and other transition-metal magnets. In a traditional BCS picture, electrons with opposite momentum and spin, i.e. $(+k, \uparrow)$ and $(-k, \downarrow)$, are paired through a lattice vibrational mode (phonon), opening an isotropic gap (s wave) around the Fermi surface. The electron-phonon coupling is on site ($r = 0$), while the net attraction potential is achieved by a retardation effect (t_0) to avoid the primary Coulomb interaction between two electrons [27], forming an attractive region in space and time.

In addition to charge, electrons also have a spin degree of freedom, which also could generate an attractive potential without assistance from phonons [10, 30]. Although the microscopic mechanism is still under investigation, a phenomenological description by analogy to the BCS formula is helpful for proposing new materials and predicting experimental observations. Following Refs. [10] and [30], the induced interaction between two quasiparticles with charge e, e' and spin s, s', respectively, in the linear response approximation, can be written as:

$$V_{ind} = -ee'g_n^2\chi_n(r,t) - s \cdot s'g_m^2\chi_m(r,t), \tag{1.10}$$

where g_n and g_m are empirical parameters that measure the strength of the coupling to charge and to spin, while χ_n and χ_m are the non-local charge density and magnetic susceptibility, respectively. The quasiparticle pairing induced by this interaction will generate Cooper pairing with certain oscillatory features, with an attraction area located differently in space and time. Following Fig. 2 in Ref. [30], repulsive interaction at $r = 0, t = 0$ for static charges becomes attractive at $r = 0, t > 0$ due to the phonon effects. This is the mechanism in BCS theory. Spin-spin interaction at the border of long-range ferromagnetic orders will involve two parallel spins, i.e. in a spin triplet state, for which attraction region centers at $r = 0$. As for antiferromagnetic cases where antiparallel spins form a singlet state, the attracted quasiparticles are separated by a finite r.

Due to the requirement of the Pauli principle, the overall wavefunction of Cooper paris should be antisymmetric. Thus the spin triplet pairing will occupy the lowest allowed p-wave state with odd angular momentum. As for the antiferromagnetically-coupled spin singlet state, it has to take a d-wave with even angular momentum

instead of an *s*-wave symmetry since the interaction is repulsive at the origin. The symmetry of Cooper pairing, effectively that of the superconducting gap, is the most definitive nature of unconventional superconductivity. For example, *d*-wave superconductivity has been measured in cuprates [31, 32], while superconductivity in Sr_2RuO_4 has been predicted to be chiral *p*-wave [33].

In real materials, superconductivity at the border of a ferromagnetic state is rare unless the electron moments that form the ferromagnetism are different from the electrons that pair to give superconductivity [34]. In most cases, the two are hard to reconcile because an attraction region around $r = 0$ necessitates a large magnetic energy scale to overcome repulsion effects. In addition, the inner product of triplet-paired spins is a factor of three smaller than singlet-pairing, which is an intrinsic weakness quantum mechanically. Therefore, antiferromagnetic QCPs seem to be more likely to host superconducting states. The richness of the spin configurations also provides tunability to reveal the microscopic pairing mechanism. We will discuss this idea further in Chapter 4.

Magnetically-driven metal-insulator transitions

Correlated insulators are materials that should be metallic from conventional band theory, but are insulators due to the localization by electron-electron correlations, which also can be expressed in magnetic ordering. Therefore, a magnetic transition involved with a metal-insulator transition is always of interest. The most prominent model for correlated insulators is the Mott-Hubbard model, most of which are antiferromagnetic. The gap opening in Mott insulators is driven by the on-site Coulomb repulsion, U, which is independent of the magnetic order [35]. In addition, quantum phase transitions of Mott insulators are typically first order.

In contrast, Slater insulators are proposed as a pure magnetic transition, where the insulating gap is opened naturally by the formation of a long-range magnetic order [36]. This transition is predicted to be continuous [36]. More interestingly, the critical point will involve fluctuations from charge and spin degrees of freedom coupled naturally, which might exhibit novel features of criticality. As originally proposed by Slater [36], electrons with opposite spins should move in different Hartree-Fock potentials. Particularly for antiferromagnetic cases, the potential energy difference will result in a periodic perturbation of the potential, which has twice the lattice periodicity, leading to an energy band splitting with a gap in the middle. This model only works for traditional antiferromagnetic order with a superlattice twice the size

of the lattice. Recently, this theory has been generalized to apply to antiferromagnetic ordering without Brillouin zone folding [37]. We will address this possibility in detail in Chapter 5.

1.4   Structure of this thesis

The remaining five chapters of the thesis are organized as follows:

In Chapter 2, I will introduce the experimental setup and principle of x-ray diffraction and optical Raman spectroscopy techniques within a high pressure sample environment. These techniques have been developed to address the microscopic features and symmetry evolution across a quantum critical point.

In Chapter 3, I will present the pressure-tuned superconducting states in Mo_3Sb_7, where we have addressed the effects of magnetism and crystal structure on the superconductivity.

In Chapter 4, I will discuss our discovery of the spiral magnetic order in MnP along with its inspiration of antiferromagnetically-induced superconductivity, addressing both the physics and possibilities for experiments on related materials.

In Chapter 5, I will describe our work on $Cd_2Os_2O_7$, where so-called all-in-all-out antiferromagnetic order on a pyrochlore lattice has been suppressed by pressure with additional inversion symmetry breaking of the lattice. Features of quantum critical behavior beyond mean-field theory and the implications for the metal-insulator transition also will be discussed.

In Chapter 6, I will summarize my results and conclusions and describe future prospects.

Chapter 2

EXPERIMENTAL METHODS

Quantum phase transitions can be experimentally realized by non-thermal control parameters such as chemical doping, magnetic field, pressure, etc., among which pressure is a particularly clean tuning method without introducing disorder or additional symmetry breaking. I have summarized in Table 2.1 the properties that need to be experimentally revealed about a quantum phase transition and the measurement methods we have incorporated with high pressure sample environments. Such experiments are technically challenging in two aspects: i) to create a sample environment with uniform and stable pressure condition, and ii) to distinguish small signals from miniature samples while the background level is high and the measurement geometry is limited due to the high pressure apparatus.

Table 2.1: Experimental study of pressure-tuned quantum phase transitions

properties of a quantum phase transition	probe techniques	related experimental systems and chapters in this thesis
order parameter (microscopic magnetic order for AFM)	(non-resonant; resonant[1]) x-ray magnetic diffraction	MnP (Ch4); $Cd_2Os_2O_7$ (Ch5)
critical point	x-ray diffraction; optical Raman spectroscopy[2]; electrical transport; ac magnetic susceptibility	Mo_3Sb_7 (Ch3); MnP (Ch4); $Cd_2Os_2O_7$ (Ch5)
first-order signature or continuous nature	x-ray diffraction; optical Raman spectroscopy	Mo_3Sb_7 (Ch3); MnP (Ch4); $Cd_2Os_2O_7$ (Ch5)
new ground state	ac magnetic susceptibility; x-ray magnetic diffraction	Mo_3Sb_7 (Ch3); $Cd_2Os_2O_7$ (Ch5)
quantum critical behavior	electrical transport[3]	not included

In this thesis, we have used multiple probes, including x-ray magnetic diffraction, optical Raman spectroscopy, and ac magnetic susceptibility, in order to address the issue of complexity in both weak and strong coupling regimes through a quantum phase transition.

2.1 High pressure sample environment
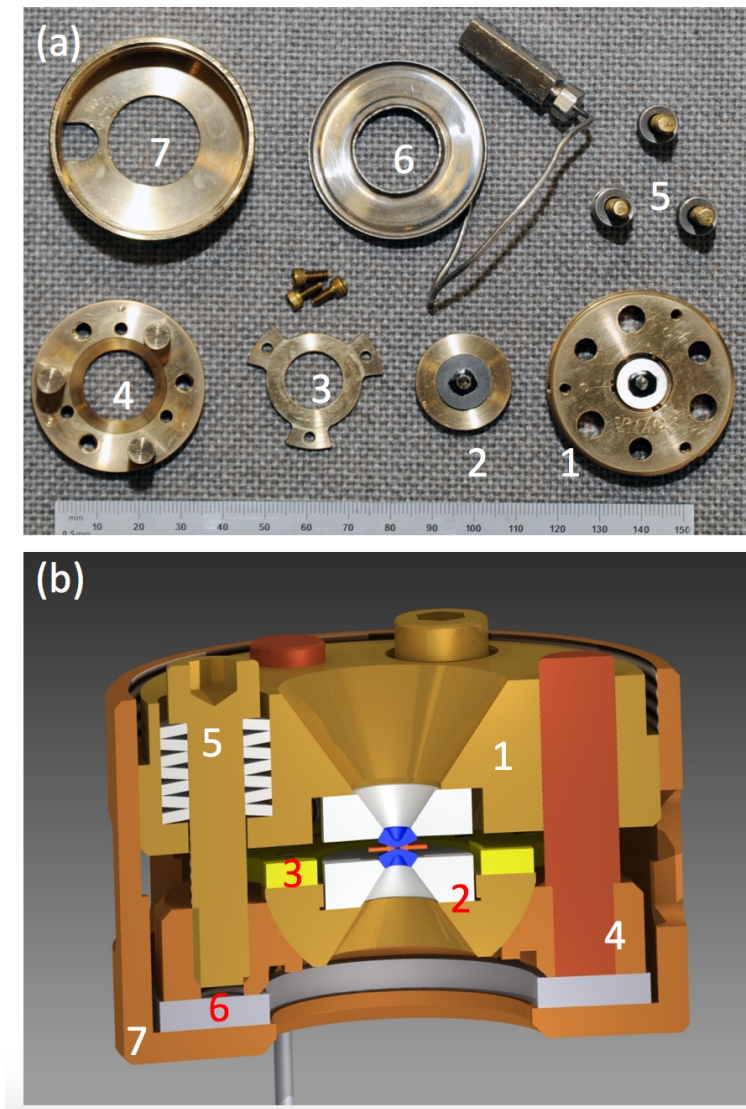
Figure 2.1: 3-pin diamond anvil cell. (a) Photograph of actual cell components. Numbers are correspnding to those in panel b. (b) Cross-sectional view of a modified three-pin Merrill-Bassett type [38] diamond anvil pressure cell. 1, 2: Upper and lower pieces of cell body. Pins press-fit into the lower part align the two pieces with each other. 3,4: Rear-perforated diamonds mounted on tungsten carbide seats; one seat is mounted on a rocker for angular alignment. The partially-perforated diamond anvils are specially designed to remove background signal from the diamonds in scattering experiments. A retaining ring 5 holds the rocker and seat in position. Screws and stacks of Belleville disc washers 6 provide the sealing force and initial room-temperature pressurization. A helium bellows actuator 7 and retaining cap 8 allow for *in situ* cryogenic pressurization.

Due to their relatively low mass, diamond anvil cells (DACs) are the most convenient

pressure vessels to be incorporated into a cryogenic sample environment. We use cells made from silicon aluminum bronze (C64200), which does not need heat treatment and thus is straightforward to be machined to high precision. It also has excellent anti-galling and anti-seizing properties under non-lubricated and vacuum conditions. The original Merrill-Bassett design [38] was modified to allow pins with a larger diameter (1/4 inch) for better stability (Fig. 2.1). To improve efficiency, pressure was varied in situ using a helium diaphragm or membrane [39–41] (Fig. 2.1, part 6), removing the need to thermally cycle to room temperature for each pressure point. Ruby fluorescence and Ag lattice constant are used to measure pressure, while the latter is only functional for diffraction experiments.

Apart from the traditional 3-pin cell design, we have also designed a more compact cell with a 1 in. diameter (Fig. 2.2) [42]. Compared with the 3-pin design, the choice of cell body materials and the capability of changing pressure in situ using a helium membrane are the same. Instead of using pins to align the two opposing parts of the cell body, this cell use sliding cylindrical surfaces for alignment (Fig. 2.2, part 2 and 3). The 1 in. diameter of this cell makes it compatible with many commercial helium-4 cryostats in a large field-temperature ($H - T$) phase space and top-mounting systems such as helium-3 and dilution refrigerators, while allowing ample clearance for the necessary vacuum and radiation shields needed for sub-Kelvin operation. For the measurements described in this thesis (mainly in Chapter 3), the pressure cell was loaded inside a commercial helium-4 cryostat (PPMS, Quantum Design) with a base temperature of 1.7 K and a 9 T magnet.

Compared to the typical pressure conditions used in geophysical research for which the diamond anvil cell was originally developed, condensed matter physics research at high pressure presents a new set of technical constraints. Most condensed matter phenomena arise from subtle interplay of small energy scales, thus it is most critical to have a stable and uniform pressure condition and to preserve the initial crystal quality through the entire cooling and pressurization process, from ambient pressure and temperature to the targeted $P - T$ point.

As we noted previously [40], the choice of pressure medium can help maintain a large chamber-to-sample volume ratio as the pressure increases. A typical pressure chamber has an initial volume of order 0.02 mm^3 and a chamber-to-sample ratio of about 100:1. Some highly compressible noble gases, such as helium and neon, significantly reduce their own volumes to 5-10% at high pressure and low temperature, and thus require a very small and thin sample (such as $10 \times 10 \times 5$
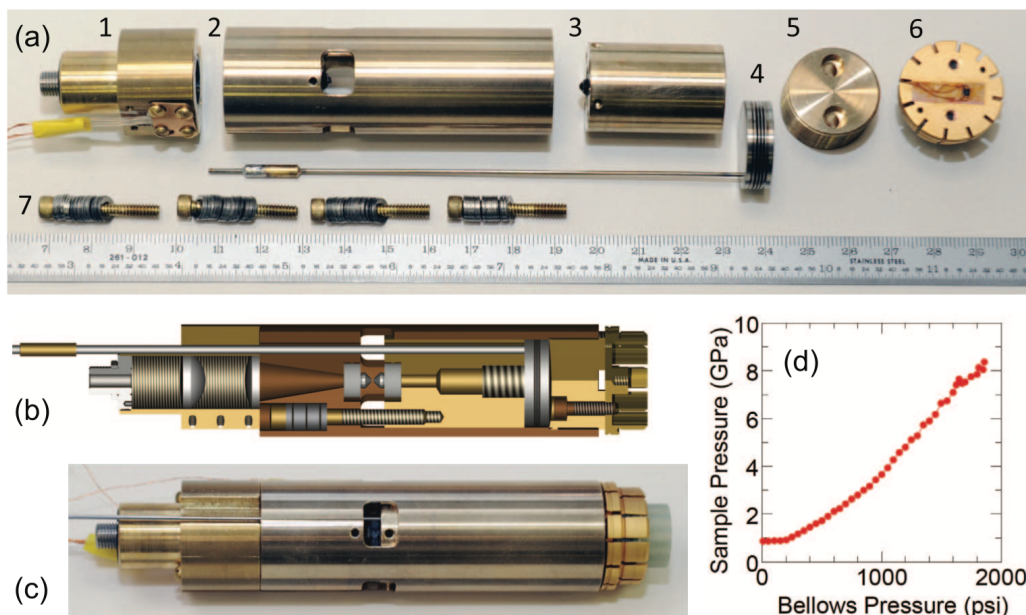
Figure 2.2: Design of the compact bellows-controlled diamond anvil cell compatible with PPMS [42]. (a) Disassembled cell showing individual components: (1) optics mount containing SMA fiber coupler and two plano-convex lenses to couple sample chamber to fiber; a Cernox thermometer is attached to the outside to measure the cell temperature. (2) Outer cylinder of the cell body. A mounted diamond is visible through the window. (3) Inner cylinder of the cell body with a second mounted diamond. (4) Helium bellows actuator. (5) Plug with external thread to screw into part 1 of the cell body for bellows confinement. (6) PPMS sample puck for mounting to cryostat base. A GaAs Hall sensor mounted to the puck measures the applied field. (7) Four brass 6-32 screws with stacks of 302 stainless steel Belleville spring washers (Associated Spring Raymond) for sealing and initial pressurization of cell. (b) Cross-sectional rendering of the internal structure of the cell. (c) Photograph of a fully assembled cell. (d) Loading curve of the bellows-actuator at $T = 8$ K. Pressure is measured using the ruby fluorescence through the fiber optics. Stick-slip motion of the cell is observed at high membrane pressures. From Ref. [42]

μm^3 in Ref. [43]), which significantly cuts down the signal. We regard a 4:1 methanol:ethanol mixture as an ideal pressure medium up to at least 40 GPa, combining both quasi-hydrostaticity and low compressibility to preserve single crystal samples in a voluminous pressure chamber. A careful choice of chamber diameter and thickness will allow reaching pressures comparable to the estimated limits given in Ref. [44] while minimizing any pressure anisotropy [40] for a fixed anvil size. However, the equation of state of the pressure medium only dominates when the gasket material is strong enough. Thus, different materials are preferred depending on the targeted pressure. For example, stainless steel gaskets typically maintain

pressure below 15 GPa, while for the experiments in the pressure range of 15 - 40 GPa, Rhenium is used instead.

Pressurization is a mechanical process that is always dynamic and non-adiabatic. The pressure-driven evolution of a sample chamber's lateral diameter and vertical thickness has been well discussed in the literature [44, 45]. In addition, diamond anvils tend to elastically buckle towards the center under pressure [45]. With the chamber shape changing upon pressurization, a new pressure gradient is established in both the gasket and pressure medium that eventually relaxes towards a quasi-hydrostatic condition, limited by the shear modulus of the medium and the chamber geometry. This redistribution of the pressure medium through plastic deformation and rheology inside a shape-changing chamber is a major characteristic of diamond anvil cells. It suggests that a voluminous pressure chamber is always preferable, as such a chamber effectively insulates the sample from large movements of the pressure medium. At low temperature ($\sim$ 4 K), the pressure medium relaxation process can take as long as hours.

2.2 X-ray magnetic diffraction

X-ray and neutron magnetic diffractions are the only two probes that are capable of providing direct and microscopic understanding of both the ordering wave vector and the spin structure, in comparison to macroscopic techniques such as magnetic susceptibility, heat capacity, optical Kerr effect, muon spin rotation (μSR), and electrical transport measurements, or local probes such as nuclear magnetic resonance and x-ray magnetic dichroism. These two diffraction techniques are complementary to each other. Neutrons have better sensitivity to magnetic moments, but also have intrinsic strong absorption from several elements of natural abundance such as Gd, Sm, Eu, B, Cd, Dy, and Ir, for which isotope enriched specimen are typically prepared. Second, it is not always easy to grow single crystals of large sizes for neutron diffraction, especially for samples containing scarce and expensive elements such as Ir and Os. In addition, neutrons cannot be focused down to a small beam size. Thus typical pressure cells for neutron diffraction are large, and difficult to cool down to very low temperature [46]. Neutron magnetic single-crystal diffraction is typically limited to pressures below 10 GPa [46–48], mainly due to the combined effect of a large range of accessible reciprocal space, which weakens the pressure cell, and cryogenic cooling capability, which limits a pressure cell's size.

All the issues listed above can be addressed with x-ray magnetic diffraction. As

an electromagnetic wave, x-rays are sensitive to both charge distribution and magnetization density. Compared with that for neutron scattering from magnetically ordered states, the cross section is reduced by a factor of $(\hbar\omega/mc^2)^2$ [49], which, however, could be made up by the brightness of a synchrotron radiation source. In addition, it brings special effects of high resolution in momentum space, polarization phenomenon and resonance techniques, which give an enhanced cross section. With much better focusing of the beam down to ~100 μm, a high pressure cell with smaller mass (Fig. 2.1) can also be used. X-ray magnetic diffraction of both non-resonant [49–56] and resonant [57–64] types became a research tool only after the availability of 2nd generation synchrotron radiation sources.

A nonrelativistic calculation using perturbation theory gives the cross section for elastic scattering as [49]:

$$
\left(\frac{d^2\sigma}{d\Omega'dE'}\right)_{a\to b,\lambda\to\lambda'} = \left(\frac{e}{mc^2}\right)^2 \delta(E_a - E_b + \hbar\omega_k - \hbar\omega_{k'})
$$

$$
\left|\left\langle b\left|\sum_j e^{iK\cdot r_j}\right|a\right\rangle \epsilon\cdot\epsilon' - i\frac{\hbar\omega}{mc^2}\left\langle b\left|\sum_j e^{iK\cdot r_j}\cdot s_j\right|a\right\rangle \epsilon\times\epsilon'\right.
$$

$$
+ \frac{\hbar^2}{m}\sum_c\sum_{ij}\left(\frac{\left\langle b\left|\left(\frac{\epsilon'\cdot P_i}{\hbar} - i(k'\times\epsilon')\cdot s_i\right)e^{-ik'\cdot r_i}\right|c\right\rangle\left\langle c\left|\left(\frac{\epsilon\cdot P_j}{\hbar} + i(k\times\epsilon)\cdot s_j\right)e^{-ik\cdot r_j}\right|a\right\rangle}{E_a - E_c + \hbar\omega_k - i\Gamma_c/2}\right.
$$

$$
+ \left.\left.\frac{\left\langle b\left|\left(\frac{\epsilon\cdot P_j}{\hbar} + i(k\times\epsilon)\cdot s_j\right)e^{-ik\cdot r_j}\right|c\right\rangle\left\langle c\left|\left(\frac{\epsilon'\cdot P_i}{\hbar} - i(k'\times\epsilon')\cdot s_i\right)e^{-ik'\cdot r_i}\right|a\right\rangle}{E_a - E_c - \hbar\omega_{k'}}\right)\right|^2,
$$

$$(2.1)$$

where $|a\rangle$ and $|b\rangle$ are the initial and final eigenstates, $k\lambda$ and $k'\lambda'$ represent the momentum and polarization of incident and outgoing photons, and $K = k - k'$ is the momentum transfer. ϵ, ϵ' are the unit vectors of polarization with reference to the scattering plane. The first term in Eq. (2.1) gives the usual Thomson cross section for Bragg scattering and depends on the Fourier transform of the charge density. With the other three terms being spin-dependent, and noticing that anomalous dispersion effects occur when $\hbar\omega_k \sim E_a - E_c$, the magnetic scattering cross section needs to be discussed under both non-resonant and resonant conditions.

Non-resonant x-ray magnetic scattering

Following Ref. [49], assume $\omega_k \sim \omega_{k'} \gg (E_a - E_c)/\hbar$. Neglecting the latter terms in the denominators, Eq.(2.1) is reduced to:

$$\left(\frac{d^2\sigma}{d\Omega' dE'}\right)_{a \to b, \lambda \to \lambda'} = \left(\frac{e}{mc^2}\right)^2 \delta(E_a - E_b + \hbar\omega_k - \hbar\omega_{k'})$$

$$\left| \left\langle b \left| \sum_j e^{iK \cdot r_j} \right| a \right\rangle \epsilon \cdot \epsilon' - i\frac{\hbar\omega}{mc^2} \left\langle b \left| \sum_j e^{iK \cdot r_j} \left(i\frac{K \times P_j}{\hbar k^2} \cdot A + s_j \cdot B \right) \right| a \right\rangle \right|^2,$$

$$(2.2)$$

where

$$A = \epsilon' \times \epsilon$$

$$B = \epsilon' \times \epsilon + (\hat{k}' \times \epsilon')(\hat{k} \cdot \epsilon) - (\hat{k} \times \epsilon)(\hat{k} \cdot \epsilon') - (\hat{k}' \times \epsilon) \times (\hat{k} \times \epsilon).$$

$$(2.3)$$

Compared with the first charge scattering term, the magnetic terms are smaller by $(\hbar\omega/mc^2)$ in amplitude. Therefore, the pure charge scattering is larger than the pure magnetic scattering by a significant factor:

$$\frac{\sigma_{\text{mag}}}{\sigma_{\text{charge}}} \simeq \left(\frac{\hbar\omega}{mc^2}\right)^2 \frac{N_{\text{m}}^2}{N^2} \langle s \rangle^2 \frac{f_{\text{m}}^2}{f^2},$$

$$(2.4)$$

where N_{m} is the number of magnetic electrons or atoms, N is the number of electrons or atoms, and f_{m} and f are the magnetic and charge form factors, respectively. For 10keV photons, $(\hbar\omega/mc^2)^2 \sim 4 \ 10^{-4}$. Considering that f_{m} of an atom falls off more rapidly than f, the ratio is even further reduced. The x-ray pure magnetic scattering should be observed in magnetic structures where the Bragg peaks do not occur at the same point in reciprocal space.

Eq.(2.2) also shows a different polarization factor for the orbit and spin magnetization densities. The magnetization-dependent part $\langle M_{\text{m}} \rangle$ of the x-ray cross section can be written explicitly in terms of $L(K)$ and $S(K)$:

$$\langle M_{\text{m}} \rangle = \frac{1}{2}L(K) \cdot A' + S(K) \cdot B,$$

$$(2.5)$$

where

$$A' = 1(1 - \hat{k} \cdot \hat{k}')(\epsilon' \times \epsilon) - (\hat{k} \times \epsilon)(\hat{k} \cdot \epsilon') + (\hat{k}' \times \epsilon')(\hat{k}' \cdot \epsilon).$$

$$(2.6)$$

B has the same definition as in Eq.(2.3).

From the point of view of performing synchrotron experiments, it is convenient to express the vectors A' and B as 2×2 matrices in a basis whose components are

parallel (π-polarized) and perpendicular (σ-polarized) to the diffraction plane. In this basis, Eq.(2.5) becomes [53]:

$$\langle M_{\mathrm{m}} \rangle = \begin{pmatrix} \langle M_{\mathrm{m}} \rangle_{\sigma-\sigma} & \langle M_{\mathrm{m}} \rangle_{\sigma-\pi} \\ \langle M_{\mathrm{m}} \rangle_{\pi-\sigma} & \langle M_{\mathrm{m}} \rangle_{\pi-\pi'} \end{pmatrix}$$

$$= \begin{pmatrix} S \cdot (k \times k') & -\frac{K^2}{2k^2}\left[\left(\frac{L(K)}{2} + S(K)\right) \cdot k' + \frac{L(K)}{2} \cdot k\right] \\ \frac{K^2}{2k^2}\left[\left(\frac{L(K)}{2} + S(K)\right) \cdot k + \frac{L(K)}{2} \cdot k'\right] & \left(\frac{K^2}{2k^2}L(K) + S(K)\right) \cdot (k \times k') \end{pmatrix}.$$

$$(2.7)$$

It is worth noting that the diagonal matrix element involves magnetization density oriented only in the direction perpendicular to the diffraction plane, while the off-diagonal matrix elements involve components that are within the diffraction plane. In addition, the most sensitive $\sigma - \sigma$ channel is independent of the orbital component $L(K)$. In a real scattering experiment, the magnetic scattering with angle 2θ is represented by:

$$\langle M_{\mathrm{m}} \rangle =$$

$$\begin{pmatrix} (\sin 2\theta)S_2 & -2(\sin^2 \theta)[(\cos \theta)(L_1 + S_1) - (\sin \theta)S_3] \\ 2(\sin^2 \theta)[(\cos \theta)(L_1 + S_1) + (\sin \theta)S_3] & (\sin 2\theta)[2(\sin^2 \theta)L_2 + S_2] \end{pmatrix},$$

$$(2.8)$$

where θ is the Bragg angle and $S_{1,2,3}$ are projections of the reciprocal space spin density with S_2 out of the diffraction plane and $S_{1,3}$ in plane (similar for L_i, $i = 1, 2$). For materials with a quenched orbital moment, as is the case in most $3d$ materials, Eq.(2.8) gives a cross section of:

$$\frac{d\sigma}{d\Omega} = \left(\frac{e^2}{mc^2}\right)^2 \left(\frac{\hbar\omega}{mc^2}\right)^2 \left\{[S_2 \sin(2\theta)]^2 + 4\sin^4(\theta)[S_1 \cos \theta + S_3 \sin \theta]^2\right\}. \quad (2.9)$$

For hard x-rays and when the transferred momentum is low, 2θ angles are small with $\sin 2\theta \sim 0.005$, and Eq.(2.9) can be simplified to:

$$\frac{d\sigma}{d\Omega} = \left(\frac{e^2}{mc^2}\right)^2 \left(\frac{\hbar\omega}{mc^2}\right)^2 [S_2 \sin(2\theta)]^2, \quad (2.10)$$

where only the S_2 perpendicular spin projection remains. In MnP, as we will discuss in Chapter 4, we have observed magnetic Bragg peaks at $(1 \pm Q', 0, 0)$ parallel to the magnetic order parameter $(Q', 0, 0)$. Hence the observed diffraction signals indicate a transverse component of antiferromagnetic order, ruling out a purely longitudinal spin wave.

Although a polarization study under non-resonant conditions could separate spin and charge magnetization density along different directions in 3-dimensional space, it is experimentally not practical given the small cross section and the intensity loss of 99% after reflection by an analyzer crystal. Non-resonant diffraction without a polarization study mainly picks up signals from the $\sigma - \sigma$ channel, which is only sensitive to the spin density out of the diffraction plane, as indicated in Eq.(2.10).

Resonant x-ray magnetic scattering

Starting with the general expression of Eq.(2.1), we have discussed the cross section of magnetic scattering in the limit of high energy, away from resonant conditions. We have also noticed the anomalous dispersion in Eq.(2.1) when $\hbar\omega \sim E_c - E_a$. In fact, large resonant enhancements of x-ray magnetic scattering cross sections have been observed while tuning the incident x-ray energy through the L or M absorption edges [57, 59]. This can be understood as electric quadrupole ($E2$) transitions to $4f$ levels and electric dipole ($E1$) transitions to $5d$ levels, i.e. the exclusion principle allows only transitions to unoccupied orbitals, resulting in an exchange interaction sensitive to the magnetization of the f and d bands. The multiple magnetic contributions are smaller by a factor of $(\hbar\omega/mc^2)$, $< 1/60$ for typical x-ray edges and are not considered here [58, 60].

Following the discussion of resonant γ-ray scattering, for an electric 2^L-pole resonance (EL) in a magnetic ion, the contribution to the coherent scattering amplitude is given by [58]:

$$f^e_{EL} = \frac{4\pi}{|k|} f_D \sum_{M=-L}^{L} \left[\epsilon'^* \cdot Y^{(e)}_{LM}(k') Y^{(e)*}_{LM}(k) \cdot \epsilon \right] F^{(e)}_{LM}(\omega), \qquad (2.11)$$

where f_D is the Debye-Waller factor and $Y^{(e)}_{LM}(k)$ are vector spherical harmonics. The strength of the resonance is determined by the factor F_{LM}, which, in turn, is determined by atomic properties:

$$F^{(e)}_{LM} = \sum_{a,c} \left[P_a P_a(c) \Gamma_x(aMc; EL)/\Gamma(c) \right] / \left[x(a,c) - i \right], \qquad (2.12)$$

where $|c\rangle$ is the excited state of the ion and $|a\rangle$ is the initial state. P_a is the probability of the ion existing in the initial state $|a\rangle$ and $P_a(c)$ is the probability for a transition from $|a\rangle$ to $|c\rangle$, which is determined by the overlap integral between the two states. $\Gamma x/\Gamma$ is the ratio of the partial line width of the excited state due to a pure 2^L-pole radiative decay due to all processes, both radiative and non-radiative. Finally,

$x = E_c - E_a - \hbar\omega/(\Gamma/2)$ is the deviation from the resonance condition in units of the total half-width following Eq.(2.1) [49]. Eq.(2.12) is valid for isotropic systems in which the symmetry is only broken by the magnetic moment. The application of the symmetries of a particular point group produced by the local environment will alter the allowed terms, such as the resonant charge scattering at forbidden Bragg peaks, referred to as Anisotropic Tensor Susceptibility (ATS) scattering, as we will discuss later. Nevertheless, this atomic factor determines the resonance most directly. For example, enhancement of the cross section at the K edge is usually within a factor of 10, while that at the L edge could be a factor ~ 100 (Os L_2 and L_3) – 1000 (Ir L_3).

Electric dipole transitions ($E1$) usually dominate the resonant magnetic cross section, such as the case of transitions in $2p_{\frac{1}{2},\frac{3}{2}} \rightarrow 5d$ electron systems like Ho [57], osmates [63] and iridates [64]. With $L = 1$, the operators with spherical harmonics become:

$$
\begin{aligned}
\epsilon'^* &\cdot Y_{l\pm1}^{(e)}(k') Y_{l\pm1}^{(e)*}(k) \cdot \epsilon \\
&= \frac{3}{16\pi} \left[\epsilon' \cdot \epsilon \mp i(\epsilon' \times \epsilon) \cdot z_n - (\epsilon' \cdot z_n)(\epsilon \cdot z_n) \right], L = 1, M = \pm1 \\
\epsilon'^* &\cdot Y_{l\pm1}^{(e)}(k') Y_{l\pm1}^{(e)*}(k) \cdot \epsilon \\
&= \frac{3}{8\pi} \left[(\epsilon' \cdot z_n)(\epsilon \cdot z_n) \right], L = 1, M = 0,
\end{aligned}
\tag{2.13}
$$

where z_n is a unit vector in the direction of the magnetic moment of the nth ion. Therefore, the form factor for $E1$ resonant scattering cross section from the nth ion is:

$$
f_{nE1}^{\text{XRES}} = \left[(\epsilon' \cdot \epsilon) F^{(0)} - i(\epsilon' \times \epsilon) \cdot z_n F^{(1)} + (\epsilon' \cdot z_n)(\epsilon \cdot z_n) F^{(2)} \right],
\tag{2.14}
$$

with

$$
F^{(0)} = \frac{3}{4k}[F_{11} + F_{1-1}], \quad F^{(1)} = \frac{3}{4k}[F_{11} - F_{1-1}], \quad F^{(2)} = \frac{3}{4k}[2F_{10} - F_{11} - F_{1-1}]. \tag{2.15}
$$

The first term of Eq.(2.14) simply contributes to the charge Bragg peak since no magnetic moments are included. It is noteworthy that in an incommensurate antiferromagnet, the second term produces first-harmonic magnetic satellites and the third term, containing two powers of the magnetic moment, produces the second-harmonic magnetic satellites [60]. The last two terms should have polarization dependence. By formulating in the same coordinates as we discussed for non-

resonant scattering, Eq.(2.14) becomes:

$$f_{nE1}^{XRES} = F^{(0)} \begin{pmatrix} 1 & 0 \\ 0 & \cos 2\theta \end{pmatrix} - iF^{(1)} \begin{pmatrix} 0 & z_1 \cos \theta + z_3 \sin \theta \\ -z_1 \cos \theta + z_3 \sin \theta & -z_2 \sin 2\theta \end{pmatrix}$$
$$+ F^{(2)} \begin{pmatrix} z_2^2 & -z_2(z_1 \sin \theta - z_3 \cos \theta) \\ z_2(z_1 \sin \theta + z_3 \cos \theta) & -\cos^2 \theta(z_1^2 \tan^2 \theta + z_3^2) \end{pmatrix},$$

(2.16)

where θ is the Bragg angle. A similar method applies for the $E2$ transition from $2p_{\frac{1}{2}, \frac{3}{2}} \rightarrow 4f$. Eq.(2.16) suggests that the cross sections in polarization switch channels $\pi - \sigma$ and $\sigma - \pi$ are purely magnetic, clearly separated with a large charge scattering background from the $\sigma - \sigma$ channel. In addition, the resonant enhancement could compensate the loss of intensity while reflected by an analyzer crystal, making the polarization study feasible.

While the scattering from such processes is typically weaker than that due to $E1$ transitions, it can sometimes be significant. For example, the quadrupole terms produce two extra resonant harmonics for incommensurate anntiferromagnets. The result analogous to Eq.(2.16) is more tedious [60]. As we have only used the $E1$ transition in this thesis, we are not going to discuss $E2$ transitions in further detail.

Anisotropic Tensor Susceptibility (ATS) scattering

As mentioned earlier, charge scattering at forbidden Bragg peaks could also be enhanced under resonant conditions. This anomalous scattering has been observed in sodium bromate [65], which breaks a screw-axis selection rule, and Fe_2O_3 [66], which has a C_3 point group at the Fe site. A general reason for forbidden reflections to occur is that the scattering amplitudes of the crystallographically equivalent atoms are not the same due to the small asphericity of the atoms from interatomic inter-actions. This anisotropy is very small in the x-ray region and in conventional x-ray diffraction theories the tensor susceptibility is supposed to be isotropic. However, near x-ray absorption edges the absorption of x-ray beams depends on their polar-izations and, in this case, taking into account the anisotropy of the susceptibility becomes essential [67]. Therefore, at resonant condition, the scattering due to the anisotropic susceptibility tensor (ATS) will have measurable values. The general properties of ATS scattering can be obtained from symmetry considerations [67].

Starting with the most general local relationship between the x-ray electric field $E(r)$ and the polarization of the crystal $P(r)$,

$$4\pi P(r) = \hat{\chi}(r)E(r),$$

(2.17)

where the vector $P(r)$ is not parallel to $E(r)$ due to the anisotropy of the susceptibility. The tensor $\hat{\chi}(r)$ is symmetric: $\chi_{ik}(r) = \chi_{ki}(r); i, k = 1, 2, 3$ and should be invariant under the space group of the crystal. By introducing the tensor structure amplitude $\hat{F}^H$, which is proportional to the Fourier component $\hat{\chi}^H$ of the tensor :

$$\hat{F}^H = -\frac{v}{r_0 \lambda^2}\hat{\chi}^H = \frac{v}{r_0 \lambda^2} \int \hat{\chi}(r) \exp\left(2\pi i H \cdot r\right) dr, \qquad (2.18)$$

where v is the volume of the unit cell, r_0 is the classical electron radius $e^2/(mc^2)$; λ is the x-ray wavelength; and H is the reciprocal-lattice vector. The integration is over the volume of the unit cell. By considering the symmetry operations, Eq.(2.18) will give the properties of scattering amplitude F^{hkl} which typically has the form of $F^{hkl} = F(h, k, l, \theta, \psi)$, where θ is the Bragg angle and ψ is the azimuthal angle [67]. F^{hkl} also has a polarization dependence, analogous to Eq.(2.16).

X-ray optics

From the discussion above, a successful x-ray magnetic diffraction experiment requires the following capabilities from the working station: (1) a bright synchrotron source focused down to 100 µm size to compensate for weak diffraction from a DAC-sized crystal, (2) a full six-circle diffractometer allowing single crystal diffraction in the desired geometry, and (3) an analyzer crystal with high reflectivity and wide enough acceptance angle for polarization studies. I now describe our experimental setup at 4-ID-D of the Advanced Photon Source, Argonne National Laboratory.

A schematic overview of the x-ray setup is shown in Fig. 2.3a. X-rays are generated by circulating electrons in the synchrotron and are $\sim 99\%$ polarized in the horizontal plane. The initial broadband x-rays are monochromatized by two Si(1,1,1) single crystals. For a symmetric Si(1,1,1) monochromator, the x-ray energy resolution is $dE/E \sim 1.32 \ 10^{-4}$ FWHM, which is the major factor in determining the reciprocal space resolution. Finer resolution is possible, at the cost of reductions in the x-ray flux. Using a pair of single crystals brings the monochromatic x-rays to the horizontal direction, improves x-ray energy stability by removing the heat load on the second crystal, and allows a detuning process to remove higher harmonics of the primary x-rays.

The X-ray beam emerges from the monochromator with a typical cross section of 2.5×1 mm^2 and are then focused by a pair of palladium coated mirrors down to 250×120 µm^2, and further cut down by motorized slits to 100×100 µm^2, comparable to the typical sample size in a diamond anvil cell. The Pd coating on the mirror
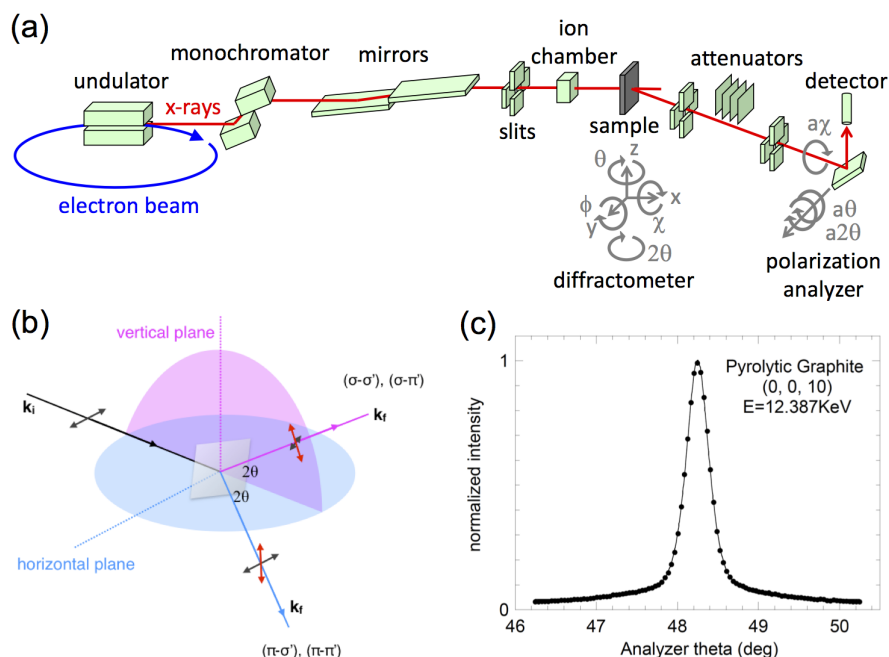
Figure 2.3: Components and schematics of x-ray diffraction. (a) Overall layout of x-ray optical components in the horizontal diffraction geometry; see text for details of the individual elements. Two additional degrees of rotational freedom in the vertical plane are not specified. Note that the extra degree of rotational freedom ϕ of the sample controls its azimuthal condition. (b) Two choices of diffraction geometry. The linearly polarized x-rays from the synchrotron provide either a π (for horizontal diffraction) or a σ (for vertical diffraction) initial condition. (c) Measured mosaic profile (0.35° FWHM) of our 5 mm thick HOPG polarization analyzer for x-rays at the Os L_2 edge.

also effectively rejects higher harmonics. The beam intensity on the high-pressure sample is about 1/8 of that of the unfocused monochromatic x-ray beam emerging from the monochromator.

A Huber 5021 diffractometer with nine circles provides rotational freedom for both the sample and the analyzer, in either the vertical or horizontal planes (Fig. 2.3b). As all of the rotation axes of the diffractometer meet at the sphere of confusion with a radius of about 50 μm, comparable to both the sample size in a diamond anvil cell and the focused x-ray beam cross section (∼100 μm), a set of motorized x-y-z translational stages is necessary to move the sample into the x-ray beam every time a new diffraction order is approached. It is desirable to place the x-y-z stages, such as Huber 5106.20M, inside the last rotational circle to hold a Gifford–McMahon

type cryostat (Sumitomo RDK-205E) with 0.5 W cooling power at 4 K.

There are in general two diffraction geometries for opposing-anvil pressure vessels: a reflection (Bragg) type on the side surface of a plate sample through a Beryllium gasket close to the anvil culet plane [68], and a Laue transmission type through both the sample body and anvils [40, 42]. For the Bragg diffraction geometry, there is very limited reciprocal space access. By contrast, the Laue geometry provides much greater freedom in the azimuthal range and a higher level of tolerance for sample misalignment, both during preparation and from motion inside the pressure chamber during pressurization.

To be sensitive to the weak diffraction signals, it is necessary to use a tight collimation to reject random elastic scattering along the incident x-ray beam path, rather than two-dimensional image plate detectors. We used Huber 3002.60M tuber slits to provide the tight collimation. Single-element x-ray detectors such as NaI based scintillation detectors (CyberStar, Oxford Danfysik) or avalanche photodiodes were used in accordance with the tight collimation.

The polarization analyzer is a standard component of resonant magnetic diffraction. It allows for switching between $\pi - \pi$' and $\pi - \sigma$ channels, and for compensating for movements of both the analyzer and the detector under the Bragg condition to follow energy scans across the resonant edge. To perform polarization analysis of x-rays around 12.4 keV, a 5-mm thick plate of highly oriented pyrolytic graphite (HOPG) was used as the analyzer, due to its spatial uniformity and relatively broad mosaic profile (0.35° FWHM, Fig. 2.3c), which matches the sample mosaicity under pressure. This mosaic width is a compromise between analyzer and samples under pressure to match the angular reception range between them. Methods of keeping the sample mosaic below 0.5° FWHM have been discussed in Section 2.1. The resonant enhancement for magnetic diffraction is typically a factor of 10-1000, which is offset by the low reflectivity (1~2%) of a typical HOPG polarization analyzer.

Resonant x-ray scattering in $Cd_2Os_2O_7$

I have discussed the general behavior of magnetic and ATS scattering at the resonance edge. On one hand, magnetic behavior could be cleanly investigated at the polarization switch channel ($\pi - \sigma$, $\sigma - \pi$) with, however, a potential contamination from the ATS signal, which could be minimized by certain geometric configurations (θ, ψ). On the other hand, the information about orbital and local symmetries conveyed by the ATS resonance ideally should be picked up. In our resonant x-ray

scattering experiment in $Cd_2Os_2O_7$ at the Os L_2 edge (Chapter 5), these two types of resonance have both been addressed.

For $Cd_2Os_2O_7$, which belongs to space group $Fd\bar{3}m$, the selection rule is $h = 4n$ for $(h, 0, 0)$ and $h + k = 4n$ for $(h, k, 0)$. The selection rules are determined by the local inversion symmetry of $16d$ (Cd) and $16c$ (Os) sites. With a $\mathbf{Q} = 0$ antiferromagnetic state, magnetic Bragg peaks overlap with integer diffraction orders and could be observed at lattice forbidden peaks with no azimuthal dependence. In contrast, ATS scattering for $Fd\bar{3}m$, as has been calculated and observed in various systems [63, 64, 69], shows a strong dependence on azimuthal angles and diffraction orders. In our experiment, we performed diffraction in a horizontal geometry to reduce the leakage from charge channel $\sigma - \sigma$ to $\sigma - \pi$. Specifically, we have placed $(6, 0, 0)$ at an azimuthal angle of $45°$, where the ATS signal vanishes at the $\pi - \sigma$ channel [63]. Simultaneously, the diffraction order $(4, 2, 0)$, with $\psi \sim 50°$, manifests an ATS signal in the $\pi - \sigma$ channel which is one order of magnitude stronger than that from magnetic diffraction. In this way, the magnetic and ATS resonances are cleanly separated. The resonant scattering cross sections have very small $\pi - \pi'$ components (Eq.(2.16)) [69], leaving the polarization non-switch channel a sensitive indicator of lattice scattering.

2.3   Optical Raman spectroscopy under high pressure

Raman spectroscopy is a powerful technique to characterize the elastic, vibrational, electronic, and magnetic properties by utilizing inelastic scattering process of a light source, usually a laser, from the near UV to the near IR range. It is most sensitive to phonon modes, which provide information about the symmetry of the crystal structure. Combined with high pressure and cryogenic sample environment, it enables a quick determination of phase transitions [70]. Using the commercial high-resolution Raman microscope (LabRAM HR Evolution, Horiba, Ltd.), we have customized an optical flow-helium cryostat (CryoIndustry) with a cold stage to host our high-pressure cells and membrane line to change pressure in situ. A small 3-pin cell (Fig. 2.1) of 37 cm diameter was built to be compatible with the stage size. An objective with a long working distance of 20 mm and relatively large numerical aperture of 0.42 (20X Mitutoyo Plan Apochromat Objective, N. A. 0.42, 20 mm WD) was used to allow focusing on the sample in the pressure chamber through the cryostat window and a diamond anvil. We chose a 632 nm laser considering both efficiency for Raman spectroscopy and ruby fluorescence, as well as background issues. The complete experimental set up is shown in Fig. 2.4.
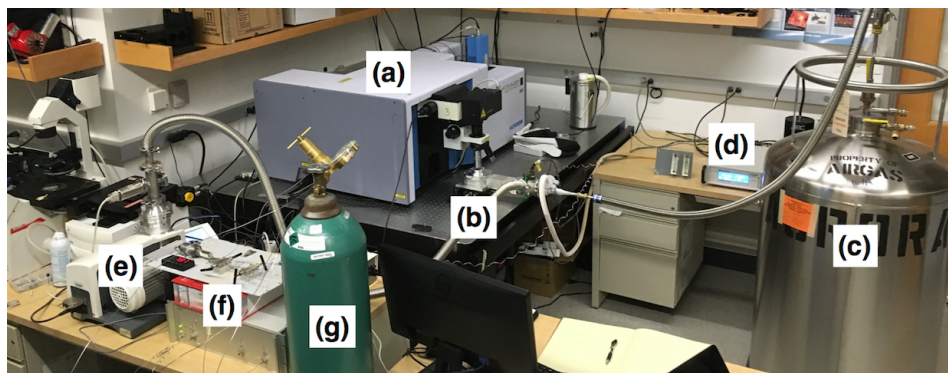
Figure 2.4: High pressure, low temperature Raman setup. Components in the picture: (a) commercial Raman microscope; (b) He-4 flow cryostat; (c) liquid helium dewar; (d) Lakeshore temperature controller; (e) vacuum pump; (f) high pressure manifold control system; (g) high pressure helium gas bottle, providing gas to change cell pressure.

As our most commonly used pressure medium, the mixture of methanol and ethanol, generates active vibrational modes from molecular interactions, it is not ideal for a Raman experiment. Instead, noble gases such as helium, neon, and argon, which are single atom molecules, are more desirable. Helium provides the best pressure conditions at low temperature [71]; the volume of the pressure chamber, however, collapses significantly. By comparison, argon will maintain the chamber size better, but the pressure condition degrades quickly with higher pressure [71]. We have tried loading with liquid argon, finding Raman peaks broadened by a factor of 2 from 0 to 8.8 GPa. Considering these effects related to atom mass, we finally chose neon as the pressure medium. The gas loading system of GSECARS at the Advanced Photon Source [43] was used to load high pressure neon gas into the chamber. Real-time views of the pressure chamber and in situ ruby measurements are available while sealing the cell with a clamping mechanism.

[1]Resonant x-ray magnetic diffraction under high pressure is a technique developed during this thesis.

[2]Optical Raman spectroscopy at low temperature under high pressure is a technique further developed during this thesis

[3]Electrical transport could be used to measure the power law behavior of the resistivity, which is an established technique but not included in the projects of this thesis.

Chapter 3

MAGNETISM, STRUCTURE AND SUPERCONDUCTIVITY IN Mo_3Sb_7

The interplay of multiple degrees of freedom in correlated electron systems is profoundly manifested in superconductivity, where electrons can be paired either through electron-phonon coupling or spin fluctuations. Using high pressure as a tuning method of competing ordering mechanisms, we have studied the intricate interaction of structure, magnetism, and superconductivity in the $4d$ intermetallic compound Mo_3Sb_7.

Synchrotron x-ray diffraction and magnetic susceptibility measurements, both employing diamond anvil cell technologies, link a first-order structural phase transition to a doubling of the superconducting transition temperature. In contrast to the spin-dimer picture for Mo_3Sb_7, we deduce from x-ray absorption near-edge structure and dc magnetization measurements at ambient pressure that Mo_3Sb_7 should possess only very small, itinerant magnetic moments. The pressure evolution of the superconducting transition temperature strongly suggests its enhancement is due to a difference in the phonon density-of-states with changed crystal symmetry.

The discussion below follows *Phys. Rev. B* **95**, 125102 (2017).

3.1 Introduction

The magnetism and superconductivity combined with crystal structure in the $4d$ intermetallic compound Mo_3Sb_7 captures both the excitement and the difficulty of understanding the emergence of collective quantum states. Examples range from metal-insulator transitions [72] to density waves [8] to superconductors [30, 73–77]. In Mo_3Sb_7 itself, superconductivity emerges below a structural phase transition with claims of accompanying magnetic order and spin dimerization [78–80], potentially placing it in a growing cohort of exotic superconductors with unconventional pairing mechanisms [30–33].

Mo_3Sb_7 goes superconducting at T_c = 2.35 K, with a structural phase transition from high-temperature cubic symmetry to low-temperature tetragonal symmetry at T_S = 53 K [78–80]. Whether this structural transition is magnetically driven is still an open question [78–81], although no long-range spin order has been observed

through either neutron or x-ray magnetic diffraction [80]. Magnetic susceptibility measurements give one $S = 1/2$ local moment per Mo site from fits to a Curie-Weiss law at high temperature [78–80], with spin gap behavior at low temperature that suggests a spin-Peierls transition at T_S [79, 80]. The presence of shortened Mo-Mo bond distances in the tetragonal phase [80] reinforces the idea that one-third of the Mo ions form dimers below T_S [79, 80]. A valence bond crystal also has been suggested as a possible ground state amid strong spin frustration [78]. The superconductivity has been claimed to be s-wave at ambient pressure [82–84], but the possibility of unusual magnetic phases at low temperature [78–81] have raised the question about the role of spin coupling.
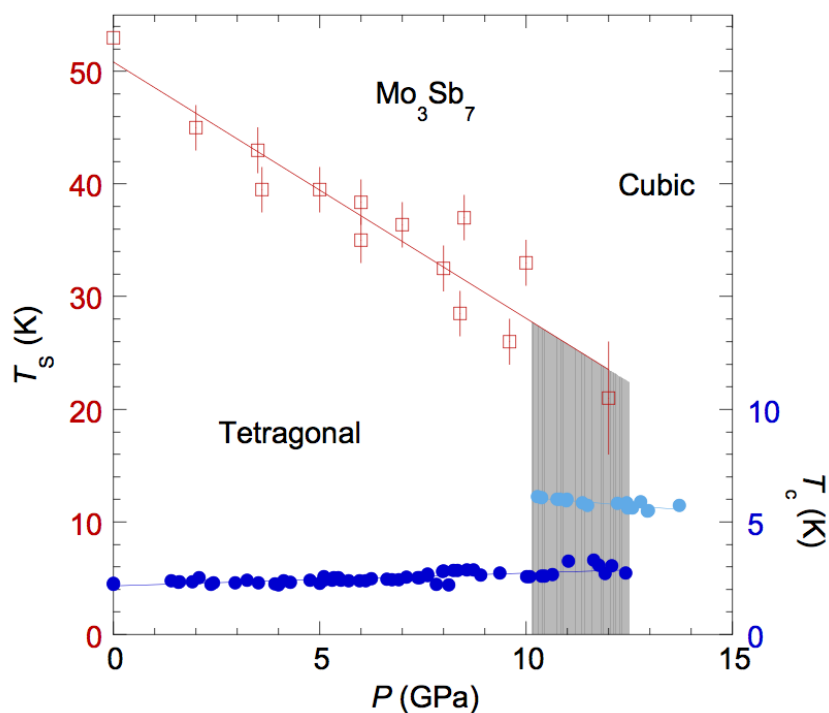
Figure 3.1: $P - T$ phase diagram of Mo_3Sb_7. Red squares mark the phase boundary between tetragonal and cubic structures at $T_S(P)$, as determined from electrical resistivity [85]. Superconducting transitions (dark and light blue circles) in both crystal structures are demarcated by characteristic signatures of the magnetic susceptibility. The shaded area marks the phase coexistence region.

Chemical doping has been exploited previously to study superconductivity in Mo_3Sb_7 [81, 86]. We combine x-ray diffraction and ac magnetic susceptibility measurements up to 17 GPa of applied pressure to examine the nature of the superconductivity in Mo_3Sb_7. Thereby, we show that hydrostatic pressure is a particularly effective tuning mechanism, and we find a second superconducting state with a factor of

two greater T_c following a pressure-induced first-order phase transition to a higher structural symmetry phase (Fig. 3.1). The high-pressure phase is cubic and continuously connects to the ambient-pressure, high-temperature paramagnetic phase. By contrast to previous suggestions of spin-dimer magnetic order in a local spin picture [78], we argue that spins in Mo_3Sb_7 should be considered as both highly itinerant and small in magnitude. The link of T_c to structure suggests that spin fluctuations are not a dominant coupling mechanism in this system, while the abrupt variation in T_c points to a symmetry-related difference in the phonon density-of-states.

3.2   Experimental methods

Mo_3Sb_7 single crystals of several mm in size were grown using a Sb self-flux technique [80]. Single crystals were polished down to plates of 20 - 30 µm thickness with a surface normal of (1, 0, 0) and broken into small shards (120 $\times$ 120 $\times$ 20 µm^3) to be loaded into the diamond anvil cell. The ac magnetic susceptibility measurements at a probe field of 0.5 Oe were carried out using a diamond anvil cell designed for rapidly exploring $H - P - T$ parameter space [42]. Sapphire seats and thermally hardened BeCu or MP35N gaskets were used to avoid any ferromagnetic background disturbance to the superconducting transition [42, 87]. Four different crystals were studied in a methanol:ethanol = 4:1 hydrostatic pressure medium. Pressure was monitored by ruby fluorescence *in situ* at low temperature [40]. X-ray absorption and high-pressure diffraction measurements were carried out at Sector 4-ID-D of the Advanced Photon Source. X-ray absorption was performed at ambient pressure and temperature, using single crystal Mo_3Sb_7 along with annealed Mo metal foil and MoO_2 and MoO_3 powders. For diffraction, 19.950 keV x-rays were used in order to avoid the Mo K edge fluorescence. The methanol:ethanol 4:1 mixture was used as the pressure medium, and a piece of polycrystalline silver foil was included as a manometer at low temperature [40]. The ambient-pressure magnetization was measured using a superconducting quantum interference device (SQUID) magnetometer (Quantum Design Magnetic Property Measuring System) on a cubic shaped single crystal of 0.0138 g along the (1, 1, 0) direction and at both $T = 60$ and 6 K, bracketing the phase transition at T_S.

3.3   Results

The pressure evolution of superconductivity in Mo_3Sb_7 was measured using ac magnetic susceptibility (Fig. 3.2). From 0 to 10 GPa, T_c slowly increases from 2.3 to 3 K with increasing P. Starting at 10 GPa, a new superconducting phase was observed
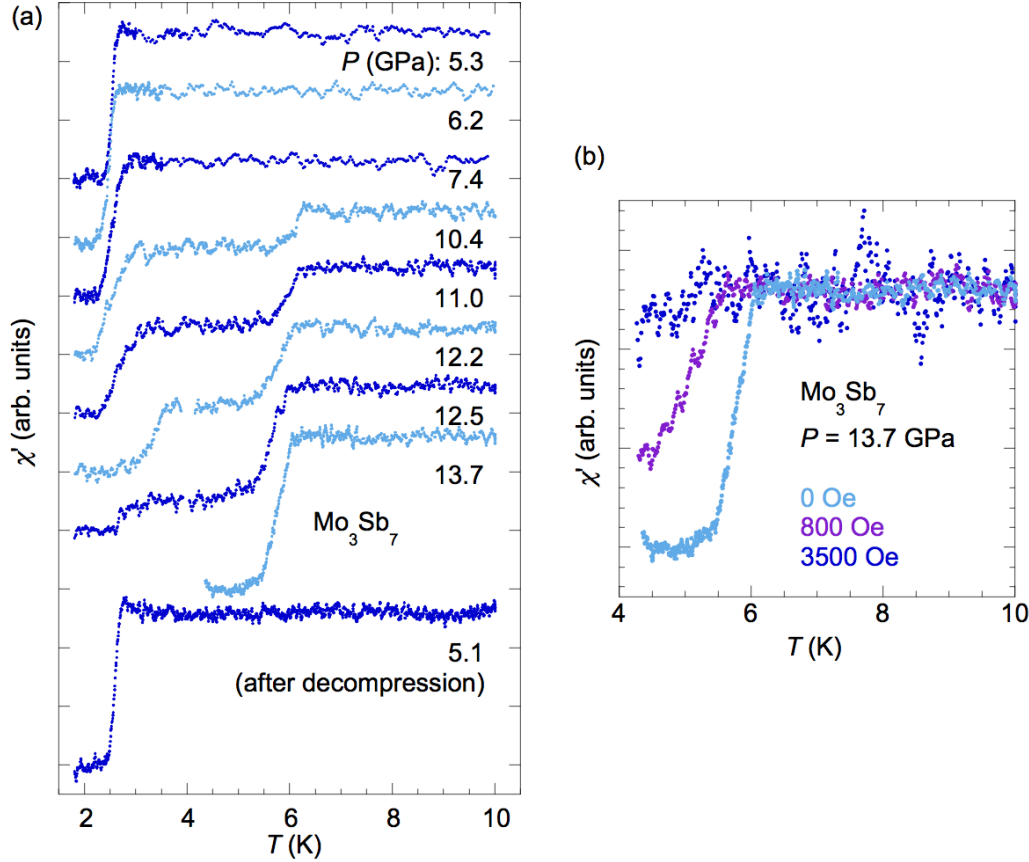
Figure 3.2: The ac magnetic susceptibility in Mo_3Sb_7. (a) The ac magnetic susceptibility at the superconducting transition at a series of pressures P in Mo_3Sb_7. The two-step transitions indicate phase coexistence. (b) An applied magnetic field suppresses the superconductivity.

with $T_c \sim 6$ K, a jump of a factor of two. This quantum phase transition between two superconducting states is clearly first order, with susceptibility manifesting two superconducting steps as a sign of phase coexistence over a wide pressure region (Fig. 3.2a). As expected, an external magnetic field suppresses the superconducting transitions (Fig. 3.2b).

Turning to structural information, the phase boundary $T_S(P)$ was tracked by macroscopic probes such as the electrical resistivity [85], where $T_S(P)$ is suppressed by increasing pressure (Fig. 3.1), but only slowly ($\sim$2.5 K/GPa), remaining well above zero out to 12 GPa. We performed a set of x-ray diffraction measurements to specify the evolution with P of the microscopic structure and associated lattice symmetries. Longitudinal diffraction line scans of various lattice orders such as (4, 0, 0), (4, 4, 0), and (4, 4, 4) at $T = 4$ K (Fig. 3.3(a)) indicate a lattice symmetry change from
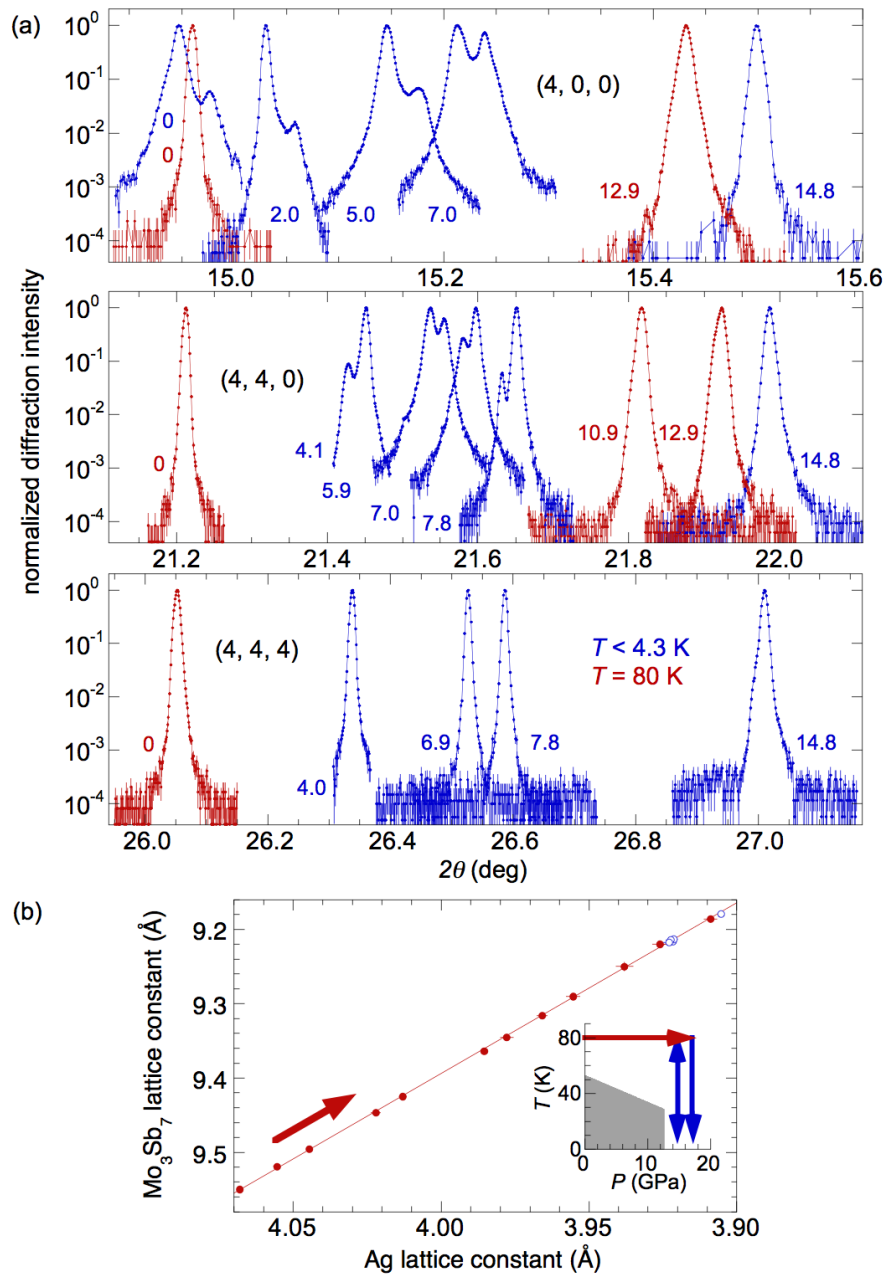
Figure 3.3: Lattice symmetry and phase continuity. (a) Longitudinal ($\theta/2\theta$) scans of three lattice orders of Mo_3Sb_7, measured for various pressures (in units of GPa) at $T = 80$ K (red) or $T < 4.3$ K (blue). All scans are plotted on a logarithmic scale in order to show the symmetry state and to rule out the presence of minor phases. (b) The Mo_3Sb_7 lattice constant vs Ag lattice constant at each (P, T) point along the specified path in the inset. (Inset) Trajectory in the $P - T$ phase space for x-ray measurements. Mo_3Sb_7 remains in the same cubic phase throughout. The bulk modulus at 80K is $B_0 = 111.5 \pm 0.8$GPa.

tetragonal at low pressure to cubic at high pressure. We examine in Fig. 3.3(b) the relationship between this high-pressure, low-temperature cubic phase and the ambient pressure, high-temperature cubic paramagnetic phase by traversing the $P - T$ phase diagram for $T > T_S$ out to $P = 17.1$ GPa. The lattice constants of both Mo3Sb7 and the silver manometer were measured at various (P, T) points along the path and then compared to each other. We find that $a_{\mathrm{Mo_3Sb_7}}(P, T)$ vs $a_{\mathrm{Ag}}(P, T)$ collapses onto a straight line throughout the trajectory. Hence the cubic phase of $\mathrm{Mo_3Sb_7}$ at high P and low T and the cubic phase at $P = 0$ and $T > T_S$ are continuous, ruling out the separation that would result from a sudden unit cell collapse in an isostructural phase transition.

Given the continuous evolution of the ambient pressure paramagnet above $T_S = 53$ K to high pressure and low temperature, we might expect the spins in the high-pressure cubic phase of $\mathrm{Mo_3Sb_7}$ to remain disordered. Spin fluctuations in $\mathrm{Mo_3Sb_7}$ have been discussed in the literature based on the assumption of one $S = 1/2$ local moment per Mo site [79, 80]. However, the existence of magnetic moments in Mo compounds strongly depends on its ionic state and local symmetry. For example, $\mathrm{Mo^{4+}}$ carries a moment of $S = 1$ in $1T\text{-}\mathrm{MoS_2}$ but no moment in $2H\text{-}\mathrm{MoS_2}$ due to a different splitting of the $4d$ orbitals by local symmetries [81]. In $\mathrm{Ba_2YMoO_6}$ [88], a $\mathrm{Mo^{5+}}$ state leads to a localized $S = 1/2$ moment, which also was assumed for $\mathrm{Mo_3Sb_7}$ [78]. The ionic state of Mo in $\mathrm{Mo_3Sb_7}$ can be determined by x-ray absorption near-edge structure (XANES) measurements [89]. In the cubic phase of paramagnetic $\mathrm{Mo_3Sb_7}$, there is only one unique Mo site in the unit cell [80], and the measured XANES K edge of $\mathrm{Mo_3Sb_7}$ is very similar to that of pure Mo metal (Fig. 3.4a), lying 10 - 15 eV away from the K edge of both $\mathrm{Mo^{4+}}$ in $\mathrm{MoO_2}$ and $\mathrm{Mo^{6+}}$ in $\mathrm{MoO_3}$. This suggests that the Mo ions in $\mathrm{Mo_3Sb_7}$ are close to charge neutral. They are also unlikely to have valence fluctuations like those displayed by highly ionized $\mathrm{Re^{5+}}$ ions in $\mathrm{Cd_2Re_2O_7}$ [90].

We plot in Fig. 3.4(b) the dc magnetization, $M(H)$, at ambient pressure. It is linear and nonsaturating at both $T = 60$ and 6 K, above and below T_S, without hysteresis for applied fields between ± 7 T. Since $\mathrm{Mo_3Sb_7}$ is cubic in the paramagnetic phase, no strong anisotropy of $M(H)$ is expected along the major crystalline axes. Here the nonsaturating $M(H)$ of $\mathrm{Mo_3Sb_7}$ differs from the isothermal magnetization behavior of many magnetic Mo compounds. For ferromagnetic and paramagnetic $\mathrm{MoS_2}$ [81, 91] and ferromagnetic $\mathrm{GaMo_4S_8}$ and $\mathrm{GaMo_4Se_8}$ [92, 93], $M(H)$ would saturate at relatively low fields, typically < 3 T. At $H = 7$ T, there is no saturation, and the
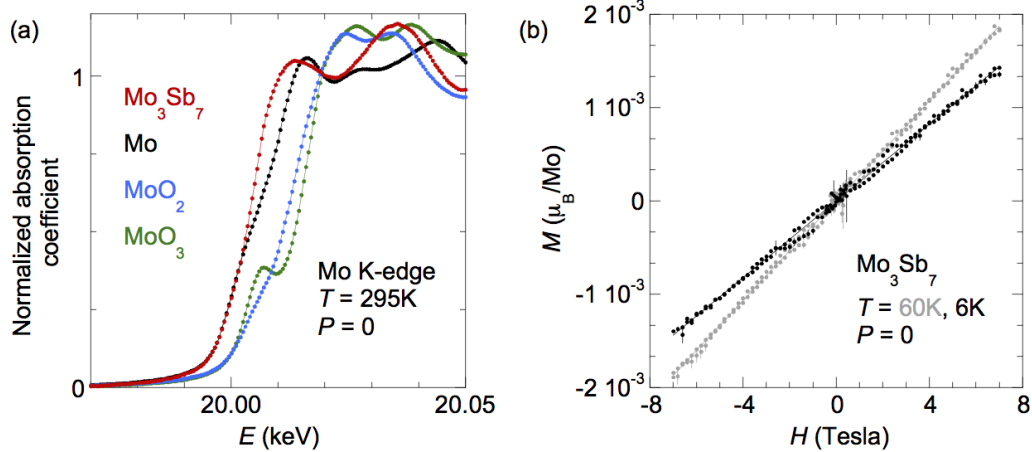
Figure 3.4: Chemical and magnetic characteristics of Mo_3Sb_7. (a) X-ray absorption near-edge spectroscopy at ambient conditions for a comparison between four different Mo compounds of various valence conditions. (b) Magnetization measurements $M(H)$ at $T = 60K$ and 6 K, bracketing T_S at $P = 0$, indicate no magnetic hysteresis and no saturation up to $H = 7$ T.

measured moment is extremely small: 2×10^{-3} μ_B/Mo. This small and unsaturated moment of Mo_3Sb_7 derived from $M(H)$ contrasts sharply from the magnetic moment deduced from the paramagnetic susceptibility, $\chi'(T)$. Fitting to a Curie-Weiss law for 230 K < T < 700 K yields a local moment of 1.56 ± 0.10 μ_B/Mo, consistent with $S = 1/2$ moment per Mo site [79, 80]. The discrepancy between the values of the magnetic moment following from the magnetization at 7 T and fits to the magnetic susceptibility gives a Rhodes-Wohlfarth ratio ~500. This indicates that the Curie-Weiss behavior is due to band structure effects rather than localized spins [9]. Indeed, the shortest Mo-Mo distance in Mo_3Sb_7 is 2.98 Å[80], a distance similar to the value of 2.73 - 2.9 Å in elemental Mo and ferromagnetic $GaMo_4S_8$ and $GaMo_4Se_8$ [92], where the overlap of $4d$ orbitals results in the electrons being considered as itinerant [92–94]. The combination of the valence state (Fig. 3.4a) and magnetization (Fig. 3.4b) measurements therefore permits us to conclude that the spins in Mo_3Sb_7 are highly itinerant and very small in magnitude. The magnetic nature of the tetragonal phase in Mo_3Sb_7 is consistent with paramagnetism (Fig. 3.4b); the temperature dependence of the magnetic susceptibility at ambient pressure [79, 80] could be due to a structural phase transition with no magnetic correlation, similar to that in $Cd_2Re_2O_7$ [90]. Hence we do not expect that the localized spin-dimer picture should be applicable to either phase of Mo_3Sb_7.

3.4 Discussion and conclusion

The superconducting transition in Mo_3Sb_7 lacks significant pressure dependence in either the tetragonal or cubic phase, leading to an abrupt doubling of the transition temperature at the phase boundary (Fig. 3.1). While the connection between superconductivity and structural symmetry is particularly prominent, the crystal symmetry dependence of superconductivity is opposite to the typical expectation for spin-fluctuation-mediated superconductivity, which is believed to benefit more from a tetragonal structure than a higher symmetry cubic phase [30]. An increasing tetragonal distortion drives the system closer to the two-dimensional limit and hence enhances spin fluctuations via a diverging $\chi_m(q, \omega)$. This trend has been observed in heavy fermion superconductors; for example, T_c is significantly larger in tetragonal $CeRhIn_5$ than in cubic $CeIn_3$ [30]. Here in Mo_3Sb_7, T_c in the high-symmetry cubic phase doubles that in the low-symmetry tetragonal phase, while both structures are stable ground states. Symmetry considerations thus favor phonon-mediated superconductivity in Mo_3Sb_7 at high pressure.

Analogous to the original BCS formula in the weak coupling limit, T_c is expressed in McMillan's formula for intermediate phonon-coupling strength [84, 95, 96] as:

$$T_c = \frac{\Theta}{1.45} \exp\left(-\frac{1.04(1 + \lambda)}{\lambda - \mu^*(1 + 0.62\lambda)}\right), \tag{3.1}$$

with the Debye temperature, Θ, dimensionless electron-phonon coupling constant, λ, and screened Coulomb potential, μ^*. While all three could potentially vary under pressure to account for the T_c evolution, both the constancy of the superconducting transition within each structural phase and its discontinuous nature in the phase coexistence region strongly suggest that the cause can be identified by comparing two structural phases of different symmetries at the same pressure. From calculations at ambient pressure [95], it is reasonable to assume that both Θ and μ^* are nearly identical in the tetragonal and cubic phases at the same pressure in the phase coexistence region. We therefore believe that the main influence on T_c should come from the electron-phonon coupling constant λ, with λ dependent on both electronic structure and the phonon dispersion spectrum [96]. The smoothly varying resistivity under pressure [85] indicates a continuously evolving electronic structure, consistent with an estimated small difference between the tetragonal and cubic structures by theoretical calculation at ambient pressure [95]. Hence the origin of the doubled T_c most likely arises from details of the symmetry-dependent phonon dispersion [96]. This causes λ to grow from 0.55 at ambient pressure [84, 95] to 0.75 in the cubic phase.

Spin fluctuations in general would disrupt a phonon-coupled superconductor by suppressing the value of λ [84] and thereby T_c. All suggested forms of singlet magnetic correlations (either long range antiferromagnetic order or spin-dimer pairs) in the tetragonal phase would introduce reduced singlet-type spin fluctuations as compared to fluctuations in the spin-disordered, high-pressure phase. This dearth of spin fluctuations in the tetragonal phase is consistent with the fact that $\rho(T)$ does not manifest $T^{3/2}$ behavior at ambient pressure [79, 80, 97]. If spin fluctuations would affect the phonon-mediated superconducting state in Mo_3Sb_7 [97], then $T_c(P)$ should be suppressed in the spin-disordered cubic high-pressure phase, while the experiments demonstrate the opposite.

In summary, pressure enhances the superconducting transition temperature in Mo_3Sb_7 by a factor of two, accompanied by a first-order phase transition from tetragonal to cubic lattice symmetry at low temperature. Direct x-ray diffraction results reveal that the high-pressure cubic phase continuously evolves from the paramagnetic phase at ambient pressure and is expected to be spin disordered. However, given the relatively small itinerant moments and weak spin fluctuation effects, we attribute the increase of T_c to a modified phonon density-of-states in the high-symmetry cubic structure. We are able to draw this conclusion because of the combination of magnetic, electronic, and structural measurements and the ability to tune different lattice symmetries with pressure. This general approach is necessary to parse the competition between different pairing mechanisms in materials with tendencies towards both magnetic and superconducting order.

Chapter 4

SPIRAL MAGNETIC ORDER AND SUPERCONDUCTIVITY IN MnP

It has been more than 30 years since the discovery of high-T_c superconductivity, yet the microscopic mechanism for unconventional superconducting order in the cuprates is still not clear. The similar phase diagram connecting a magnetically ordered state to a superconducting state has been discovered in other systems, potentially suggesting alternative magnetic origins for Cooper pairing. Experiments providing microscopic information about magnetism in clean model systems are beneficial in addressing this topic.

Using a synchrotron-based non-resonant x-ray magnetic diffraction technique, we reveal a spiral spin order in MnP and trace its pressure evolution towards superconducting order via measurements in a diamond anvil cell. Judging from the magnetostriction, ordered moments vanish at the quantum phase transition as pressure increases the electron kinetic energy. Spins remain local in the disordered phase, and the promotion of superconductivity is likely to emerge from an enhanced coupling to residual spiral spin fluctuations and their concomitant suppression of phonon-mediated superconductivity. As the pitch of the spiral order varies across the $3d$ transition metal compounds in the MnP family, the magnetic ground state switches between antiferromagnet and ferromagnet, providing an additional tuning parameter in probing spin-fluctuation-induced superconductivity. The discussion in this chapter follows *Nat. Commun.* **7**, 13037 (2016).

4.1 Introduction

Magnetic materials have played an outsized role in revealing the shape of the world around us. The similarly venerable field of superconductivity serves as a prime example of emergent, collective behavior in nature, with raised hopes of technological import with the discovery of exotic superconducting order in the cuprates. Magnetism and superconductivity often compete for preeminence as a material's ground state, but in the right circumstances the fluctuating remains of magnetic order can induce superconducting pairing. The intertwining of the two on the microscopic level, independent of lattice excitations, is especially pronounced in heavy fermion compounds [21], rare earth cuprates [98], and iron pnictides [99].

The recent discovery of a superconducting phase in the transition metal compound MnP [100] opens the possibility of investigating this scenario. MnP possesses a complex pressure-temperature ($P-T$) phase diagram [100] (Fig. 4.1). At ambient pressure, there is helical spin order below $T_N = 50$ K, with a wave vector $\boldsymbol{Q} = (0.117, 0, 0)$ [101]. Under pressure, the helical order is quickly replaced by ferromagnetism at ~1 GPa, and another magnetic state, assumed to be antiferromagnetic [100], emerges for $P > 2$ GPa. Superconductivity appears after the high-pressure magnetic phase is suppressed at $P \sim 7$ GPa [100]. The spin structure in the high-pressure magnetic phase remains unsettled, and is under active exploration by both x-ray and neutron [102] magnetic diffraction techniques.
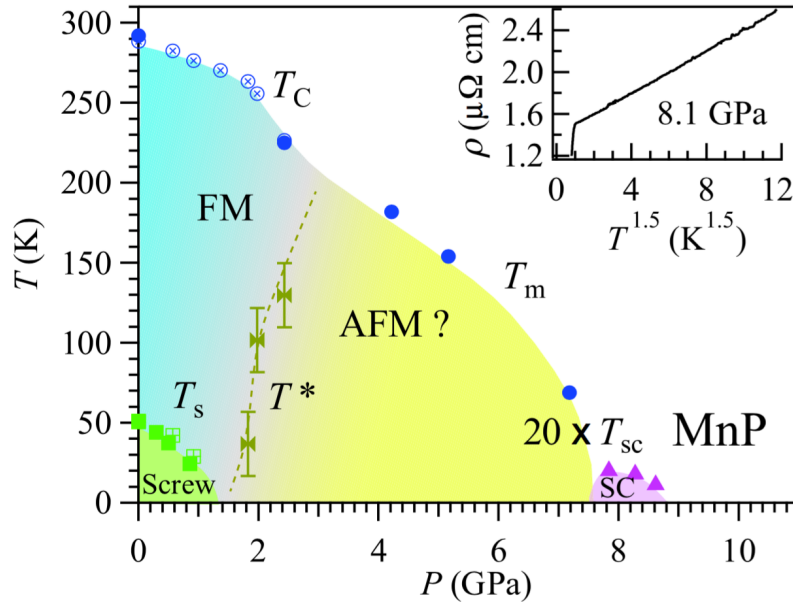
Figure 4.1: $P-T$ phase diagram of MnP from Ref. [100]. Pressure dependence of the magnetic transition temperatures, T_C, T_m, T^*, T_S, and the superconducting transition temperature T_{SC}; T_{SC} has been scaled by a factor of 20 for clarity.

We employ synchrotron-based magnetic x-ray diffraction to investigate the high-pressure magnetic phases in MnP [100]. This sensitive probe, suitable for 0.0002 mm^3 single crystal volumes and diamond anvil cell techniques, directly reveals a reduced moment, incommensurate spin state at high pressure proximate to the superconducting state. This new magnetic order is most likely a magnetic helix with a tightened pitch in comparison to that at ambient pressure where superconductivity is absent. The extant data correlating magnetic pitch length and superconductivity is sparse but suggestive in the (V/Cr/Mn/Fe/Co/Ni)(P/As/Sb) family [100, 101, 103–

116] and, as discussed in detail below, we suggest this family of spiral magnets as a new venue for tunable, spin-fluctuation-mediated superconductivity.

Here we point out that for a helical arrangement of localized spins, a variable spiral period could provide a unique tuning process from ferromagnetic to antiferromagnetic ground state in the long and short wavelength limits, respectively. Such chemical or pressure adjustable helical order naturally provides the possibility for continuous tuning between ferromagnetically- and antiferromagnetically-mediated superconductivity. At the same time, phonon-mediated superconductivity is suppressed because of the local ferromagnetic spin configuration [117] in the low-frequency spiral fluctuation modes.

4.2   Experimental methods

Following the general principle of non-resonant x-ray magnetic diffraction that has been discussed in Chapter 2, we can estimate the scattering cross section $\sigma_{\mathrm{mag}}/\sigma_{\mathrm{charge}}$ in this experiment. MnP is a $3d$ transition metal compound with low local symmetry at the Mn sites. Thus it is reasonable to assume that the orbital moments are quenched in this system. Spins localized at Mn sites, as suggested by our measured Rhodes–Wohlfarth ratio, are the major source of magnetism. For MnP, with $N = 25$ for Mn, and a projected spin moment s about $1.3/\sqrt{2}\mu_{\mathrm{B}}$, $\sigma_{\mathrm{mag}}/\sigma_{\mathrm{charge}}$ is estimated to be 2-5 $\times 10^{-8}$ for $I_{(1\pm\mathrm{Q}\,,\,0,\,0)}$ / $I_{(2,\,0,\,0)}$. This value becomes smaller as the ordered moment, $\langle m \rangle$, decreases with increasing pressure.

4.3   Results

We performed non-resonant single crystal X-ray magnetic diffraction under pressure [40, 42, 118] to elucidate the cascade of magnetic states in the $P - T$ phase diagram of MnP (Fig. 4.1) and their relation to superconductivity. We discover helical magnetic order with $\boldsymbol{Q}$'= (0.25, 0, 0) presaging the high-pressure superconductor (Fig. 4.2). We observe a pair of superlattice peaks in mirror symmetry to the lattice order at three pressures, 3.17, 5.28 and 6.43 GPa, but absent at P = 8.99 and 10.4 GPa. Lattice line shapes are instrument resolution limited for the whole pressure range, and can be fit to a Pseudo-Voigt form with a lattice coherence length exceeding 1500 Å. The magnetic peaks are significantly broadened, indicating a shorter correlation length of the helical spin order from ~310 Å at 3.2 GPa to ~70 Å at 6.4 GPa, about three times the pitch length of 24 Å. All magnetic peaks are fit with a Lorentzian form on a sloped background, which could be attributed to influence from spin fluctuations in the ordered phase. However, our counting statistics are not
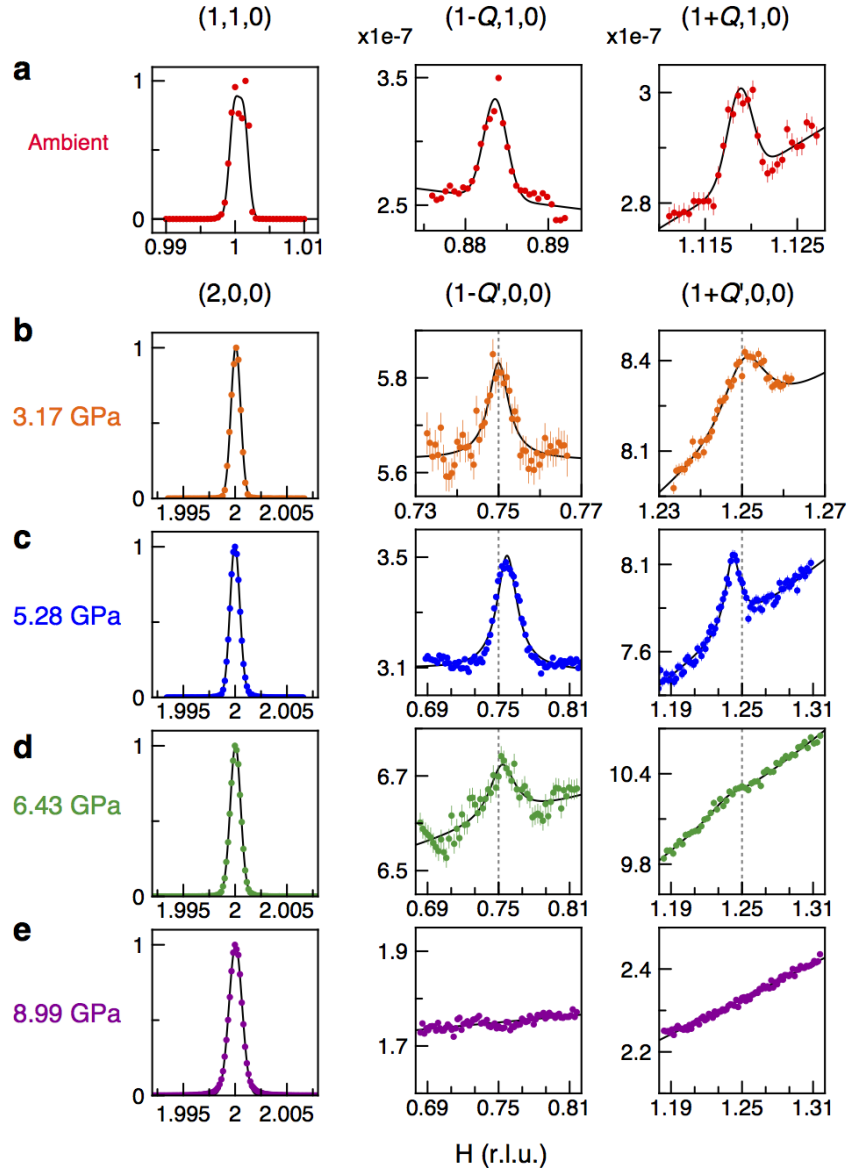
Figure 4.2: X-ray diffraction evidence of helical order in MnP. (a) Raw scans around the (1, 1, 0) order at ambient pressure and $T = 4$ K, showing both the lattice Bragg peak and a pair of non-resonant magnetic peaks associated with the helical spin order Ha-I. Solid lines are guides to the eye. (b–d) Longitudinal ($\theta/2\theta$) line shapes of (2, 0, 0) lattice, and (1±Q', 0, 0) helical magnetic order, measured at $T = 4$ K. We set $a > b > c$ in the *Pbnm* space group for the lattice [101]. Vertical dashed lines mark the commensurate (0.75, 0, 0) and (1.25, 0, 0) positions. (e) Above P_c = 6.7 GPa, magnetic diffraction is no longer observed in longitudinal scans at same positions of b–d. Vertical error bars represent 1σ s.d. counting statistics.

sufficient to make a distinction from a Lorentzian-squared form, which results from disorder pinning [119]. The reduced background benefits from the use of a pair of

wide-angle perforated diamond anvils [24, 42]. Our instrument resolution is fine enough to indicate that the observed magnetic pairs are mirror symmetric to the (1, 0, 0) order, but not commensurate. The presence of mirroring peaks around (1, 0, 0) indicates the *n*-glide plane constraint is broken for the spin arrangement at high pressure [101], although the (1, 0, 0) lattice order is still forbidden.
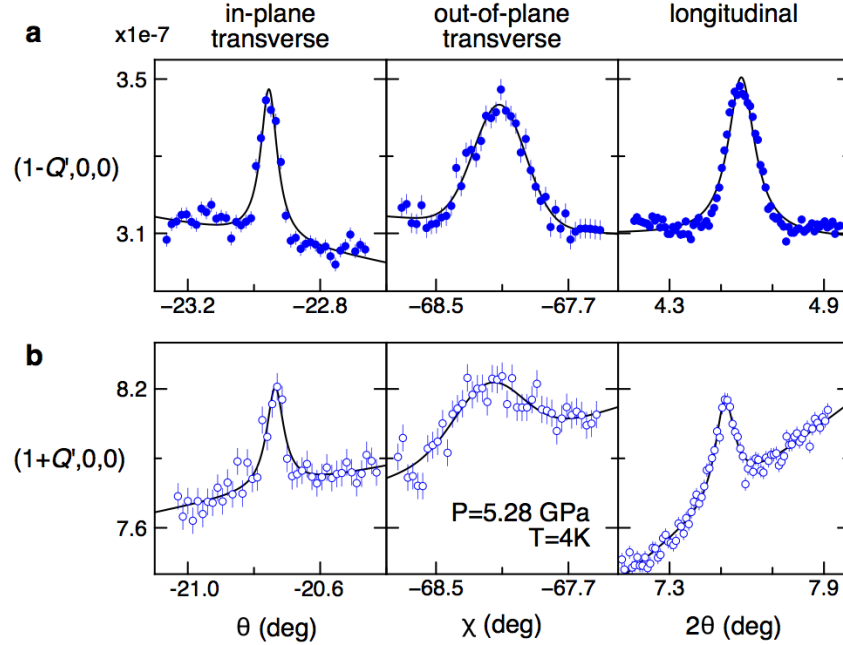
Figure 4.3: Single crystal nature of the magnetic order at $P = 5.28$GPa. The single crystal nature of the magnetic order is proven by independent raw scans across the 3D reciprocal space for both (1-Q', 0, 0) and (1+Q', 0, 0) orders. The out-of-diffraction-plane transverse scan is dominated by the resolution function determined by the wide horizontal detector slits, while the in-plane transverse scan is intrinsic to the sample mosaic (full-width at half-maximum~0.1°) under pressure. The longitudinal scans are of the $\theta/2\theta$ type (plotted against 2θ here) and identical to those in Fig. 4.2c. Measurements were performed at $T = 4$ K. Vertical error bars represent 1σ s.d. counting statistics. Solid lines are guides to the eye.

These diffraction peaks are always of single crystal nature (Fig. 4.3) and their pressure evolution is commensurate to that of the *a* axis. Here we adopt the *Pbnm* space group setting for MnP with $a > b > c$ [101] The low transferred momentum of (1±Q', 0, 0) rules out diffraction from integer lattice orders from both MnP and other components of the high-pressure cell (diamond and Ag manometer) [40, 42, 120, 121]. The peak intensities lie in the range of 1 - 4 10^{-8} relative to the (2, 0, 0) lattice intensity, which are comparable with the estimate of non-resonant magnetic diffraction intensities and the observed diffraction signal of the low-pressure helical

order under the same experimental condition (Fig. 4.2a). It is known that spin order can induce higher harmonics [122, 123]. However, we did not observe a diffraction peak at (1±Q'/2, 0, 0) with commensurate sensitivity (Fig. 4.4). This implies that our observed pair of peaks represents the primary wave describing the spin order. We did not observe diffraction intensity at (1±2Q', 0, 0), thereby ruling out a strong charge harmonic to the magnetic order.
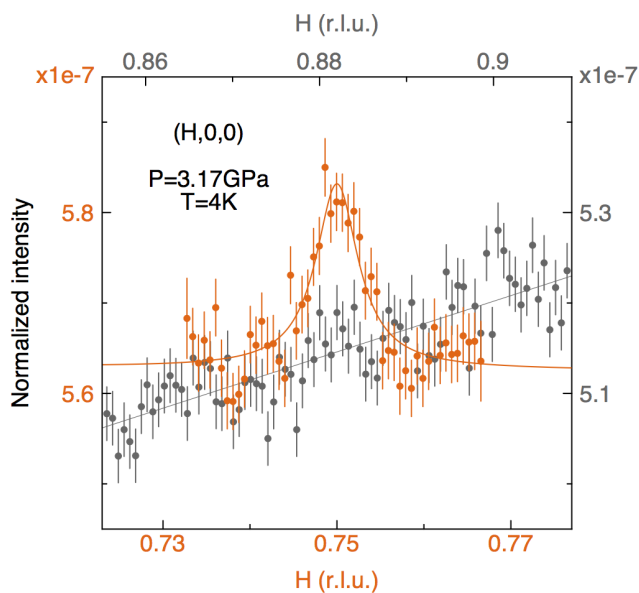
Figure 4.4: Primary wave nature of the observed diffraction order. A comparison of longitudinal scans between the observed (1-Q', 0, 0) order and null (1-Q'/2, 0, 0) position. This indicates that our observed peaks are primary waves and not higher harmonics of another wave vector. The longitudinal scan of (1-Q', 0, 0) is identical to the data in Fig. 4.2b. Vertical error bars represent 1σ s.d. counting statistics.

Our limited number of observed diffraction orders and the lack of a full azimuthal study because of constrained high-pressure cell geometry make it insufficient to fully refine the high-pressure spin structure. However, in our diffraction geometry, the non-resonant magnetic cross section for orders along the $(H, 0, 0)$ direction is only sensitive to magnetic moments projected out of the vertical diffraction plane and transverse to the wave vector $\boldsymbol{Q}$' (Chapter 2 and Chapter 4.2). With spin moments localized in Mn (see below) and an incommensurate wave vector in MnP, the magnetic order is not likely to be of a collinear, amplitude-modulated type. Thus it is reasonable to identify the magnetism in MnP as helical order with tightened pitch (Ha-II, Fig. 4.5 inset). This provides a consistent perspective on all three spin structures (Ha-I, FM and Ha-II). The spiral magnetism develops with a varying twist angle between neighboring spin pairs along the wave vector

direction, a subtle result due to pressure-dependent, competing exchange constants from multiple close neighbors in an anisotropic lattice [124]. By contrast, a recent non-polarized neutron diffraction study at $P = 3.8$ GPa [102] suggests spiral order along the shortest axis, b, in the *Pnma* space group. This result is surprising since for all other (V/Cr/Mn/Fe/Co/Ni)(P/As/Sb) family members (Table 4.1) [100, 101, 103–116] the spiral order exists along either of the longer axes, a or c, in the *Pnma* space group setting.
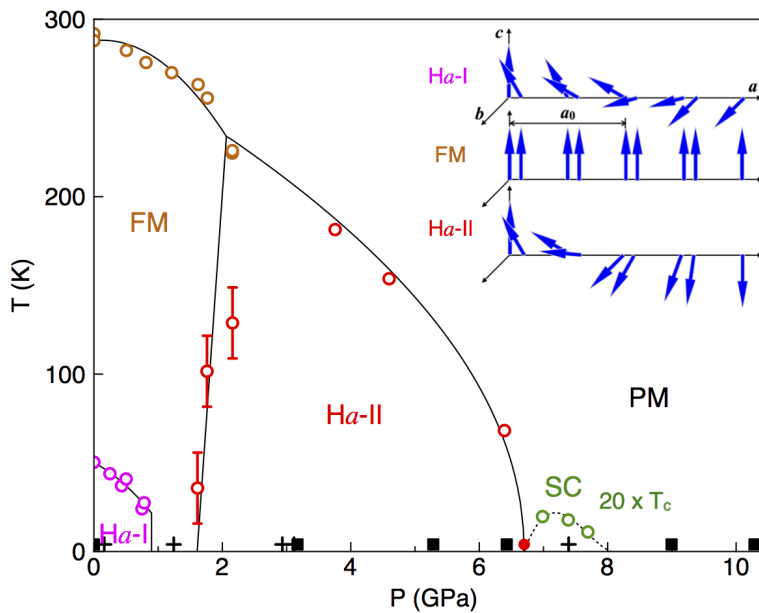
Figure 4.5: Magnetic phases of MnP. The $P - T$ phase diagram includes ferromagnetism (FM), a double-helical order (Ha-I) at low pressure [101], a new helical order (Ha-II) discovered at high pressure in the current work, superconductivity (SC) and paramagnetism (PM). Phase boundary data is adapted from [100] (open circles) with a reduction of pressure scale by a factor of 1.12 to match our X-ray measured Ha-II phase boundary at 4 K (filled circle). Also marked are (P, T) positions where the helical order was observed or proved null through magnetic scattering (filled squares) and where the lattice parameters are measured (crosses). The presence of multiple ferromagnetic phases [125] is not distinguished here for clarity. (Inset) Schematics of spin structures of three magnetic ground states, presented in a sequence of ascending pressure. The n-glide plane constraint between two helical orders in Ha-I is broken in the Ha-II phase.

The boundary of the magnetic phase is determined most accurately by the pressure evolution of the lattice. Single crystal refinement of five to six Bragg orders of MnP at each pressure indicates that the lattice structure remains in the orthorhombic phase to 10.4 GPa. Longitudinal scans of lattice orders such as (2, 0, 0), (0, 2, 1), (2,

2, 0) and (2, 2, 2), showing instrument resolution limited profiles with no noticeable peak splitting, support this conclusion. All three lattice constants evolve nonlinearly at low pressure but linearly at high pressure, with the crossover defining the critical pressure, Pc = 6.7±0.2 GPa (Fig. 4.6a and 4.6b), consistent with the range where magnetic diffraction was observed directly [100]. The lattice changes continuously under pressure to a sensitivity level of $|\Delta l|/l \sim 1 \times 10^{-3}$ (Fig. 4.6a and 4.6b). The orthorhombic structure of MnP is considered to be a distortion from the hexagonal structure of NiAs [106, 112], as the two symmetries can evolve continuously across the ratio $a/c = 1.732$. Under pressure, the orthorhombic distortion in MnP, measured by a/c, keeps increasing from 1.85 to 1.98 and moves away from the hexagonal symmetry. While helical order in both MnSi and CrAs are suppressed by pressure through a clear first-order quantum phase transition [114, 115, 126], the quantum phase transition in MnP at P_c is isostructural and could be continuous.

The lattice evolution with pressure indicates a significant magnetostriction, which is common to many $3d$ and rare-earth magnetic compounds [127, 128]. Here in MnP, magnetostriction can be extracted from Δc and Δa of the lattice and scaled to the magnetic phase boundary of either the Curie or Nêel temperatures $T_{C,N}$, as $\Delta c/c \sim \Delta a/a \sim T_{C,N}$ (Fig. 4.6), regardless of whether there is underlying ferromagnetic or antiferromagnetic order. Since the staggered magnetic moment $\langle m \rangle$ is directly related to the magnetostriction, both Δl and $\langle m \rangle$ vanish at the quantum phase transition. Beyond P_c, an energy density of 7 GPa distributed over eight valence electrons in the P $3p$ and Mn $3d$ orbitals [129] increases the electron kinetic energy t by ~15 meV per electron, comparable to the magnetic exchange constants J (2.5 - 11meV, [130]). An increasing t/J ratio reduces the ordered moment, $\langle m \rangle$, and eventually destabilizes the magnetism. While $\langle m \rangle$ drops to zero at a quantum critical point, the fate of individual local moments remains of high interest, as exemplified in heavy fermion materials [131].

Spins in MnP are deep in the local limit at ambient pressure given a Rhodes-Wohlfarth ratio of 2.2 (Fig. 4.7). The 15 meV per electron increase in kinetic energy sufficient to destabilize the magnetic order is not enough to fully delocalize the $3d$ moments, considering their 0.20 eV bandwidth [129]. Therefore, MnP is a system with local moments surviving beyond the quantum critical point, and spin fluctuations in the disordered state naturally raise special interest about magnetically-driven superconductivity.

In the disordered phase, the predominant spin fluctuation modes likely are still
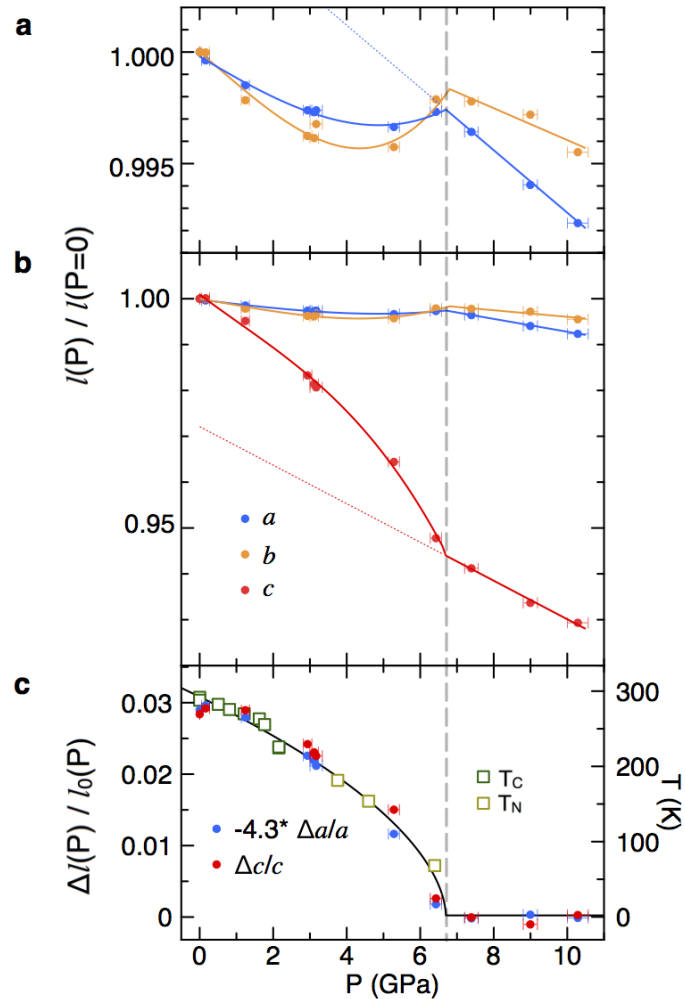
Figure 4.6: Scaled evolution of the magnetostriction and the magnetic phase boundary in MnP. (a,b) Normalized lattice evolution at $T = 4$ K under pressure, with $a(P = 0) = 5.8959$ Å, $b(P = 0) = 5.2361$ Å and $c(P = 0) = 3.1807$ Å in the *Pbnm* space group. $a(P)/a(0)$ and $b(P)/b(0)$ evolve slowly under pressure and are non-monotonic, while $c(P)/c(0)$ has a strong monotonic pressure dependence. The shapes of a, b and $c(P)$ indicate large magnetostriction. Assuming that the lattice of a non-magnetic phase should evolve linearly over this pressure range (dashed lines in a and b as $a_0(P)/a(P = 0)$ and $c_0(P)/c(P = 0)$), and that the low-pressure behavior can be modelled from extensions of the high-pressure lattice, the magnetostriction is then extracted by subtracting the estimated $a_0(P)$ and $c_0(P)$. (c) Magnetostriction, expressed as $\Delta l/l = (l(P) - l_0(P))/l_0(P)$ in both $\Delta c/c$ and $\Delta a/a$, can be scaled to magnetic phase transition temperatures T_C and T_N as a function of pressure. Δc and Δa are of different signs, indicating the anisotropic nature in both magnetic exchange interactions and the lattice's response to the magnetic order. Horizontal error bars represent the full range of pressure during a measurement.
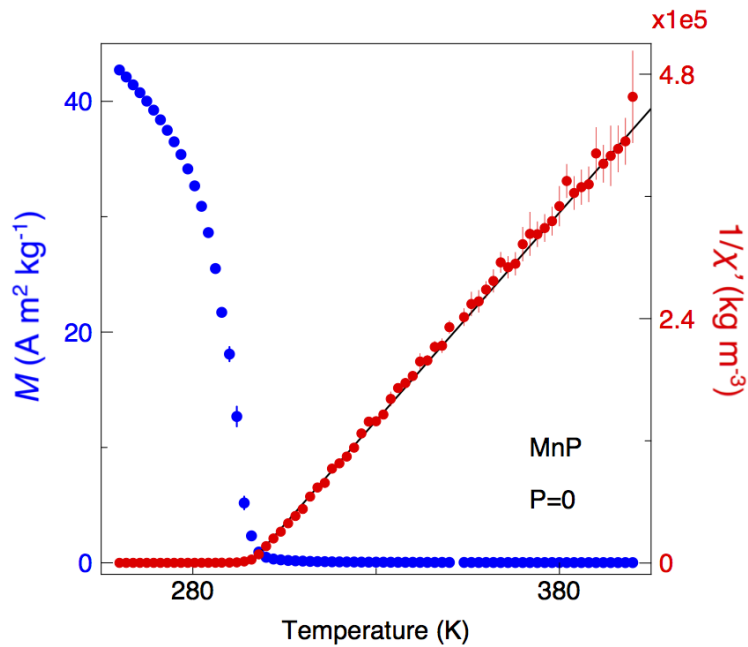
Figure 4.7: Magnetization and inverse magnetic mass susceptibility at ambient pressure. The magnetization M was measured in a SQUID based Magnetic Property Measurement System (Quantum Design) in a 100 Oe d.c. field, and plotted in SI units. Magnetic susceptibility $\chi'(T)$ was fit to the Currie–Weiss law above the ferromagnetic transition at 291 K to extract a moment of 2.79 μ_B per Mn. The measured Curie–Weiss moment is compared with the literature value of the saturated moment 1.3 μ_B per Mn [101] in the high field and low temperature limit to provide a Rhodes-Wohlfarth ratio of 2.2. Vertical error bars represent 1σ s.d. of measured magnetization.

dictated by the nearby magnetic instability [131–133]. In MnSi, helical fluctuations in the form of spiral/helix paramagnons were observed for $T > T_C$ despite a weak first order transition. Those fluctuations center at a wave vector similar in magnitude to the ordering wave vector Q, but with a random direction [133], presumably because of the short range Dzyaloshinskii-Moriya interaction in a cubic lattice symmetry. In MnP and CrAs, the lattice anisotropy likely confines wave vector directions of magnetic fluctuations. The pressure evolution of Q in CrAs [116] is constant up to $P_c \sim 0.65$ GPa [114–116, 134]. Interpreting its behavior for $P > P_c$ [134] is clouded by a strong first-order phase transition and a highly strained sample condition (lattice mismatch of several per cent) in the phase coexistence region. With no significant evolution of Q in the ordered phase under pressure (Fig. 4.2) [116], the disordered phases of MnP and CrAs should possess spin fluctuations dominated by the magnetic instability in the ordered phase, that is, spiral modes centered at $Q \sim (0.25, 0, 0)$ for

MnP and (0.36, 0, 0) for CrAs.

4.4 Discussion

Fluctuation modes in spiral magnets are of particular interest in terms of the competition between spin and lattice (phonon) fluctuations and their connection to superconducting pairing of s, p, or d character. Consider a helical fluctuation at a finite wavelength. By contrast to the usual antiferromagnet, spins of nearest neighbors along the wave vector $\boldsymbol{Q}$ direction share a large ferromagnetic projection. These ferromagnetic spin fluctuations in the low frequency limit would suppress phonon-mediated superconductivity due to on-site pairing of itinerant electrons [117], emphasizing magnetically mediated coupling channels. Furthermore, varying the pitch of the helical order provides a continuous tuning of local ferromagnetic order versus intermediate- range antiferromagnetic order, thus tilting the competition between the two types of magnetically mediated superconductivities.

The spin interaction between two itinerant electrons is an oscillating function in real space, with attractive regions at distance $(n + 1/2)\lambda$ (where n is an integer). The strongest interaction happens at a half pitch length $\lambda/2$ of the fluctuating spiral modes (Fig. 4.8a), which is about 12 Å in MnP. This is similar to the antiferromagnetic fluctuation-mediated interaction in the rare earth cuprates and the heavy fermion compounds [30, 136]. There is a relatively long interaction length between itinerant charge carriers as compared with both the on-site interaction of the phonon-mediated type [136] and the nearest-neighbor resonant valence bond type for underdoped cuprates [137]. On the other hand, the coherence lengths of Cooper pairs are typically much longer than interaction lengths in both phonon- and magnetically-mediated superconductors [30, 136] and for MnP, the superconducting coherence length extends over 300 Å [100]. This coherence length is necessarily smaller than the mean free path of itinerant electrons, thereby allowing the electron pair overlap to maintain phase coherence. The MnP samples we used have a residual resistance ratio of ~1000 at ambient pressure [100], close to the clean limit. The issue of pairing symmetry is more tenuous, but the model of helical magnets allows certain predictions. The interaction of paring itinerant electrons at a distance $r = (n+1/2)\lambda$ along the wave vector $\boldsymbol{Q}$ direction of helical spin fluctuations (Fig. 4.8a) mandates a preferred axial direction and suggests that the superconductivity might be of the singlet d_{z^2} type, especially in light of the low-symmetry lattice structures of MnP and CrAs.
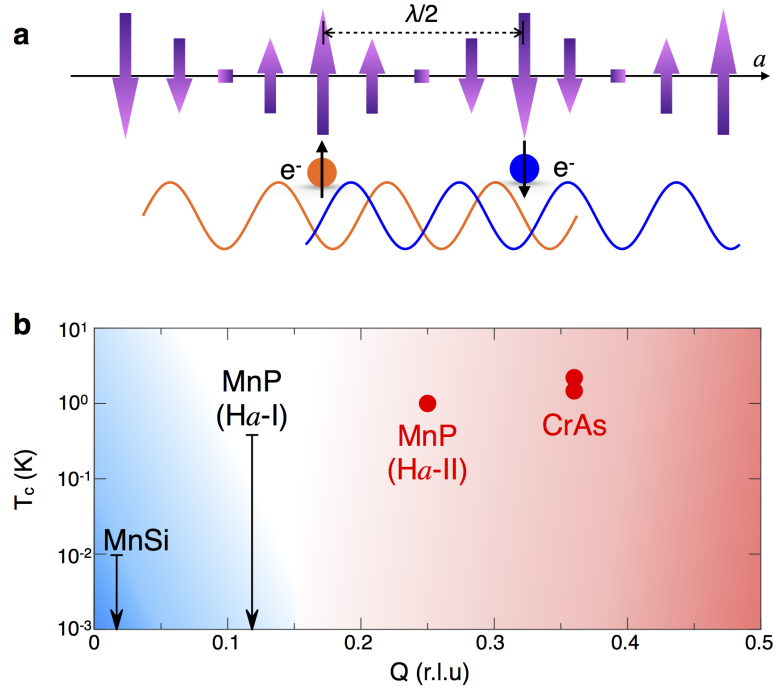
Figure 4.8: Variable helical pitch length as a tuning method for magnetically me-
diated superconductivity. (a) Schematic of a superconducting electron pair coupled
through helical spin order in a projected planar view. The two sites of itinerant
electron coupling are separated along the helical order by a half wavelength $\lambda/2$,
suggesting the possibility of singlet d_{z^2}-wave pairing. This scenario competes with
superconductivity of a ferromagnetic type, while the nearly parallel local spin con-
figuration always suppresses phonon-mediated superconductivity at a single site
[117]. (b) Superconducting transition temperature T_c plotted as a function of he-
lical wave vector Q in selected $3d$ intermetallic compounds. Data for MnSi [126,
133], MnP [100, 101] and CrAs [114–116] are collected from either the literature
or current work. Red solid circles represent observed superconducting transitions,
which only exist in pressure-induced disordered phases beyond the helical order,
and are likely antiferromagnetically mediated. The horizontal bars of the downward
arrows represent the lower bounds of null searches for superconductivity. Ferro-
magnetically mediated superconductivity is expected to be at a lower temperature
than its antiferromagnetic counterpart [30, 135]. The pitch of the helical order
represents a potential tuning method between ferromagnetically (blue region) and
antiferromagnetically (red region) mediated superconductivity.

While spiral fluctuations suppress phonon-mediated superconductivity and enhance
the coupling channels for the magnetic interactions, helical fluctuations of differ-
ent pitches provide the means to switch from ferromagnetic to antiferromagnetic
character. With increasing spiral wavelength, the interaction strength of the antifer-
romagnetic coupling is reduced over an elongated r [30]. Moreover, an increased

spiral wavelength reduces the turning angle between neighboring spins and thereby heightens the local ferromagnetic spin density. By varying the pitch, it is possible to tune both the ferromagnetic and antiferromagnetic spin fluctuations. Our focus on local moment helical order complements itinerant models of continuous tuning by band filling from ferromagnetic to antiferromagnetic order with a concomitant switch between magnetically mediated superconductivities of different symmetries [135]. Through the comparison of the cuprates and Sr_2RuO_4, it appears that ferromagnetically mediated superconductivity typically has an orders of magnitude lower transition temperature than its antiferromagnetic analogue of the same dimensionality [135].

The dimensionality of the spin fluctuations is another interesting issue. The helical order in $3d$ compounds can be compared with incommensurate antiferromagnetic order in heavy fermion materials like $CeCu_{6-x}Au_x$ [131], where spin fluctuations with two-dimensional character were observed around the ordering wave vector Q [132]. Even though the effective low dimensionality enhances the spin fluctuations, the extremely low magnetic coupling strength in $CeCu_{6-x}Au_x$ [131] suppresses the possible magnetically mediated superconductivity below experimental sensitivity. Spin fluctuations in MnP are likely three-dimensional (3D) judging from the $T^{3/2}$ dependence of the resistivity [100], but they are matched with a large magnetic coupling strength [130] and bandwidth [129], so the superconducting transition temperature, T_c, could still be measurable even at a level of $T_N/1,000$. For 3D helical magnets such as MnP and CrAs with T_c = 1 - 2 K (Fig. 4.8b), the corresponding ferromagnetic type could be below the lowest range of temperatures measured to date.

Although experimental evidence is still limited, the effects of a variable spiral pitch are suggestive. We illustrate the trends in Fig. 4.8b for the series MnSi, MnP and CrAs as a function of their different magnetic wave vectors. With a small spiral wave vector of (0.017, 0.017, 0.017) [133], MnSi does not superconduct under pressure down to at least 10 mK [126], although the lack of an inversion center could complicate the symmetry properties of a superconducting state. For MnP at low pressure, the helical order with a wave vector of $0.117\ r.l.u.$ [101] was replaced by ferromagnetic order at P ∼ 1 GPa, and no superconductivity was observed down to 350 mK [100]. On the other hand, both MnP at high pressure ($0.25\ r.l.u.$) and CrAs ($0.36\ r.l.u.$) have relatively large wave vectors (short pitches) and demonstrate superconducting ground states once the helical order is suppressed by pressure [115,

Table 4.1: Compounds in the (V/Cr/Mn/Fe/Co/Ni)(P/As/Sb) family with spiral antiferromagnetic order, organized by Q-vector from 0.07 to 0.40. Marked as well is the direction of the helical order along either the *a*- or *c*-axes in the *Pnma* space group setting.

Compounds	T_N(K)	Q (*r.l.u.*)	Helical order	Reference
$Mn_{0.65}Cr_{0.35}As$	195	0.071	*a*	[110]
$Mn_{0.7}V_{0.3}As$	142	0.08	*a*	[105]
$Mn_{0.75}Cr_{0.3}As$	202	0.088	*a*	[110]
$Mn_{0.75}Cr_{0.25}As$	205	0.097	*a*	[110]
$MnAs_{0.925}P_{0.075}$	232	0.10	*a*	[108]
$Mn_{0.95}Co_{0.05}P$	53	0.101	*c*	[111]
$Mn_{0.9}Co_{0.1}P$	49	0.107	*c*	[111]
$Mn_{0.95}V_{0.05}P$	107	0.109	*c*	[111]
$Mn_{0.8}Co_{0.2}P$	70	0.111	*c*	[111]
$Mn_{0.9}Cr_{0.1}P$	50	0.112	*c*	[111]
$Mn_{0.95}Fe_{0.05}P$	62	0.113	*c*	[111]
$Mn_{0.95}Cr_{0.05}P$	53	0.116	*c*	[111]
$Mn_{0.9}V_{0.1}As$	206	0.116	*a*	[105]
MnP (low pressure)	50	0.117	*c*	[101]
$Mn_{0.8}Cr_{0.2}As$	208	0.120	*a*	[110]
$Mn_{0.95}V_{0.05}As$	200	0.128	*a*	[105]
$Mn_{0.9}Cr_{0.1}As$	210	0.133	*a*	[110]
$Mn_{0.95}Fe_{0.05}As$	211	0.142	*a*	[107]
$Mn_{0.9}Fe_{0.1}P$	172	0.145	*c*	[111]
$Mn_{0.9}V_{0.1}P$	152	0.151	*c*	[111]
$Mn_{0.95}Ni_{0.05}As$	202	0.155	*a*	[109]
$Mn_{0.95}Co_{0.05}As$	196	0.166	*a*	[106]
$Mn_{0.9}Co_{0.1}As$	174	0.184	*a*	[106]
$Mn_{0.85}V_{0.15}P$	141	0.189	*c*	[111]
$Mn_{0.8}V_{0.2}P$	113	0.194	*c*	[111]
FeP	125	0.20	*c*	[103]
$Mn_{0.85}Co_{0.15}As$	152	0.209	*a*	[106]
$Mn_{0.8}Fe_{0.2}P$	142	0.210	*c*	[111]
MnP (high pressure)		0.250	*c*	current work
$Mn_{0.6}Cr_{0.4}As$	232	0.252	*c*	[110]
$Mn_{0.72}Fe_{0.28}P$	173	0.258	*c*	[111]
CrAs	265	0.356	*c*	[116]
$Cr_{0.98}Ni_{0.02}As$	202	0.357	*c*	[109]
FeAs	70	0.395	*c*	[113]
$CrAs_{0.86}Sb_{0.14}$	340	0.40	*c*	[104]
$CrAs_{0.72}Sb_{0.28}$	340	0.40	*c*	[104]
$CrAs_{0.66}Sb_{0.34}$	310	0.40	*c*	[104]
$CrAs_{0.5}Sb_{0.5}$	175	0.40	*c*	[104]

116].

We list in Table 4.1 38 different intermetallic compounds with magnetic pitch varying nearly continuously from 0.07 to 0.40 $r.l.u$. Most of them have not been examined under pressure, neither to map the evolution of their magnetism nor to search for superconductivity. With such studies, the $3d$ helical magnets of the (V/Cr/Mn/Fe/Co/Ni)(P/As/Sb) family [100, 101, 103–116] present manifest opportunities to further our understanding of the linkage between magnetism and unconventional superconductivity.

Chapter 5

QUANTUM PHASE TRANSITIONS IN $Cd_2Os_2O_7$

Correlated electron systems are characterized by competing energy scales. These include the on-site Coulomb (Hubbard) interaction U, the electron kinetic energy represented by the hopping integral t, the crystal field strength Δ, and the spin-orbit coupling constant λ. In decades-long explorations of $3d$ electron systems, such as cuprates and vanadium oxides, λ is negligible; thus the competition among U, t, and Δ determines the general physical properties. When it comes to $5d$ electrons, $\lambda \sim Z^4$ is significantly enhanced and plays a major role, while U/t also becomes smaller due to the more extended d band. For example, Sr_2IrO_4 inherited the Mott physics from $3d$ transition-metal compounds with an additional contribution from λ, becoming a spin-orbit Mott insulator [138]. As a consequence, $5d$ electron systems provide a new testbed to study correlation effects in a regime where all energy scales are similar: $U \sim t \sim \lambda \sim \Delta$.

Orthogonal to the energy perspective, spatial and/or geometrical properties could play an equally important role in shaping the physics of correlated electron systems. First, crystal structures with particular symmetry properties could fundamentally determine the parity of ground states. For instance, superconductivity in lattices with and without inversion symmetry should have distinct parity and pairing properties [139]. Second, lattice geometry can introduce magnetic frustration or induce long-range magnetic order of certain spin configurations, such as the cases of Kagomé [140], Shastry-Sutherland [141], and pyrochlore lattices [142]. Finally, for phase transitions in which the crystal structure is less distorted, a continuous transition is preferred, which is relevant to this chapter, and a theme that connects the topics in this thesis, especially this chapter.

All combined, $5d$ electron systems with special symmetry properties potentially can be tuned through continuous quantum phase transitions where various interactions strongly compete, thus involving entangled fluctuation modes. As we discussed in Chapter 1, this type of strongly-coupled QPT could exhibit nontrivial quantum critical phenomena beyond mean-field theory [16, 17]. Recently, pyrochlore-structured $5d$ transition-metal oxides such as $A_2Ir_2O_7$ (A = Y, La, Eu, Sm, and Nd) and $Cd_2Os_2O_7$, with a concurrent metal-insulator and paramagnetic-antiferromagnetic

transition, were proposed as candidates for studying this type of quantum criticality [17]. Here, we directly track the breakdown of all-in-all-out antiferromagnetic order in the low temperature limit at 35.8 GPa in $Cd_2Os_2O_7$, employing a newly-developed, high-pressure, resonant x-ray magnetic scattering technique. Both x-ray diffraction and Raman spectroscopy support a scenario of a continuous quantum phase transition. Concurrent with the antiferromagnetic QPT, the lattice undergoes inversion symmetry breaking, corresponding to the softening of a breathing mode. With the high pressure phase line manifesting a curvature strongly deviating from the mean-field prediction, we argue that the critical region, which connects three phases of different time-reversal and inversion symmetry properties, is of a strongly-coupled nature involving the spin, charge and structural degrees of freedom.

5.1 Introduction

An all-in-all-out (AIAO) spin arrangement on corner-sharing tetrahedra (Fig. 5.1a) has spins pointing either all towards or all against the center of each tetrahedron (Fig. 5.1b), which is an unusual form of magnetism that preserves the underlying cubic lattice symmetry. This spin order is often termed as a $Q = 0$ state in order to reflect the preservation of lattice symmetry and unit cell size. However, this should be distinguished from a $Q = 0$ type of ferromagnetic order where the wave length is infinitely long. AIAO spin order has been observed in pyrochlore systems such as FeF_3 [143], $Nd_2Zr_2O_7$ [144], $A_2Ir_2O_7$ (A = Sm, Eu and Nd) [64, 145, 146], and $Cd_2Os_2O_7$ [63] and suggested for additional $A_2Ir_2O_7$ systems with A = Y, Eu, Gd, Tb, Dy, Ho, Yb, and Lu [147].

The formation of such a magnetic order in $A_2Ir_2O_7$ (A = Y, La, Eu, Sm, and Nd) and $Cd_2Os_2O_7$ is also concomitant with a metal-insulator transition without any structural discontinuity at $T_{N, MIT}$ [148–150]. The continuous nature of this thermal transition is directly reflected by the slow rise of the ordered moment size as well as the electrical resistivity at the transition temperature [63, 64, 145, 146, 148–150]. The concurrent spin and quasiparticle fluctuations at the transition, combined with the general strong spin-orbit coupling in $5d$ electrons, makes the quantum version of this AIAO/MIT phase transition intriguing for establishing a model system for non-mean-field type QPTs. In $Ln_2Ir_2O_7$ (Ln = Nd, Sm, Eu, Gd, Tb, Dy, and Ho), T_{MIT} was suppressed to zero by field [151, 152], pressure [151, 153, 154], and chemical tuning of Ln [150, 151], while signatures of non-Fermi liquid behavior have been proposed both experimentally [154, 155] and theoretically [156, 157] in the quantum critical region. However, for the AIAO type of antiferromagnetic QPT, there is still
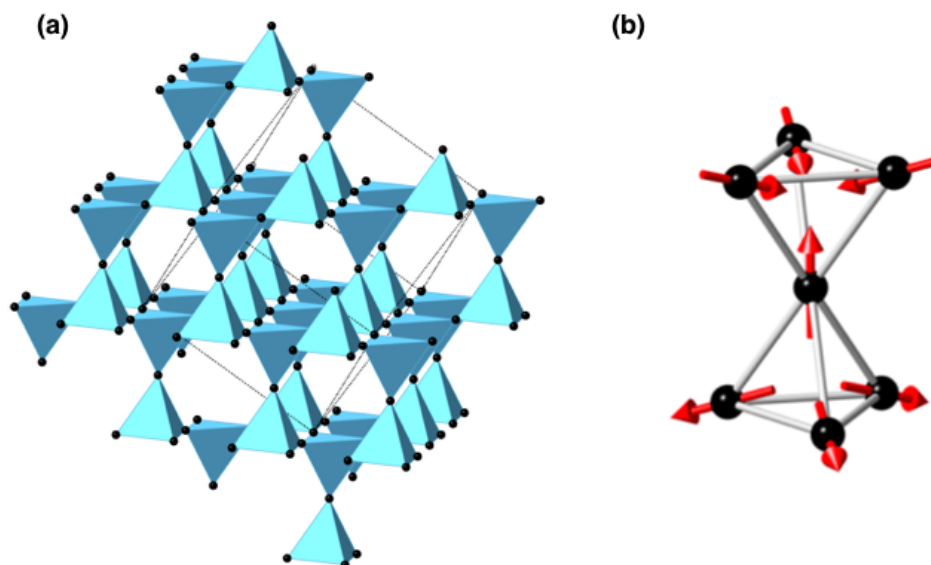
Figure 5.1: Pyrochlore lattice structure and spin configurations in the all-in-all-out magnetic order. (a) A schematic of $Cd_2Os_2O_7$, showing only Os sites to highlight the pyrochlore spin structure, with layers of Kagome lattice and triangular lattice stacked alternatively along the <1,1,1> direction. (b) Local spin arrangement at two neighboring tetrahedra, with spin moments pointing radially to the center in one tetrahedron (all-in), and pointing towards the outside in the other (all-out).

lacking a direct measurement to prove its existence and the underlying symmetry evolution. Thus it is crucial to develop a microscopic probe of the intertwined electron, spin, orbital, and lattice degrees of freedom at the quantum critical point.

A direct measurement of the AIAO order could be performed by either neutron or x-ray magnetic scattering. For $Ln_2Ir_2O_7$ and $Cd_2Os_2O_7$, neutron scattering would encounter strong intrinsic absorption by either Cd or Ir, along with the difficulties of both the high cost of Ir and Os materials and growing large single crystals from a high temperature solution. X-ray magnetic diffraction provides an alternative and potentially more accessible venue for experimental exploration [63, 64]. In addition, as discussed in Chapter 2, a focused x-ray beam is of compatible dimensions with a high pressure sample. For commensurate magnetic order such as AIAO with a wave vector coincident to that of the lattice, magnetic diffraction at an x-ray resonant edge combined with polarization analysis is necessary to verify the magnetic nature. With all these factors considered, resonant x-ray magnetic diffraction is the most suitable technique under high pressure to directly probe QPTs of AIAO order. The experimental methods of resonant x-ray magnetic scattering have been discussed in detail in Chapter 2.

Using the combined experimental tools of resonant x-ray magnetic diffraction and optical Raman scattering, we have explored the potential quantum critical state in a system with antiferromagnetic AIAO order. We select $Cd_2Os_2O_7$ as our model system over $Ln_2Ir_2O_7$, mainly to avoid the site-disorder issue from 3+/4+ valence states of Ln and Ir, in comparison with the 2+/5+ valence states of Cd and Os [142]. This stoichiometry and site disorder issue renders a large uncertainty in determining the transport nature of the paramagnetic state [147, 158]. In addition, this choice also avoids the potential complication from an extra set of Lanthanide magnetic moments on the A site pyrochlore (excepting Eu). At ambient pressure, $Cd_2Os_2O_7$ undergoes a metal-insulator transition at T_{MIT} = 227 K concurrent with the formation of AIAO magnetic order. The transition temperature can be suppressed by pressure with an initial rate of ~4 K/GPa, measured through electrical transport to 2 GPa [148]. The AIAO magnetic order was directly illustrated by resonant x-ray magnetic diffraction at the Os L_3 edge [63], and the lattice symmetry was characterized in detail by optical Raman scattering [63].

We have successfully performed high-pressure single-crystal resonant x-ray diffraction experiments across the quantum phase boundary of AIAO spin order in $Cd_2Os_2O_7$ at P_c = 35.8 GPa, observing neither a discontinuity in the lattice constant nor an abrupt change in the electronic configuration of valence orbitals. Concomitant to the recovery of time-reversal symmetry in the magnetically disordered state, the crystal lattice experiences a spontaneous inversion symmetry breaking with a continuous space group change from $F d \bar{3} m$ to $F \bar{4} 3 m$. Broad phase space exploration by optical Raman also confirmed the presence of the $F d \bar{3} m$ lattice space group from 10 - 300 K, and 0 - 29 GPa. All these results combine to manifest a coexistence of spin fluctuations, lattice breathing modes, and quasiparticle excitations in the quantum critical region, and a potential interplay between them surrounding the confluence point of quantum phase transitions of spin and lattice degrees of freedom. Those components naturally point to strongly-coupled quantum criticality in this three-dimensional antiferromagnet.

5.2 Spin and orbital resonance

The antiferromagnetic order introduces a different set of selection rules for diffraction in comparison to that of the lattice. With a commensurate wave vector $Q = 0$ in the AIAO phase of $Cd_2Os_2O_7$, magnetic diffraction peaks could be probed at forbidden lattice orders such as (2, 0, 0) and (6, 0, 0) [63]. However, diffraction signals at these reciprocal space positions still could contain contributions from two other scat-
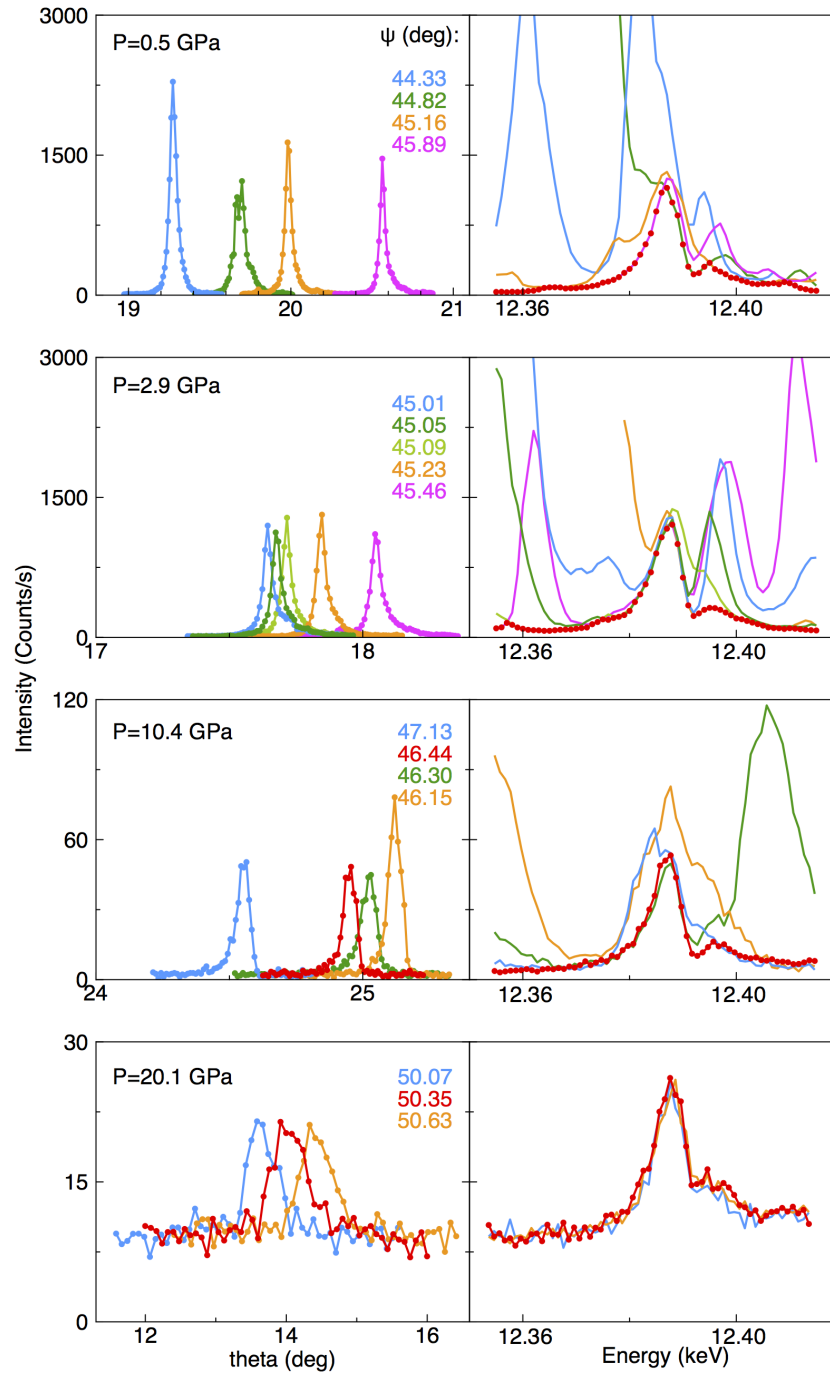
Figure 5.2: Raw scans of resonant magnetic diffraction at low pressures. (Left) Mosaic scans of $(6, 0, 0)$ order at different azimuthal angles with the values specified in the panel. (Right) Energy resonance profiles under various azimuthal conditions. Intensity is expressed in Counts/s for $I = 100$ mA synchrotron storage current. While multiple scattering is present, the minimum trace of these curves manifests the energy resonance profile of the magnetic diffraction.

tering mechanisms, namely, multiple scattering and anisotropic tensor susceptibility (ATS) scattering. The latter is typically understood as a type of orbital ordering in the system [65–67] (Chapter 2). Multiple scattering does not possess a resonance profile, and could be easily detected and eventually separated. On the other hand, ATS scattering potentially could lead to the same resonance profile as its magnetic counterpart (Figs. 5.2, 5.3, 5.4). Unlike the scattering matrix of regular Bragg diffraction that only has the diagonal components and preserves the polarization of the incident beam, both magnetic and ATS scattering matrices have off-diagonal components to switch the polarization of the scattered x-rays [60, 67] (Chapter 2). Scattering matrix elements from these two processes (ATS and magnetism) can be separated by using different incident and scattered x-ray polarizations, together with the azimuthal conditions of the diffraction order, which makes resonant scattering a type of spectroscopy within diffraction.

At the Os L_2 edge, these two types of resonances share the same virtual transition probability from the core $2p_{\frac{1}{2}}$ orbit to empty orbitals of the t_{2g} band as the intermediate state, and they exhibit a similar energy dependence in the resonance profile (Figs. 5.2, 5.3, 5.4). In the $\pi - \sigma$ channel of the horizontal scattering geometry, the ATS resonance at azimuthal angle $\psi \sim \pm 45°$ (relative to the <0 0 1> order) becomes zero for both (2, 0, 0) and (6, 0, 0) orders of the $Fd\bar{3}m$ space group [63], while that of the (4, 2, 0) order is finite. In addition, the magnetic scattering intensity in $Cd_2Os_2O_7$ is about one to two orders of magnitude smaller than typical ATS scattering. Thus, in the $\pi - \sigma$ channel, the intensity of the (4, 2, 0) order mainly represents the ATS signal, while that of the (6, 0, 0) order represents the pure magnetic signal. In the $\pi - \pi'$ channel, both magnetic and ATS scattering are weak, and intensities from forbidden orders (6, 0, 0) and (4, 2, 0) would be sensitive to the regular Bragg diffraction of the lattice, and reflect the change of the space group.

The low intensity signal of the magnetic resonance can be contaminated by multiple scattering that shows up in both the mosaic curves and the energy spectra (Figs. 5.2, 5.3), and is sensitive to slight changes in the sample azimuthal angle. Therefore, several scans with slightly different azimuthal conditions around $45°$ were always taken to distinguish the true magnetic signal as the minimum shape of all energy spectra (Figs. 5.2, 5.3). It was possible to find a position where a clean energy resonance signal exists without additional multiple scattering, especially for samples with a broad mosaic at high pressure. In $Cd_2Os_2O_7$, magnetic resonance has been observed at the (6, 0, 0) order on seven samples at 4.0 ± 0.5 K, and in the pressure
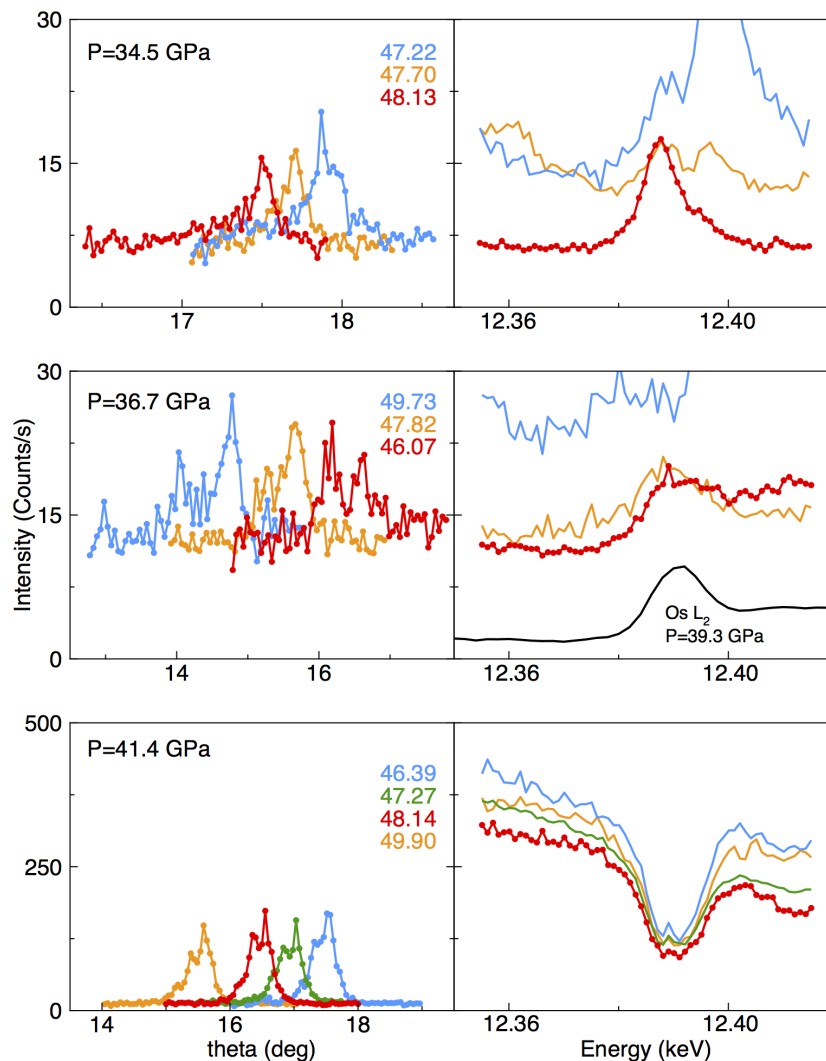
Figure 5.3: Raw scans of resonant magnetic diffraction close to and beyond the critical point. Left and right panel assignments are the same as Fig. 5.2. At the phase boundary (36.7 GPa), the magnetic resonance has disappeared, and the energy dependence is that of the Os L_2 fluorescence background. Beyond that pressure, lattice distortion allows charge diffraction at the (6, 0, 0) order, as the resonance profile reflects the charge nature of the energy dependence.

range between ambient and 34.5 GPa.

We believe that the magnetic order is fully suppressed by 36.7 GPa (Fig. 5.3), judging by the differently-shaped energy spectrum profile; no clear resonance at 12.387 keV was observed. Instead, the minimum profile of the energy scan exhibits a similar shape with the L_2 fluorescence background across the absorption edge (Fig. 5.3). This behavior was verified on another sample at a slightly higher pressure of
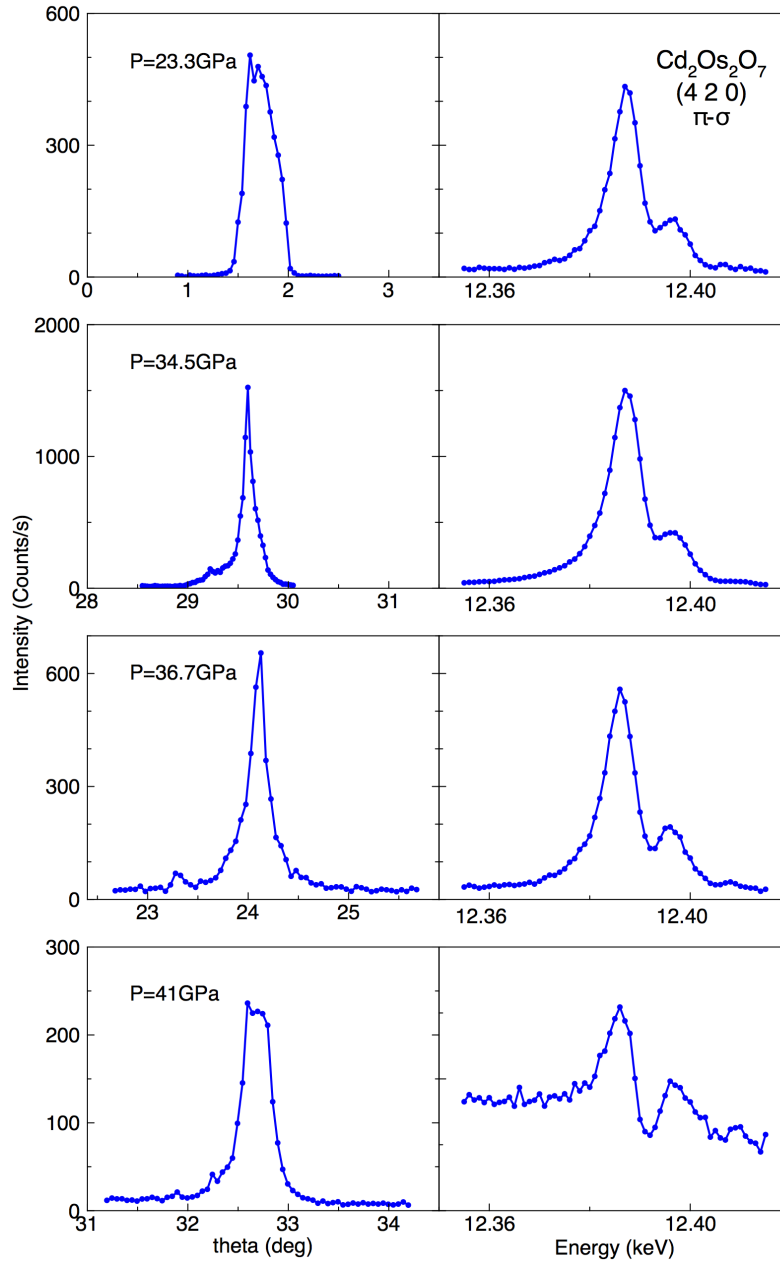
Figure 5.4: Raw scans of the ATS resonance at (4, 2, 0). For simplicity, we only display one mosaic profile (left) and one resonance profile (right). The ATS signal is 10 - 100 times stronger than the magnetic diffraction intensity. Hence the contamination from multiple scattering is small. The resonance extends beyond the magnetic phase boundary at P_c = 35.8 GPa, although the resonance profile at 41 GPa shows a summation of ATS resonance in the channel and a projection of 2.5% of the diffraction intensity in the channel due to the fact that the graphite analyzer crystal was placed at an angle of about 5 degrees off 90 degrees.

38.6 GPa with an increased overall intensity. At 41 GPa, the diffraction intensity at (6, 0, 0) was significantly enhanced by 1.5 orders of magnitude. Meanwhile, the energy scan manifests a typical profile of those allowed Bragg peaks, which has an inverse shape of the L_2 edge absorption spectrum (Fig. 5.3). This indicates that the (6, 0, 0) order becomes non-forbidden at high pressure due to a variation in the lattice symmetry. The lattice symmetry assignments will be discussed in the following section.

Resonance scattering at the (4, 2, 0) order, with an azimuthal angle about 50° in our sample geometry, manifests a significant ATS diffraction signal in the $\pi - \sigma$ channel (Fig. 5.4). An ambient pressure characterization indicates that the ATS diffraction at (4, 2, 0) is about one order of magnitude stronger than the magnetic resonance, with little temperature dependence from 4 K to 300 K. Therefore, measurements at the (4, 2, 0) order naturally are less affected by multiple scattering and show consistent behavior in both rocking and energy scan curves at various azimuthal angles. Unlike magnetic resonance, which diminishes at high pressure, ATS resonance has been observed all the way up to 41 GPa (Fig. 5.4). The resonance profiles remain unchanged in the whole pressure–temperature phase space within an energy resolution of approximately 1.7 eV, suggesting an essentially constant t_{2g} band, in which the empty states provide pathways to virtual transitions in the resonant process. At 41 GPa, the ATS resonance signal is still distinguishable, as the energy spectrum is a superposition of both the ATS resonance and that of normal lattice diffraction in both the $\pi - \pi'$ and $\sigma - \sigma$ (~1.3% leakage) channels (Fig. 5.4).

5.3 Lattice structure and symmetry

At ambient pressure, Cd2Os2O7 belongs to the $Fd\bar{3}m$ space group (No. 227) of cubic structure through the entire temperature range. No discontinuity of the lattice constant has been discovered through the magnetic transition at T_N = 227 K [63, 148]. At 4 K, longitudinal scans at diffraction orders (1, 1, 1) and (2, 2, 0) (Fig. 5.5) both remain in a single peak profile over the whole pressure range up to 41 GPa, indicating that the cubic structure is preserved throughout. As a consequence of both the fragmented mosaic structure of the single crystal and pressure inhomogeneity across the sample, the HWHM of the longitudinal line shape at (0, 2, 2) (Fig. 5.5) has evolved from 0.005° at 1.4 GPa to 0.016° at 37.3 GPa, corresponding to a correlation length changing from 2000 Å to 600 Å. Starting with a = 10.1614 Å at ambient pressure, the lattice constant shrunk by ~5% at 41 GPa without discontinuity within a sensitivity of $\Delta a/a \sim 10^{-3}$ (Fig. 5.5). While the $Fd\bar{3}m$ space group is uniquely
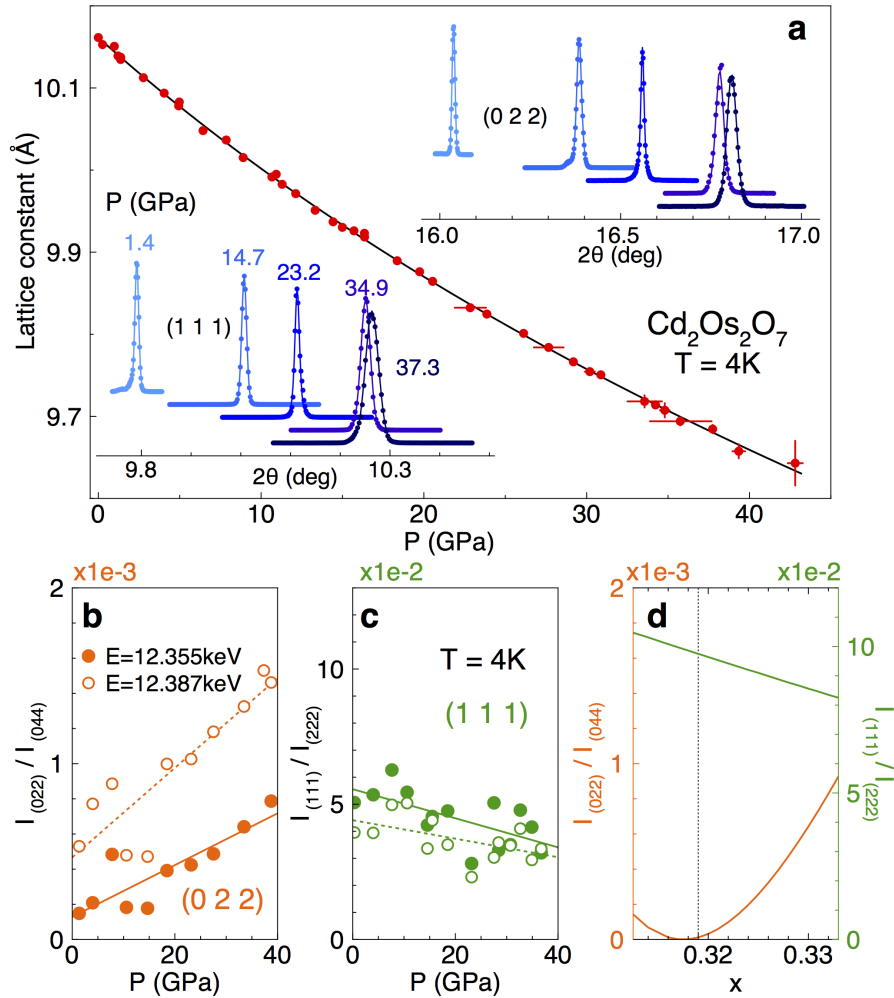
Figure 5.5: Lattice evolution under pressure. (a) Pressure evolution of the lattice constant was fit to a two-parameter Birch equation of state with $B = 190.4 \pm 3.6$ GPa, and $B' = 4.2 \pm 0.2$. (insets) Longitudinal ($\theta/2\theta$) scans of (1, 1, 1) and (0, 2, 2) orders measured at various pressures using 12.387 keV x-rays verify the cubic symmetry. (b-c) Pressure evolution of integrated diffraction intensities of (0, 2, 2) and (1, 1, 1) orders, normalized by (0, 4, 4) and (2, 2, 2) orders, respectively. The measurement was performed under either resonant ($E = 12.387$ keV) or off-resonant ($E = 12.355$ keV) conditions. These two orders are sensitive to O $48f$ sites in the unit cell, and develop in opposite fashion up to 40 GPa. (d) Simulated (0, 2, 2) and (1, 1, 1) intensities as a function of x. The overall percentage changes of (0, 2, 2) and (1, 1, 1) give an x increasing from 0.319 at $P = 0$ [148] to approximately 0.325 at P_c.

determined by the unit cell's lattice constant and one free coordinate x for oxygen position on $48f$ sites that characterizes the trigonal distortion of the Os-O$_6$ cluster [148, 159], diffraction intensities at (1, 1, 1) and (0, 2, 2) show a continuous evolution

through the quantum phase transition, with x increasing by a small amount from 0.319 at $P=0$ [148] to ~0.325 at P_c (Fig. 5.5b-c).

Although the cubic symmetry was preserved and the lattice constant evolves continuously under pressure, a change in the space group which characterizes the symmetry properties of all sites is still allowed. Specifically, the $Fd\bar{3}m$ space group could have a cascade of continuous symmetry evolution to cubic structured $F\bar{4}3m$, $F4_132$ and $Fd\bar{3}$ space groups and other tetragonal and trigonal space groups, as exemplified in the closely-related, non-magnetic superconductor $Cd_2Re_2O_7$ [160–162]. Such symmetry changes could be observed by the violation of certain forbidden selection rules when lattice symmetry is lowered [160].

Lattice symmetry at low temperature

As we pointed out earlier, both the ATS and magnetic resonant scattering matrices have very small $\pi - \pi'$ components in $Cd_2Os_2O_7$, allowing a sensitive probe of lattice symmetry changes. While the $\pi - \pi'$ intensity at both (6, 0, 0) and (4, 2, 0) orders remains consistently low below 36 GPa, it starts increasing when the magnetic diffraction intensity is suppressed (Fig. 5.6). The energy scans show an inverse shape of the absorption spectrum without any resonance signature, indicating that the intensity is not coming from a different ATS behavior. Instead, it comes from selection rules of a different symmetry group at high pressure, which make (6, 0, 0) and (4, 2, 0) no longer forbidden. Within a cubic structure (Fig. 5.5), the low-pressure $Fd\bar{3}m$ group could continuously evolve to $F\bar{4}3m$, $F4_132$ and $Fd\bar{3}$ groups. However, selection rules for $F4_132$ ($h = 4n$ for (h, 0, 0) orders) would not allow diffraction intensity at (6, 0, 0), while those of the $Fd\bar{3}$ group ($h = 4n$ for (h, 0, 0) and $k + l = 4n$ (k, l = 2n) for (0, k, l) orders) would allow neither (6, 0, 0) nor (4, 2, 0). Therefore, $F\bar{4}3m$, allowing diffraction at both orders, is the only possible choice.

A similar symmetry group change has been reported in $Cd_2Re_2O_7$ upon cooling [160], with a lower symmetry from breaking lattice inversion symmetry, which is exactly why (6, 0, 0) and (4, 2, 0) orders gain diffraction intensity. In the $Fd\bar{3}m$ group, the Cd $16d$ site and the Os $16c$ site both manifest .$\bar{3}m$ local symmetry. Therefore, the Cd- and Os-tetrahedra are identical (Fig. 5.1). Both atoms bear no free parameters in their coordinates and the geometric diffraction factors for (6, 0, 0) and (4, 2, 0) simply sum up to be zero. In the $F\bar{4}3m$ group, however, both Cd and Os occupy $16e$ sites, coordinated by (x, x, x) in position with x being a free parameter
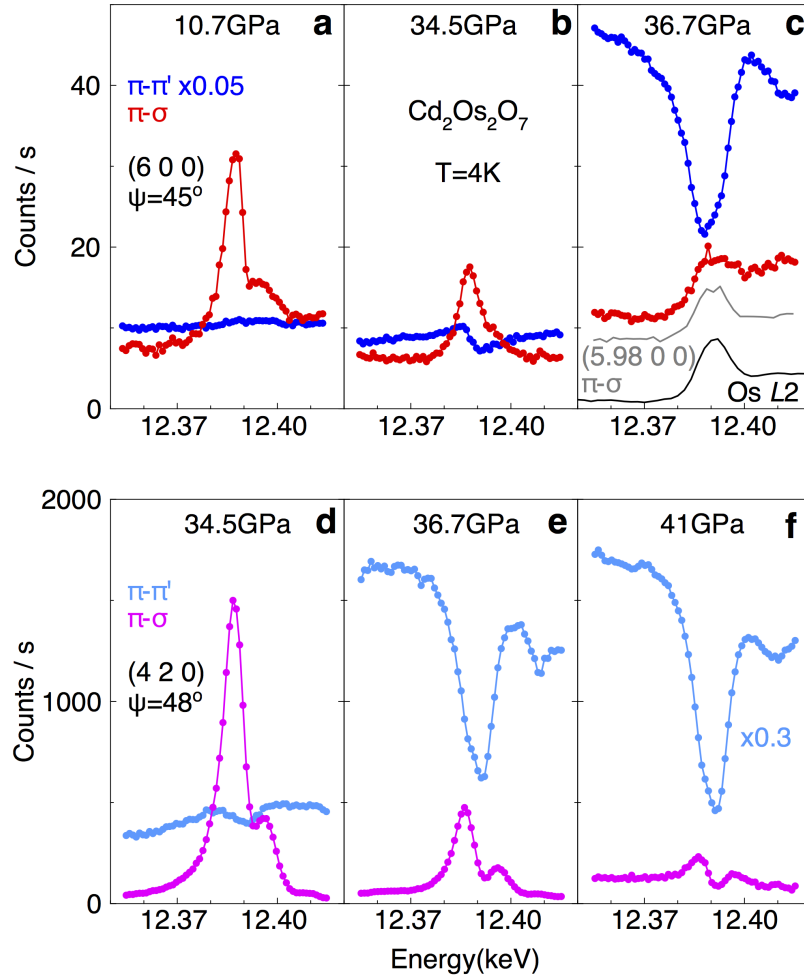
Figure 5.6: Polarization-sensitive resonant diffraction data under pressure. Raw energy scan profiles at both (a-c) (6, 0, 0) and (d-f) (4, 2, 0) orders from two separate polarization channels ($\pi - \sigma$ in red/pink and $\pi - \pi$' in navy/aqua). While magnetic resonance in the $\pi - \sigma$ channel at (6, 0, 0) has been suppressed (Fig. 5.4, text), the $\pi - \pi$' charge diffraction intensities rise dramatically for both (6, 0, 0) and (4, 2, 0) orders, with a small leakage into the $\pi - \sigma$ channel becoming apparent through the polarization analyzer.

characterizing the perturbation around 1/8 (Os) and 5/8 (Cd), respectively [148]. Accordingly, the inversion symmetry is removed from $.\bar{3}m$ to $.3m$ local symmetry. The newly found freedom allows Cd and Os atoms to slide along local <1 1 1> direction, yielding different sizes of adjacent tetrahedra in the Cd and Os networks. The diffraction intensities from both (6, 0, 0) and (4, 2, 0) are proportional to $|f_{Os}\Delta_{Os} + f_{Cd}\Delta_{Cd}|^2$, where f_{Os} and f_{Cd} are the atomic factors of Os and Cd atoms, respectively, and Δ_{Os} and Δ_{Cd} represent the perturbations from equal-sized adjacent tetrahedra. From the perspective of inversion symmetry breaking, this corresponds

to a lattice breathing mode, which has been discovered in many pyrochlore systems such as KOs_2O_6 [163], $LiGa_{1-x}In_xCr_4O_8$ [164–166], $Ba_3Yb_2Zn_5O_{11}$ [167], etc., and has direct implications on the nature of the magnetism [168–170].

Lattice symmetry in broader $P - T$ phase space

Our optical Raman spectroscopy provides an efficient survey of symmetry conditions over the broad pressure-temperature phase space in the range of 10-300 K and 0-29 GPa. With a surface normal in the (1, 1, 1) direction, we were able to measure all six Raman-active modes predicted (Figs. 5.7, 5.8) for space group $Fd\bar{3}m$ [171] without a specific polarization condition, which is difficult to fully control given the stress-induced birefringence in diamond [172, 173]. The six modes we observed are consistent with previous optical Raman measurements in $Cd_2Os_2O_7$ [63] and other materials of the same space group, such as $Cd_2Re_2O_7$ [174] and AOs_2O_6 (A = K, Rb) [175, 176]. These peaks are typically assigned as $T_{2g}(1)$, E_g, $T_{2g}(2)$, $T_{2g}(3)$, A_{1g} and $T_{2g}(4)$ from low to high frequencies. Since all Cd and Os atoms are located at sites of inversion symmetry, all six optical Raman active modes correspond to the vibration of oxygen atoms [171, 175]. Among these modes, only the $T_{2g}(2)$ mode represents the vibration of oxygen atoms O' occupying $8b$ sites, which could be depicted by a distortion of the Cd_4-O tetrahedral cage [177]. The remaining five modes are all attributed to the motion of oxygen atoms O occupying $48f$ sites, representing Cd-O stretching, O-Cd-O bending, O-O stretching, O-Os-O bending, and Os-O stretching in the ascending frequency sequence [177].

We show representative raw Raman spectra between 100 and 1000 cm^{-1} (12.4 to 124 meV) at T = 10 K from low pressure to 28.3 GPa (Fig. 5.7), and around 29 GPa from 10 K to 295 K (Fig. 5.8). These two sets of data enclose the most important boundary of the phase space we have explored (individual $P - T$ points are marked by grey crosses in the phase diagram in Fig. 5.11). Our search was not able to reach the quantum critical pressure at P_c = 35.8 GPa, but it does cross the AIAO antiferromagnetic phase boundary as a function of pressure at T = 150 K and 215 K (Fig. 5.11). Lattice distortion or symmetry changes typically will generate dramatic changes in the Raman spectrum. Specially for a change from the $Fd\bar{3}m$ to the $F\bar{4}3m$ group in $Cd_2Os_2O_7$, the number of Raman active modes will change from 6 to 15 [175], with additional peaks showing up from the vibrations of Cd and Os atoms due to the inversion symmetry breaking. One soft mode of particular interest is the Raman inactive mode with A_{2u} symmetry in space group $Fd\bar{3}m$, which will become Raman active in the $F\bar{4}3m$ structure with $A1$ representation. This low-frequency
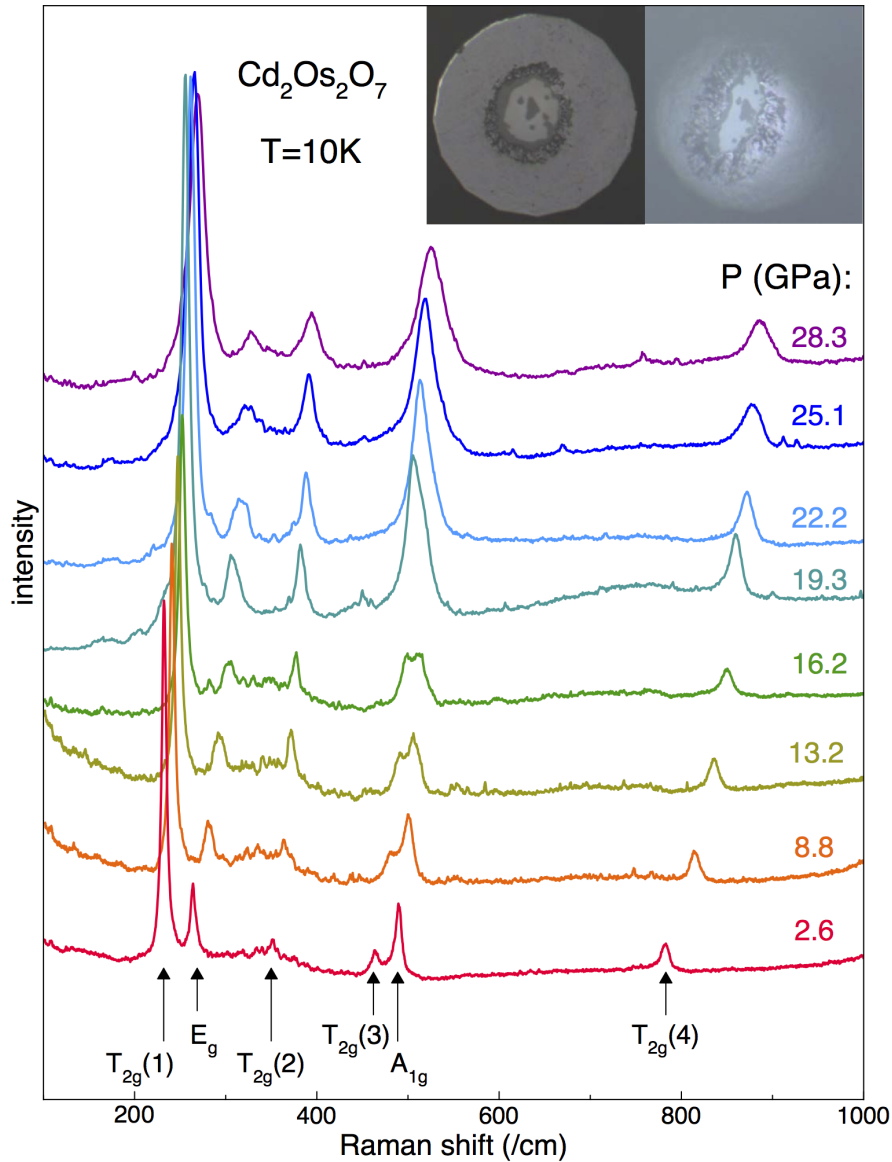
Figure 5.7: Raman spectra at $T = 10$ K for different pressures. All six Raman active modes have been observed up to 28.3 GPa and are labeled. Pictures of the pressure chamber at the lowest (left) and highest (right) pressure are shown in the inset.

mode has been observed in $Cd_2Re_2O_7$ at low temperature [174]. Some of our Raman spectra were taken in an extended range down to 20 cm^{-1} (2.5 meV), but no peaks with consistent behavior in temperature and pressure have been observed. In addition, our spectrometer is not specialized for low frequency range, where some electronics designed to suppress elastic scattering background make it difficult to distinguish real signals of low-energy Raman modes. Nevertheless, the fact that the Raman spectra stay unchanged indicates that there is no symmetry change at finite
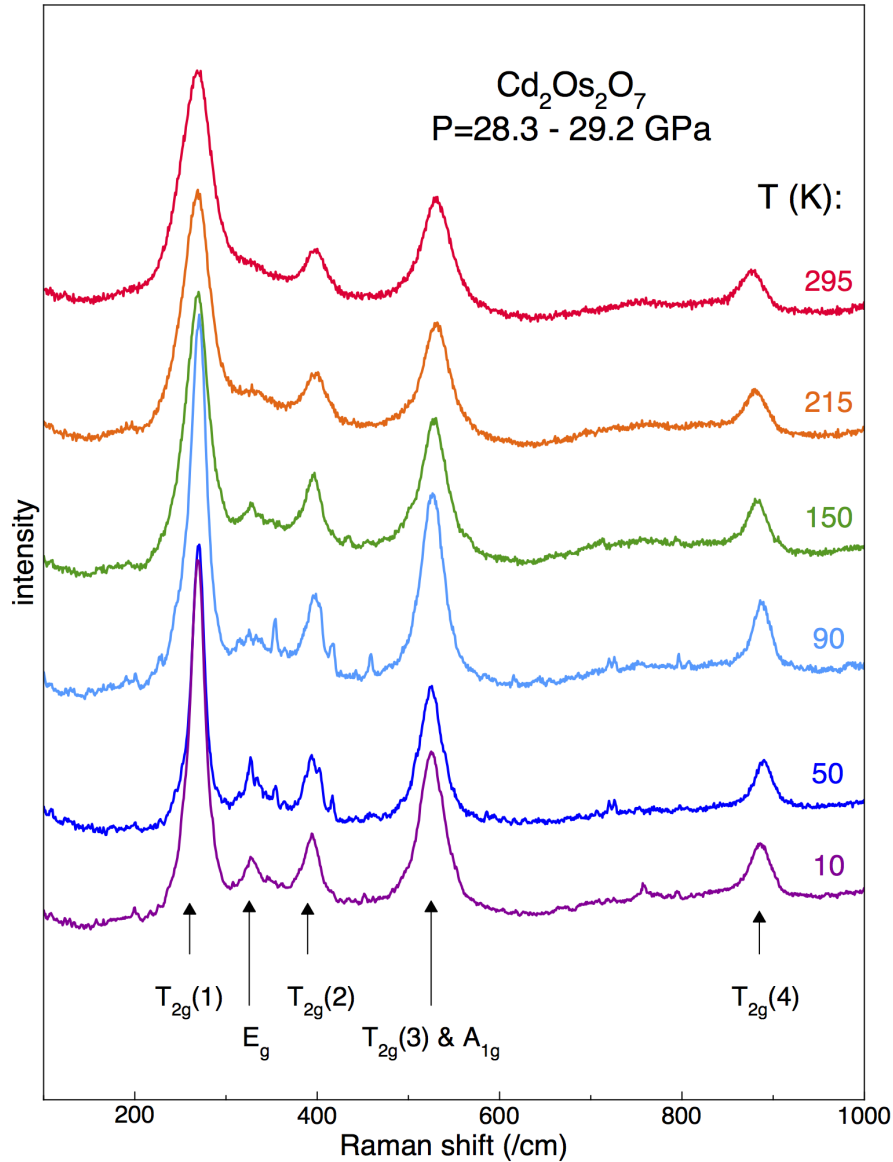
Figure 5.8: Raman spectra at the highest pressure point from T = 10 K to 300 K. All six Raman active modes have been observed from 10 K to room temperature at 28.3-29.2GPa and are labeled.

temperature phase transitions.

The analysis of Raman modes is often discussed in terms of wave number and intensity. In our high pressure experiment, the wave number could be determined within the relative precision of $\sim 1\ 10^{-3}$ at low pressure and $\sim 3\ 10^{-3}$ at the high pressure end with a well-preserved sample condition. The evolution of wave number vs pressure for all the six modes at T = 10 K and 295 K are shown in Fig. 5.9. All six modes are getting stiffer under pressure, which is the direct effect of enhanced short-
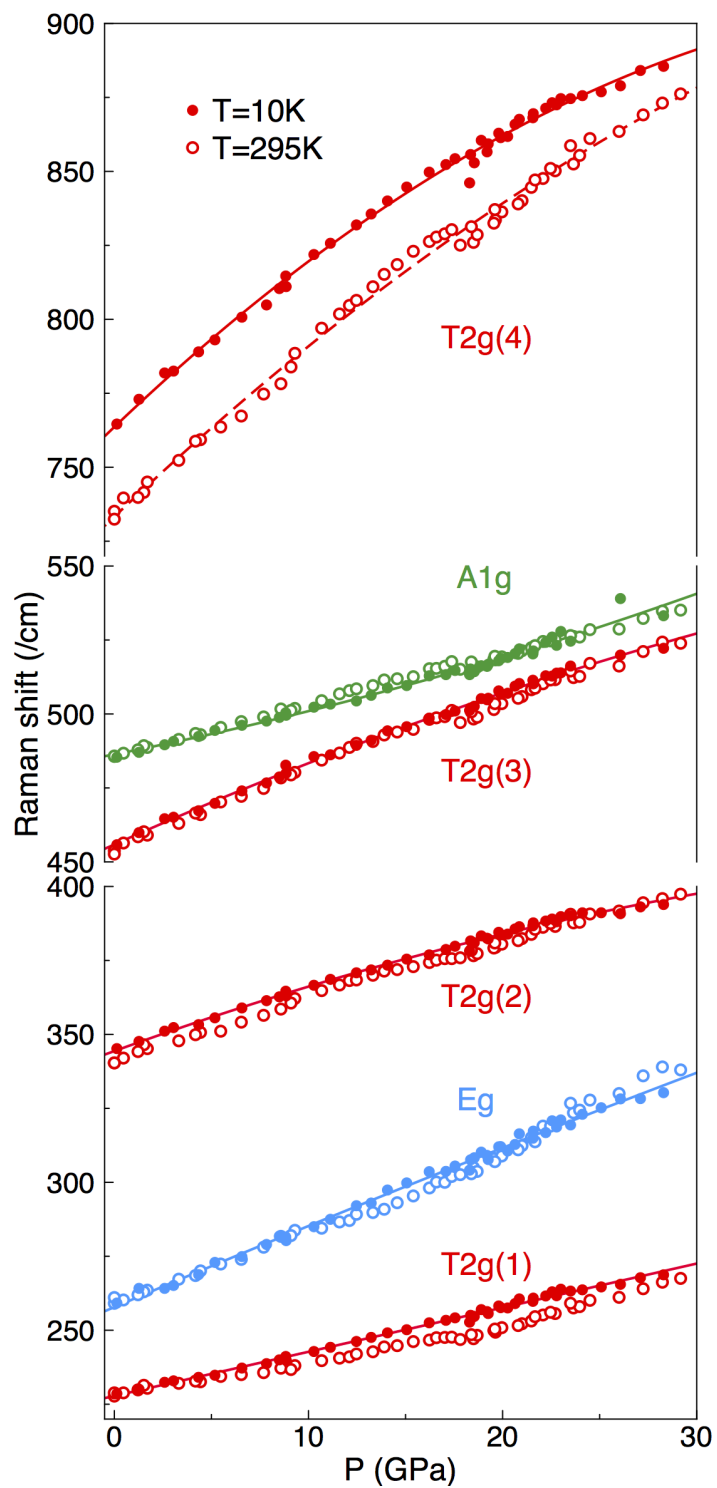
Figure 5.9: Raman shift vs. pressure. The pressure dependence of all six Raman active modes in $Cd_2Os_2O_7$ at $T = 10$ K (solid circles) and 295 K (open circles). The lines are guides to the eye.

range interactions from the squeezed unit cell. One difficulty in determining wave number is to distinguish the $T_{2g}(3)$ and A_{1g} peaks, which are close by at ambient condition but get even closer with increasing pressure as the pressure dependence of the lower energy mode $T_{2g}(3)$ is stronger (Fig. 5.9). This introduces additional systematic errors in measuring the Raman shifts. The relative changes of all six modes over a 29 GPa pressure range (ω(29GPa)- ω(0))/ ω(0)) are: 17.6%, 27.4%, 14.1%, 14.6%, 9.8% and 15.8%, respectively (Fig. 5.9).

The stronger pressure dependence of E_g indicates a strong anharmonic component in the vibration of O(1), a conclusion which is also supported by the large temperature dependence of $T_{2g}(4)$ (Fig. 5.9). Due to an offset from its ideal position, the oxygen atom O(1) at the $48f$ site manifests vibrations with high anharmonicity, which has been discussed for $Tb_2Ti_2O_7$ [178, 179] and can be characterized by $\sqrt{\langle u \rangle^2}/d$, where u is the vibration amplitude and d is the bond length between oxygen and adjacent Tb or Ti atoms [178]. Not all modes are affected by this anharmonicity due to symmetry constraints. For example, $T_{2g}(1)$, $T_{2g}(3)$ and A_{1g} modes show no obvious temperature difference and only moderate pressure dependence. While the E_g mode shows strong pressure dependence, it has barely any temperature dependence. In contrast with temperature tuning [148], we have observed a slight evolution of the O($48f$) coordinate x towards being more imperfect under pressure (Fig. 5.5), which will enhance the anharmonicity of oxygen vibrations. The E_g mode could be more sensitive to this distortion, thereby yielding its enhanced pressure dependence.

Typically, the Raman scattering intensity contains significant information to resolve lattice symmetry. However, intensity is not a well-defined quantity in our experiment due to the polarization effects from the diamond anvils, which changes with the strain distribution under pressurization and is hard to characterize. With the intensity of Raman modes showing a strong polarization dependence, the evolution of intensity, even relative intensity, will be difficult to analyze and even could be misleading.

5.4 Discussion

Our x-ray diffraction results (Figs. 5.2, 5.3, 5.4, 5.6) have clearly shown a phase transition around 36 GPa, where the breakdown of AIAO magnetic order and a coincident change of lattice symmetry are most clearly reflected by the integrated intensity of the magnetic peak at (6, 0, 0) and the charge diffraction peaks at both (6, 0, 0) and (4, 2, 0) (Fig. 5.10). The continuous nature of this quantum phase transition is manifested by the smooth evolution of the lattice constant (Fig. 5.5),
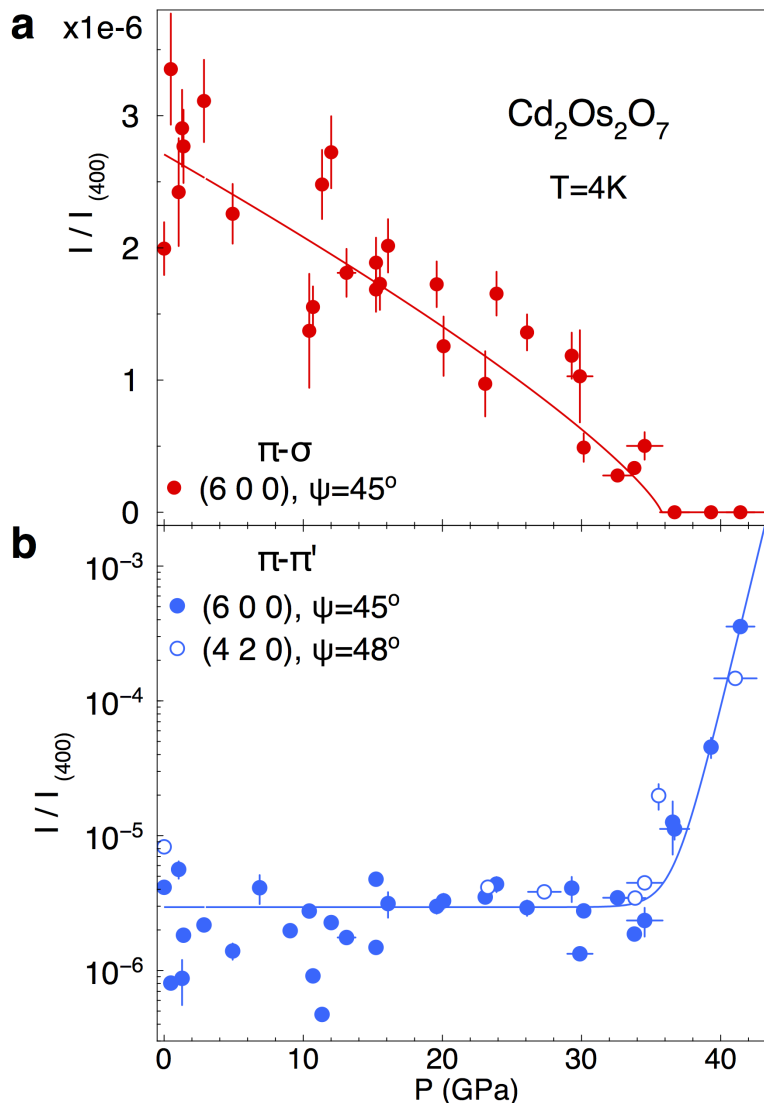
Figure 5.10: Continuous magnetic and structural quantum phase transitions (a) Magnetic diffraction intensity was measured at $(6, 0, 0)$ and in the $\pi - \sigma$ channel, with a power-law fit (solid line) to model the evolution over the whole pressure range. (b) Lattice diffraction intensities, measured at both the $(6, 0, 0)$ and $(4, 2, 0)$ orders in the $\pi - \pi'$ channel, indicate a continuous switching between the $Fd\bar{3}m$ and $F\bar{4}3m$ space groups with a phase boundary that rises effectively exponentially.

the gradual suppression of magnetic scattering intensity below P_c (Fig. 5.10a), and the continuous rise of lattice scattering intensity at $(6, 0, 0)$ and $(4, 2, 0)$ above P_c (Figs. 5.10b). Moreover, the ATS resonance profile, which is very sensitive to small local distortions, stay unchanged through the transition (Fig. 5.3, 5.6), providing strong evidence for a second-order phase transition.

For magnetic states, $I_{(6,0,0), \pi-\sigma} \sim \langle m \rangle^2$, where $\langle m \rangle$ is the staggered moment size,

i.e. the antiferromagnetic order parameter. A fit to the intensity over pressure $I \sim (P_c - P)^{2\beta}$ yields $P_c = 35.8 \pm 0.7$ GPa and a critical exponent $\beta = 0.40 \pm 0.04$ for $\langle m \rangle$, which has no strong deviation from mean-field theory [1]. From energetic considerations of localized $3d$ - $5d$ spins [180, 181], our magnetic diffraction results at the low temperature limit of 4 K also provide a means to estimate the AIAO magnetic phase boundary through $T_N \sim L \sim \langle m \rangle^2$, where L is the external magnetostriction that develops under $\langle m \rangle$. In AIAO-ordered pyrochlores, where the cubic lattice symmetry is preserved by the magnetic order and the phase transition is continuous, the external magnetostriction L is difficult to observe over the lattice's thermal expansion. Nevertheless, a non-monotonic evolution of the lattice constant with temperature, $a(T)$, for AIAO order at very low T has been demonstrated in $Nd_2Ir_2O_7$ ($T_N = 33.5$ K and $\Delta a/a \sim 1 \ 10^{-4}$) [182]. Following this logic, we identify the magnetic phase boundary $T_N(P)$ of $Cd_2Os_2O_7$ in Fig. 5.11 via the relationship $T_N \sim I \sim \langle m \rangle^2$. At high pressure, for $P > P_c$, the presence of a charge resonance at (4, 2, 0) verifies that the unoccupied t_{2g} orbitals remain the same in promoting the resonance behavior (Figs. 5.3, 5.6e, 5.6f). At the same time, the absence of a resonance at (6, 0, 0) importantly marks the vanishing of the staggered moment $\langle m \rangle$ and the long-range antiferromagnetic order (Figs. 5.3, 5.6c).

We believe that the high-pressure phase is most likely magnetically disordered. Spins are still configured as corner-shared tetrahedra networks with axial single-ion anisotropy along the <1 1 1> direction. Thus ferromagnetic interactions will manifest strong geometric frustration [142, 183, 184]. The pyrochlore lattice also prefers long-range order with a wave vector of q_{order} = (000) [142], but no commensurate antiferromagnetic peaks have been observed in our experiment. Moreover, tuning by either chemical doping or pressure drives the ratio of the magnetic interaction strength to the hopping integral smaller in $A_2(Os,Ir)_2O_7$. With an increasing electron density under 15% volume reduction by pressure, and moving away from the strong interaction strength limit [147], one would not naturally expect a ferromagnetic ground state. Finally, ferromagnetic quantum phase transitions, as well as commensurate-incommensurate antiferromagnetic transitions, are first order, which would contrast with the continuous AIAO quantum phase transition observed in our experiment.

The continuous increase of charge diffraction intensity beyond P_c can be regarded as the evolution of a new order parameter. As we have discussed before, the fact that (6, 0, 0) and (4, 2, 0) become non-forbidden corresponds to the broken inversion
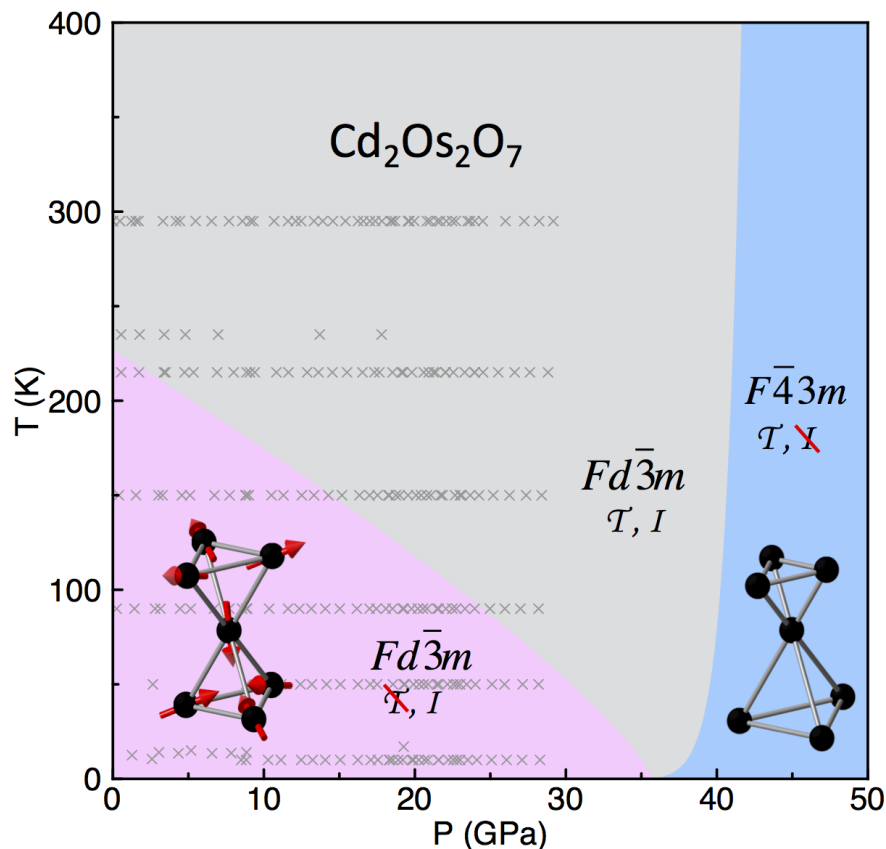
Figure 5.11: $P - T$ phase diagram of Cd$_2$Os$_2$O$_7$. The Cd$_2$Os$_2$O$_7$ lattice retains its cubic symmetry throughout the probed $P - T$ phase space, but continuously transitions between $Fd\bar{3}m$ and $F\bar{4}3m$ space groups. The $Fd\bar{3}m$ lattice symmetry was verified by optical Raman scattering from 0 - 29 GPa and 10 - 300 K (grey crosses), while both phases of magnetism and structure (pink and blue shading) were inferred from x-ray diffraction measurements at $T = 4$ K. The two phase lines effectively converge at the same quantum critical region, dividing the $P-T$ space into three phases with distinct time-reversal ($\mathcal{T}$) and inversion ($\mathcal{I}$) symmetry properties. The metallic paramagnetic phase in the low-pressure $Fd\bar{3}m$ space group has both spatial inversion ($\mathcal{I}$) and time reversal ($\mathcal{T}$) symmetries. In the low-pressure AIAO phase (inset), time reversal symmetry is broken. On the high-pressure side, the $F\bar{4}3m$ space group breaks the spatial inversion symmetry, introducing a tetrahedral breathing distortion (inset), and restores the time reversal symmetry with disordered spins.

symmetry, which derives from differently-sized adjacent tetrahedra of the Os and Cd sublattices (Fig. 5.11, inset) and can be regarded as fully-softened breathing modes with spontaneous symmetry breaking [163–170]. These breathing modes disappear above $k_B T_c \sim K|\Delta_{Os}|^2$, with the lower $F\bar{4}3m$ symmetry replaced by the higher $Fd\bar{3}m$ symmetry with adjacent tetrahedra of equal size. Here K is the vibrational elastic

constant and Δ_{Os} is the amplitude of the Os tetrahedron breathing mode. We expect $T_c \sim I$, given that the measured x-ray diffraction intensities (Fig. 5.10b) depend on these lattice distortions as $I \sim |f_{Os}\Delta_{Os} + f_{Cd}\Delta_{Cd}|^2$, where $f_{Os/Cd}$ are x-ray atomic form factors. As we have observed no charge diffraction intensity at $P = 34.5$ GPa and very weak intensity at $P = 36.7$ GPa, taking $T_c \sim 4$ K at the measured P_c is a reasonable benchmark while mapping $I_{(6, 0, 0), (4, 2, 0), \pi - \pi'} \sim |f_{Os}\Delta_{Os} + f_{Cd}\Delta_{Cd}|^2 \sim K|\Delta_{Os}|^2 \sim T_c$, leading to the striking concave high-pressure phase boundary in Fig. 5.11. It is of particular interest that the high-pressure phase line manifests a curvature that rises with a power much greater than 1 (Figs. 5.10b, 5.11), strongly deviating from a mean-field prediction. Rather, this is in the spirit of theoretical discussions of strong-coupled quantum critical behavior in AIAO pyrochlores [17].

Within our experimental resolution of ~1 GPa at $T = 4$ K, the two phase lines set by two different types of order parameters converge at the same point, thus dividing the $P - T$ phase space into three areas with different symmetry properties. From Landau's phase transition theory, these two quantum phase transitions should be either separated or share a first-order phase line. However, the concurrence within experimental resolution and the clear deviation from the mean-field prediction stimulate a discussion of strong coupling in the quantum critical region.

The $P - T$ phase space is divided into three regions with distinct symmetry properties (Fig. 5.11). This quantum phase transition with unique symmetry properties also distinguishes itself from its counterpart at finite temperature as well as from previous studies of quantum phase transitions in $5d$ AIAO materials. In the family $Ln_2Ir_2O_7$ (Ln = Eu, Sm, Nd, Pr), the ordering temperature could be tuned by chemical substitution with a phase transition happening between Nd and Pr [150, 151], while $Pr_2Ir_2O_7$ stayed a non-magnetic metal down to the lowest measured temperature [147, 185, 186]. Quantum critical behavior such as non-Fermi liquid features have been studied by ARPES in $Pr_2Ir_2O_7$, which emerges after the breakdown of an insulating antiferromagnetic state [155]. According to x-ray diffraction data, $Pr_2Ir_2O_7$ preserves inversion symmetry at low temperature [182], which is also the model used to discuss non-trivial quantum critical behavior in theoretical predictions, where a major assumption of inversion symmetry being preserved was used to construct band structure degeneracy [17]. In spite of the inapplicability of this assumption to $Cd_2Os_2O_7$, as shown by our experimental results, the high pressure phase line demonstrates a curvature similar to that predicted by theory [17], a strong signature of nontrivial quantum criticality. Therefore, the break from mean-field

behavior in this system might not depend on detailed band structure, but could be more universal.

In the phase diagram of $Cd_2Os_2O_7$ (Fig. 5.11), the quantum critical regime above the critical point manifests both spin fluctuations and a lattice breathing mode that get soft simultaneously at the quantum critical point. The exact nature of their interaction will help determine the character of the high-pressure phase, but is likely complicated. Although spin-phonon coupling is known to generate unequal bond lengths in spin-Peierls dimers and antiferromagnetic superlattices [180], in the AIAO phase the breathing phonons are not fully softened, at least in the static limit, where AIAO order only induces an external magnetostriction with a homogenous expansion [182]. In the high-pressure phase, a breathing lattice could in principle still permit AIAO spin configurations on different sized tetrahedra, despite a loss of site inversion symmetry in the $F\bar{4}3m$ space group, but our diffraction result did not show any AIAO order at high pressure. In short, these two modes are competing with each other in both the low-P and high-P phases, and this nature is most clearly reflected by the reduction of lattice symmetry from the $Fd\bar{3}m$ to $F\bar{4}3m$ group when the AIAO order breaks down. Nevertheless, the quantum critical region should involve multiple fluctuations from both the spin and lattice degrees of freedom, with further studies required to specify the microscopics.

The relationship between the magnetic and metal-insulator transitions is also intriguing. The increased bandwidth under pressure suggests that the electronic properties of $Cd_2Os_2O_7$ in the high-pressure $F\bar{4}3m$ state become more metallic, potentially even superconducting in analogy to superconducting $Cd_2Re_2O_7$ with its broken inversion symmetry [187]. AIAO magnetic order and the metal-insulator transition respond similarly to compression across the $P - T$ phase diagram. Our projected magnetic phase boundary in Fig. 5.11 gives $\frac{dT_N}{dP} \sim -5.0$ K/GPa at P=0, which is consistent with $\frac{dT_{MIT}}{dP} = -4$ K/GPa in $Cd_2Os_2O_7$ measured by electrical transport over the first 2 GPa range [148]. Comparing the two 5d AIAO ordered compounds with clear high-temperature metallic states, we find an average $\frac{dT_N}{dP} \sim -6.5$ K/GPa over the whole AIAO phase in $Cd_2Os_2O_7$ and a $\frac{dT_{MIT}}{dP} \sim -5.8$ K/GPa in $Nd_2Ir_2O_7$ [151, 153]. This comparison holds true despite large differences in T_N of 227 K and 33.5 K, respectively. Thus it is very likely that an insulator-metal transition happens at the same critical point P_c.

The coupling between quasiparticle fluctuations with spin and lattice, however, are more complicated. So far, the discussion has been limited to iridates and has

assumed band touching of different types including Weyl nodes, Dirac nodes or a simple quadratic band touching at $Q = 0$ [17, 155, 186] to specify and simplify the model. The coupling mechanisms of electron-spin [17] and electron-lattice [188] have been established under these assumptions and quantum critical behavior beyond mean-field theory has been predicted [17]. The band structure in various systems can be more complicated, but the advantage of involving low carrier density states, for instance via an insulator-metal transition at the quantum critical point, could be universal. With the Fermi surface fully gapped, quasiparticle fluctuations would involve all itinerant states in reducing the screening of the Coulomb U, and the increased interaction range would then help stabilize a continuous quantum phase transition [17, 186]. Indeed, at the ambient-pressure metal-insulator transition in $Cd_2Os_2O_7$, an increase in U from 0.8 to 1.5 eV in the theoretical modeling is consistent with the observed spectral weight shift in infrared conductivity over the broad range of 0 - 4 eV [189].

In the quantum critical region in Fig. 5.11, soft AIAO spin fluctuations and lattice breathing modes could exist and compete, and further couple to quasiparticle fluctuations. The competition between spin and lattice degrees of freedom might explain the remarkable concave-shaped phase line at high pressure, as TC scales to pressure with a non-trivial exponent much larger than one, a characteristic of strongly-coupled quantum criticality [17]. We note as well that the quantum critical region is asymmetric in $P - T$ phase space, as the magnetic and structural phase lines approach P_c with different asymptotic behavior (Fig. 5.11). A major reason for most quantum phase transitions in 3-dimensional materials to exhibit mean-field behavior is the fluctuation of a single order parameter being the only soft (critical) mode (Chapter 1). To breakout of this framework, the quantum behavior should coherently involve multiple soft modes, which is the idea of a strongly-coupled quantum critical point [16, 17]. Our study of $Cd_2Os_2O_7$ has demonstrated an experimental realization of this scenario with multiple fluctuation modes from spin, lattice and quasiparticles as well as signatures deviating from mean-field predictions. In addition, the time-reversal and inversion symmetry properties at the quantum critical point could fundamentally determine the ground state of $Cd_2Os_2O_7$ at high pressure, generating even more exotic critical behavior. The phase diagram in $5d$ pyrochlores with consideration of spin-orbit coupling have been intensively studied theoretically with a strong dependence on the underlying symmetry flow. For instance, one could get topological insulators, Dirac semimetals, Weyl semimetals, etc. in $5d$ pyrochlore iridates [147, 188] by removing or introducing time-reversal

symmetry and inversion symmetry since the band degeneracy they determine will directly affect band topology. Moreover, a parity-breaking liquid crystal has been discovered in the spin-orbit-coupled noncentrosymmetric system, $Cd_2Re_2O_7$ [190], and odd-parity superconductivity has been theoretically proposed [191, 192].

The scenario of a metal-insulator transition evolving together with a magnetic transition naturally brings up the consideration of the magnetically-driven metal-insulator transition, which we have discussed in Chapter 1. From the band structure perspective, the Os $5d$ t_{2g} band in $Cd_2Os_2O_7$ is neither degenerate and forming a $S = 3/2$ state under Hund's rule, as indicated by the reduced staggered moment $\langle m \rangle = 0.59$ μ_B/Os, nor cleanly separated into several narrow bands as demonstrated for a perfect Os-O_6 octahedron [148, 193, 194]. Instead, the t_{2g} orbitals in $Cd_2Os_2O_7$ extend continuously over a spectral width of order 2 eV [193] from the combined effect of U (~1 eV) [195], spin-orbit coupling (~0.35 eV) [194], and trigonal distortion (~0.3 eV) on the Os-O_6 octahedron [159]. Through the continuous quantum phase transition, the overall stability of the empty t_{2g} band is verified by the constant charge resonance profile at (4, 2, 0), with a coarse energy resolution slightly above 1 eV. Therefore, the Mott-Hubbard mechanism of exchange coupling J opening an insulating gap will not apply to $Cd_2Os_2O_7$. Alternatively, a Slater mechanism has been proposed. In contrast to a traditional Slater mechanism where an insulating gap is opened by the folding of the Brillouin zone due to a doubling of unit cell size when a superlattice is formed [36] (Chapter 1), AIAO order preserves the size of the unit cell. However, the formation of antiferromagnetic order from the paramagnetic state would influence the oscillating dynamic component of the quasiparticle self-energy. Although the frequency-independent Hartree part fails to open up a full gap, which is why the system is a paramagnetic metal at high temperature, it could assist the gap opening by producing preexisting mass renormalization when the antiferromagnetic order creates extra repulsion between the empty and filled bands [37]. This cooperative opening of an insulating gap involves a shifting of bands along with the magnetic order parameter, and could be continuous as experimentally observed. Specifically, if the gap opens through a critical state of singular points at the Fermi surface, instead of a removal of states altogether, its thermodynamics could fit the Lifshitz description [195, 196].

The quantum phase transition in $Cd_2Os_2O_7$, with its interwoven spin, orbit, lattice, and charge degrees of freedom, contrasts sharply with systems that have a partially-gapped Fermi surface, exemplified by itinerant spin density waves where persistent

carriers screen spin fluctuations and lead to mean-field behavior [16, 17, 24]. The cubic AIAO antiferromagnet also differs from itinerant ferromagnets, where strong spin and charge mode coupling at wave vector $Q = 0$ categorically induces first-order quantum phase transitions [5, 6]. Spin-orbit coupling in $5d$ systems is regarded as intermediately strong [147], and pressure drives U/t smaller with increasing kinetic energy t, away from the strong-correlation limit. Pressure tuning thus likely induces a continuous quantum phase transition while still preserving non-trivial quantum criticality in this $5d$ antiferromagnet. By Luttinger's theorem, a continuous insulator-metal transition would result in either a carrier-mass enhancement or non-Fermi-liquid behavior [72] in $Cd_2Os_2O_7$'s high-pressure phase, and the broken inversion symmetry sets the conditions for odd-parity superconductivity. A microscopic theory remains to be developed to describe the interaction between the AIAO spin fluctuations, breathing phonon modes, and quasiparticle excitations, especially taking into consideration the symmetry, chirality, and wave vector characteristics of each.

Chapter 6

CONCLUSIONS AND OUTLOOK

My Ph.D. dissertation has focused on quantum phase transitions in antiferromagnetic materials ranging from $3d$ to $5d$ electrons, relating various types of magnetic ordering to other correlated electron phenomena such as metal-insulator transitions and superconductivity. Using high-pressure as the major tuning technique at cryogenic temperature, I have developed and utilized multiple probes in order to address the issue of electronic instabilities and symmetry evolution through quantum phase transitions. In particular, my instrumental development effort in resonant x-ray magnetic diffraction and optical Raman spectroscopy under high pressure could be applied broadly to a great many model systems for a variety of scientific topics.

Motivated by the pursuit to reveal microscopic mechanisms of spin-fluctuation-mediated superconductivity, we have studied Mo_3Sb_7 and MnP, both of which manifest a pressure-dependent superconducting state potentially intertwined with magnetism. In Mo_3Sb_7, the superconducting transition temperature was doubled under pressure. However, given the small itinerant moments and weak spin fluctuation effects, it was concluded that the superconductivity is most likely to be phonon-mediated and we attributed the increase of T_c to a modified phonon density-of-states in the high-symmetry cubic structure. In MnP, we have discovered a helical magnetic order with a tightened spiral pitch near the pressure-induced superconductivity. The unique spiral type of spin fluctuations would naturally suppress phonon-mediated BCS pairing due to the ferromagnetic component, leaving spin fluctuations as a favorable mediating channel. We point out that the spiral pitch in the MnP family, with about 40 available compounds, provides a tuning parameter between ferromagnets and antiferromagnets at long and short wavelengths, respectively. Both magnetic states potentially could promote superconductivity mediated by spin fluctuations, albeit of very different types.

Our x-ray magnetic diffraction experiment on the $5d$ pyrochlore $Cd_2Os_2O_7$ under high pressure has discovered the breakdown of the AIAO antiferromagnetic order accompanied by an inversion symmetry breaking of the lattice, with a potential insulator-metal transition occurring simultaneously. Combining the x-ray measurements with optical Raman spectroscopy, we have traced the underlying

symmetry changes across the $P - T$ phase space, confining the allowable ground states within certain time-reversal and inversion symmetry conditions. The quantum phase transition in $Cd_2Os_2O_7$ is of a continuous nature, with striking deviations from a mean-field form at high pressure. This is presumably due to a strong interaction of spin fluctuations, lattice breathing modes and quasiparticle excitations, which may be an experimental realization of the theoretically proposed strongly-coupled quantum criticality. $Cd_2Os_2O_7$ stands out as one of the rare cases of quantum phase transitions beyond the mean-field regime in three-dimensional materials.

Similar resonant x-ray magnetic diffraction inquiries should be conducted in pyrochlore-based AIAO iridates. As mentioned in Chapter 5, similar to $Cd_2Os_2O_7$, pyrochlore-structured $A_2Ir_2O_7$ (A = Sm, Eu and Nd) manifests a metal-insulator transition concurrent with the formation of AIAO antiferromagnetic order. The quantum phase transition in $A_2Ir_2O_7$ has been studied by chemical tuning: T_{MIT} is suppressed by varying elements on the A site and finally $Pr_2Ir_2O_7$ remains metallic down to the lowest measured temperature. However, this A-site chemical-doping driven quantum phase transition preserves lattice inversion symmetry in $Pr_2Ir_2O_7$, in contrast with our pressure study of $Cd_2Os_2O_7$. A pressure-induced insulator-metal transition has also been reported for both $Nd_2Ir_2O_7$ and $Eu_2Ir_2O_7$, but with no direct information about the AIAO order or symmetry evolution. Therefore, a comparative study of $A_2Ir_2O_7$ (A = Sm, Eu and Nd) will shed light on the understanding of how the AIAO magnetic order is related to phonon modes and the formation of an insulating gap. Experimentally, although there is no magnetic resonance at the Ir L_2 edge, the resonant effect is significantly enhanced at the Ir L_3 edge (E = 11.215keV) by a factor of ~1000. Moreover, the relatively lower transition temperature at ambient condition implies a lower critical pressure, making experimental inquiries more accessible. It remains to be seen whether magnetic iridates under pressure would bring the same strongly-coupled critical phenomena as their osmate counterpart.

In addition to this pyrochlore family with magnetic and metal-insulator transitions, resonant x-ray magnetic diffraction at the Ir L_3 edge would also contribute significantly to the long-standing interest in quantum spin liquids. Due to the combined effects from crystal field splitting and spin-orbit coupling, the correlated $5d$ electrons residing on the Ir ions can be described by an effective J_{eff} = 1/2 spin. Therefore, iridates on a honeycomb lattice could potentially host quantum spin liquid states proposed for spin-1/2 systems with the interactions between nearest neighbors of the XX, YY, or ZZ type [147, 197, 198]. So far, candidates such as Na_2IrO_3 and

α-Li$_2$IrO$_3$ are magnetically ordered at low temperature. While more candidate materials have been proposed, pressure could provide an alternative way of tuning magnetic exchange conditions other than the chemical synthesis approach, and possibly destabilize the long-range order to achieve a quantum spin liquid state. This evolution will be most clearly tracked with the capability of directly probing magnetically ordered states with microscopic details under pressure. With further instrument development of resonant magnetic diffuse scattering under pressure, not only long-range order but also short-range magnetic fluctuations possibly could be probed under pressure, which could provide direct evidence of excitation modes in the reciprocal space to be examined for quantum spin liquid states. Though the cross section for magnetic scattering is typically small and the signal is further reduced due to a short-range correlation, the considerable enhancement at the Ir resonant edge will serve as an essential compensation.

Further extension of our successful experience with resonant x-ray diffraction at the Os L_2 edge allows the investigation of magnetism and orbital ordering at the L edges of Ta, Re, Ir, Pt, Pb, Tl, etc., opening up a series of experiments of $5d$ electron systems. Materials based on these elements manifest the complexity arising from competing energy scales of the on-site Coulomb interaction (U), spin-orbit coupling (λ) and hopping integral (t), thus becoming a vibrant playground to study correlated states.

Furthermore, there remains plenty of interest in the macroscopic understanding of both metal-insulator transitions and superconductivity under pressure, so it is worth pointing out some future scientific opportunities based on experimental developments.

In Cd$_2$Os$_2$O$_7$, the metal-insulator transition remains one missing piece of the puzzle as the magnetic order and lattice symmetry have been directly probed by x-rays. Given the high critical pressure value, with the extra difficulty of making electrical contacts on the semimetallic surface, measuring the $T_{\mathrm{MIT}}(P)$ phase boundary using electrical transport measurements is challenging. Instead, non-contact techniques such as optical spectroscopy are often preferred. Our Raman experiment has demonstrated a successful incorporation of optics into a high-pressure sample environment. Considering the distinct signature of a metal-insulator transition manifested by optical reflectivity and the absorption coefficient, the instrument we set up for Raman spectroscopy should be sufficient to probe the transition under high pressure. With additional time-resolved capabilities, such as a pump-probe tech-

nique, dynamic properties of phonon modes and electronic responses could also be tracked, potentially allowing a more detailed discussion of critical behavior and the mechanism of the metal-insulator transition.

As for superconductivity, the discussion of spin-fluctuation-mediated Cooper pairing will only be definitive if the superconducting gap symmetry can be clearly resolved. Under ambient conditions, both phase-sensitive quantum interference devices and amplitude-sensitive optical Raman spectroscopy have been used to determine the parity of the superconductivity [199]. While the former requires a strict remnant field condition that is difficult to achieve in a high-pressure sample environment, polarization-sensitive Raman spectroscopy is more promising to cooperate with a high-pressure environment. Raman spectroscopy could measure magnetic excitations at the same time, which presumably could establish directly the connection between spin fluctuations and superconductivity. Starting from our current high-pressure Raman setup, there are several technical issues to overcome, namely surface conditions, sample heating, suppression of fluorescence from both sample and background, and weak signals of the superconducting gap state. In addition, diamonds under stress could further complicate the polarization effect. Potentially, time-resolved Raman spectroscopy could solve some of these issues and provide a unique perspective into the long-standing topic of unconventional superconductivity.

BIBLIOGRAPHY

[1]   L. D. Landau. *Collected Papers of L. D. Landau*. Edited by D. ter Harr. New York: Pergamon Press, 1965. ISBN: 9781483152707.

[2]   K. G. Wilson and J. Kogut. "The renormalization group and the ϵ expansion". *Phys. Rep.* 12.75 (1974).

[3]   S.-K. Ma. *Modern Theory of Critical Phenomena*. The Benjamin/Cummings Publishing Company, Inc., 1976. ISBN: 0805366717.

[4]   J. A. Hertz. "Quantum critical phenomena". *Phys. Rev. B* 14.1165 (1976).

[5]   D. Belitz, T. R. Kirkpatrick, and Jörg Rollbühler. "Tricritical Behavior in Itinerant Quantum Ferromagnets". *Phys. Rev. Lett.* 94.247205 (2005).

[6]   M. Brando et al. "Metallic quantum ferromagnets". *Phys. Rev. Lett.* 88.025006 (2016).

[7]   Q. Si and F. Steglich. "Heavy fermions and quantum phase transitions". *Science* 329 (2010), pp. 1161–1166.

[8]   Y. Feng et al. "Itinerant density wave instabilities at classical and quantum critical points". *Nat. Phys.* 11 (2015), pp. 865–871.

[9]   T. Moriya. *Spin Fluctuations in Itinerant Electron Magnetism*. Berlin: Springer-Verlag, 1985. ISBN: 9783642825019.

[10]   T. Moriya. "Developments of the theory of spin fluctuations and spin fluctuation-induced superconductivity". *Proc. Jpn. Acad.* Ser. B 82.1 (2006).

[11]   J. Custers et al. "The break-up of heavy electrons at a quantum critical point". *Nature* 424 (2003), pp. 524–527.

[12]   Q. Gegenwart P.and Si and F Steglich. "Quantum criticality in heavy-fermion metals". *Nat. Phys.* 4 (2008), pp. 186–197.

[13]   L. Onsager. "Crystal Statistics. I. A Two-Dimensional Model with an Order-Disorder Transition". *Phys. Rev.* 65.117 (1944).

[14]   C. N. Yang. "The spontaneous magnetization of a two-dimensional Ising model". *Phys. Rev.* 85.808 (1952).

[15]   S. Sachdev. *Quantum Phase Transitions*. Cambridge, England: Cambridge University Press, 1999. ISBN: 0521514681.

[16]   D. Belitz, T. R. Kirkpatrick, and Thomas Vojta. "How generic scale invariance influences quantum and classical phase transitions". *Rev. Mod. Phys.* 77(2) (2005), pp. 579–632.

[17]   L. Savary, E. Moon, and L. Balents. "New type of quantum criticality in the pyrochlore iridates". *Phys. Rev. X* 4.041027 (2014).

[18] P. W. Anderson. "Resonating valence bonds: A new kind of insulator?" *Materials Research Bulletin* 8(2) (1973), pp. 153–160.

[19] P. W. Anderson. "The resonating valence bond state in La_2CuO_4 and super-conductivity". *Science* 235(4793) (1987), pp. 1196–1198.

[20] B. Keimer and J. E. Moore. "The physics of quantum materials". *Nat. Phys.* 13 (2017), pp. 1045–1055.

[21] N. D. Mathur et al. "Magnetically mediated superconductivity in heavy fermion compounds". *Nature* 394 (1998), pp. 39–43.

[22] Q. Si. "Global magnetic phase diagram and local quantum criticality in heavy fermion metals". *Physica B* 378.23 (2006).

[23] R. Jaramillo et al. "Breakdown of the Bardeen–Cooper–Schrieffer ground state at a quantum phase transition". *Nature* 459 (2009), pp. 405–409.

[24] Yejun Feng, A. Palmer, Yishu Wang, D. M. Silevitch, and T. F. Rosenbaum. "Direct probe of Fermi surface evolution across a pressure-tuned quantum phase transition". *Physical Review B* 91.155142 (2015). DOI: `10.1103/PhysRevB.91.155142`.

[25] R. Jaramillo et al. "Signatures of quantum criticality in pure Cr at high pressure". *Proc. Natl. Acad. Sci.* 107 (2009), pp. 13631–13635.

[26] R. Jaramillo et al. "Chromium at high pressures: Weak coupling and strong fluctuations in an itinerant antiferromagnet". *Phys. Rev. B* 77.184418 (2008).

[27] J. Bardeen, L. N. Cooper, and J. R. Schrieffer. "Theory of superconductivity". *Phys. Rev.* 108.1175 (1957).

[28] G. R. Stewart. "Heavy Fermion Systems". *Rev. Mod. Phys.* 56.755 (1984).

[29] R. Joynt and L. Taillefer. "The superconducting phases of UPt_3". *Rev. Mod. Phys.* 74.235 (2002).

[30] P. Monthoux, D. Pines, and G. G. Lonzarich. "Superconductivity without phonons". *Nature* 450.1177 (2007).

[31] D. van Harlingen. "Phase-sensitive tests of the symmetry of the pairing state in the high-temperature superconductors—Evidence for $d_{x^2-y^2}$ symmetry". *Rev. Mod. Phys.* 67.515 (1995).

[32] C. C. Tsuei and J. R. Kirtley. "Pairing symmetry in cuprate superconductors". *Rev. Mod. Phys.* 72.969 (2000).

[33] F. Kidwingira et al. "Dynamical Superconducting Order Parameter Domains in Sr_2RuO_4". *Science* 314 (2006), pp. 1267–1271.

[34] S. K. Sinha et al. "Study of coexistence of ferromagnetism and superconductivity in single crystal $ErRh_4B_4$". *Physica B* 109-110 (1982), pp. 1693–1698.

[35] N. F. Mott. "Metal-insulator transition". *Rev. Mod. Phys.* 40.677 (1968).

[36] J. C. Slater. "Magnetic effects and the Hartree-Fock equation". *Phys. Rev.* 82.538 (1951).

[37] R. Arita et al. "*Ab initio* studies on the interplay between spin-orbit interaction and Coulomb correlation in Sr_2IrO_4 and Ba_2IrO_4". *Phys. Rev. Lett.* 108.086403 (2012).

[38] L. Merrill and W.A. Bassett. "Miniature diamond anvil pressure cell for single crystal x-ray diffraction studies". *Rev. Sci. Instrum.* 45.290 (1974).

[39] W. B. Daniels and M. G. Ryschkewitsch. "Simple double diaphragm press for diamond anvil cells at low temperatures". *Rev. Sci. Instrum.* 54.115 (1983).

[40] Y. Feng et al. "Invited article: High-pressure techniques for condensed matter physics at low temperature". *Rev. Sci. Instrum.* 81.041301 (2010).

[41] S. V. Sinogeikina et al. "Online remote control systems for static and dynamic compression and decompression using diamond anvil cells". *Rev. Sci. Instrum.* 86.072209 (2010).

[42] Y. Feng, D. M. Silevitch, and T. F. Rosenbaum. "A compact bellows-driven diamond anvil cell for high-pressure, low-temperature magnetic measurements". *Rev. Sci. Instrum.* 85.033901 (2014).

[43] M. Riversa et al. "The COMPRES/GSECARS gas-loading system for diamond anvil cells at the Advanced Photon Source". *High pressure research* 28 (2008), pp. 273–292.

[44] D. J. Dunstain and I. L. Spain. "Technology of diamond anvil high-pressure cells: I. Principles, design and construction". *J. Phys. E: Sci. Instrum.* 22.913 (1989).

[45] M. I. Eremets. *High Pressure Experimental Methods*. New York: Oxford University Press, 1996. ISBN: 9780198562696.

[46] S. Klotz. *Techniques in high pressure neutron scattering*. CRC Press, Taylor & Francis Group, 2016. ISBN: 1439835624.

[47] I. N. Goncharenko et al. "Neutron diffraction studies of magnetic structure and phase transitions at very high pressures". *High Press. Res.* 14.41 (1995).

[48] J.-M. Mignot et al. "Single-crystal neutron diffraction under high pressures: valence instabilities in Tm monochalcogenides". *Hyperfine Interactions* 128 (1995), pp. 207–224.

[49] M. Blume. "Magnetic scattering of x-rays". *J. App. Phys.* 57 (1985), pp. 3615–3618.

[50] P. M. Platzman and N. Tzoar. "Magnetic scattering of x rays from electrons in molecules and solids". *Phys. Rev. B* 2.9 (1970).

[51] M. Brunel and F. de Bergevin. "Diffraction of x-rays by magnetic materials: II. Measurements on antiferromagnetic Fe_2O_3". *Acta. Cryst. A* 37 (1981), pp. 324–331.

[52] D. Gibbs et al. "Magnetic x-ray scattering studies of holmium using synchrotron radiation". *Phys. Rev. Lett.* 55.2 (1985).

[53] M. Blume and D. Gibbs. "Polarization dependence of magnetic x-ray scattering". *Phys. Rev. B* 37.4 (1988).

[54] T. Brückel et al. "First observation of bulk magnetic scattering using high-energy x-rays". *Act Cryst. A* 49 (1993), pp. 679–682.

[55] J. P. Hill et al. "Observation of x-ray magnetic scattering in Nd_2CuO_4". *Phys. Rev. B* 52.9 (1995).

[56] J. Strempfer et al. "The non-resonant magnetic x-ray scattering cross-section for photon energies up to 500keV". *Europhys. Lett.* 40 (1997), pp. 569–574.

[57] D. Gibbs et al. "Polarization and resonance properties of magnetic x-ray scattering in Holmium". *Phys. Rev. Lett.* 61.10 (1988).

[58] J. P. Hannon et al. "X-ray resonance exchange scattering". *Phys. Rev. Lett.* 61.10 (1988).

[59] E. D. Isaacs et al. "X-ray resonance exchange scattering in UAs". *Phys. Rev. Lett.* 62.14 (1988).

[60] J. P. Hill and D. F. McMorrow. "X-ray resonant exchange scattering: polarization dependence and correlation functions". *Acta Cryst. A* 52 (1996), pp. 236–244.

[61] L. Paolasini et al. "Magnetic ground state of pure and doped $CeFe_2$". *Phys. Rev. Lett.* 90.057201 (2003).

[62] B. Bohnenbuck et al. "Magnetic structure of $RuSr_2GdCu_2O_8$ determined by resonant x-ray diffraction". *Phys. Rev. Lett.* 102.037205 (2009).

[63] J. Yamaura et al. "Tetrahedral Magnetic Order and the Metal-Insulator Transition in the Pyrochlore Lattice of $Cd_2Os_2O_7$". *Phys. Rev. Lett.* 108.247205 (2012).

[64] C. Donnerer et al. "All-in–all-out magnetic order and propagating spin waves in $Sm_2Ir_2O_7$". *Phys. Rev. Lett.* 117.037201 (2016).

[65] D. H. Templeton and L. K Templeton. "Tensor X-ray Optical Properties of the Bromate Ion". *Acta. Cryst. A* 41 (1985), pp. 133–142.

[66] K. D. Finkelstein, Q. Shen, and S. Shastri. "Resonant x-ray diffraction near the iron K edge in hematite $\alpha-Fe_2O_3$". *Phys. Rev. Lett.* 69.1612 (1992).

[67] V. E. Dmitrienko. "Forbidden reflections due to anisotropic x-ray susceptibility of crystals". *Acta. Cryst. A* 39 (1983), pp. 29–35.

[68] P. P. Kernavanoisa N. andDeen and L. Paolasini. "Pressure device for reso-
      nant magnetic x-ray scattering". *Rev. Sci. Instrum.* 76.083909 (2005).

[69] D. Collins S. P.and Laundy and A. Stunault. "Anisotropic resonant diffrac-
      tion fro $HoFe_2$". *J. Phys.: Condens. Matter* 13 (2001), pp. 1891–1905.

[70] A. F. Goncharov. "Raman spectroscopy at high pressure". *International
      Journal of Spectroscopy* 2012.617528 (2012).

[71] N. Tateiwa and Y. Haga. "Evaluations of pressure-transmitting media for
      cryogenic experiments with diamond anvil cell". *Rev. Sci. Instrum.* 80.123901
      (2009).

[72] M. Imada, A. Fujimori, and Y. Tokura. "Metal-insulator transitions". *Rev.
      Mod. Phys.* 70.1039 (1998).

[73] L. C. Gupta2006. "Superconductivity and magnetism and their interplay in
      quaternary borocarbides RNi_2B_2C". *Adv. Phys.* 55.691 (2006).

[74] K. Yasuzuka S.and Murata. "Recent progress in high-pressure studies on
      organic conductors". *Sci. Technol. Adv. Mater.* 10.024307 (2009).

[75] E. Fradkin, S. A. Kivelson, and J. M. Tranquada. "*Colloquium*: Theory of
      intertwined orders in high temperature superconductors". *Rev. Mod. Phys.*
      87.457 (2015).

[76] G. R. Stewart. "Superconductivity in iron compounds". *Rev. Mod. Phys.*
      83.1589 (2011).

[77] L. Li et al. "Coexistence of magnetic order and two-dimensional supercon-
      ductivity at $LaAlO_3$/$SrTiO_3$ interfaces". *Nat. Phys.* 7 (2011), pp. 762–766.

[78] T. Koyama et al. "Frustration-Induced Valence Bond Crystal and Its Melting
      in Mo_3Sb_7". *Phys. Rev. Lett.* 101.126404 (2008).

[79] V. H. Tran, W. Miiller, and Z. Bukowski. "Observation of a Spin Gap in the
      Normal State of Superconducting Mo_3Sb_7". *Phys. Rev. Lett.* 100.137004
      (2008).

[80] J.-Q. Yan et al. "Flux growth and physical properties of Mo_3Sb_7 single
      crystals". *Phys. Rev. B* 87.104515 (2013).

[81] J.-Q. Yan et al. "Fragile structural transition in Mo_3Sb_7". *Phys. Rev. B*
      92.064507 (2015).

[82] C. Candolfi et al. "Conventional *s*-wave pairing in the presence of spin
      fluctuations in superconducting Mo_3Sb_7 from specific heat measurements".
      Phys. Rev. B 77.092509 (2008).

[83] R. Khasanov et al. "Muon-spin rotation measurements of the penetration
      depth of the Mo_3Sb_7 superconductor". *Phys. Rev. B* 78.014502 (2008).

[84] B. Wiendlocha et al. "Superconductivity of Mo_3Sb_7 from first principles".
      Phys. Rev. B 78.060507(R) (2008).

[85] G. Z. Ye et al. "Competition of superconductivity with the structural transition in Mo_3Sb_7". *Phys. Rev. B* 94.224508 (2016).

[86] C. Candolfi et al. "Low-temperature galvanomagnetic, magnetic, and thermoelectric properties of $Mo_3Sb_{7-x}Te_x$ (x=0.0, 0.3, 1.0, 1.6, and 1.8)". *Phys. Rev. B* 79.235108 (2009).

[87] A. Palmer, D. M. Silevitch, Yejun Feng, Yishu Wang, R. Jaramillo, A. Banerjee, Y. Ren, and T. F. Rosenbaum. "Sub-Kelvin magnetic and electrical measurements in a diamond anvil cell with in situ tunability". *Review of Scientific Instrument* 86.093901 (2015). DOI: 10.1063/1.4929861.

[88] M. A. de Vries, A. C. Mclaughlin, and J.-W. G. Bos. "Valence Bond Glass on an fcc Lattice in the Double Perovskite Ba_2YMoO_6". *Phys. Rev. Lett.* 104.177202 (2010).

[89] S. P. Cramer et al. "Molybdenum x-ray absorption edge spectra. The chemical state of molybdenum in nitrogenase". *J. Am. Chem. Soc.* 98.1287 (1976).

[90] M. Hanawa et al. "Superconductivity at 1 K in $Cd_2Re_2O_7$". *Phys. Rev. Lett.* 87.187001 (2001).

[91] S. Tongay et al. "Magnetic properties of MoS_2: Existence of ferromagnetism". *Appl. Phys. Lett.* 101.123105 (2012).

[92] V. Shamrai et al. "Low-temperature properties of $Ga_{0.5}Mo_2S_4$". *J. Low Temp. Phys.* 49.123 (1982).

[93] A. K. Rastogi et al. "An electron-phonon contribution to the stoner enhancement in $GaMo_4X_8$ compounds". *J. Low Temp. Phys.* 52.539 (1983).

[94] W. M. Lomer. "Electronic Structure of Chromium Group Metals". *Proc. Phys. Soc. (London)* 80.489 (1962).

[95] B. Wiendlocha and M. Sternik. "Electronic Structure of Chromium Group Metals". *Intermetallics* 53.150 (2014).

[96] W. L. McMillan. "Transition Temperature of Strong-Coupled Superconductors". *Phys. Rev.* 167.331 (1968).

[97] C. Candolfi et al. "Spin Fluctuations and Superconductivity in Mo_3Sb_7". *Phys. Rev. Lett.* 99.037006 (2007).

[98] B. Keimer et al. "From quantum matter to high-temperature superconductivity in copper oxides". *Nature* 518 (2015), pp. 179–186.

[99] Q. Si, R. Yu, and E. Abrahams. "High-temperature superconductivity in iron pnictides and chalcogenides". *Nat. Rev. Mater.* 1.16017 (2016).

[100] J.-G. Cheng et al. "Pressure Induced Superconductivity on the border of Magnetic Order in MnP". *Phys. Rev. Lett.* 114.117001 (2015).

[101] G. P. Felcher. "Magnetic structure of MnP". *J. Appl. Phys.* 37 (1966), pp. 1056–1058.

[102]   M. Matsuda et al. "Pressure dependence of the magnetic ground states in MnP". *Phys. Rev. B* 93.100405(R) (2016).

[103]   G. P. Felcher et al. "Magnetic structure of iron monophosphide". *Phys. Rev. B* 3.3046 (1971).

[104]   A. Kallel, H. Boller, and E. F. Bertaut. "Helimagneism in MnP-type compounds: MnP, FeP, CrAs, and $CrAs1 - xSb_x$ mixed crystals". *J. Phys. Chem. Solids* 35 (1974), pp. 1139–1152.

[105]   K. Selte et al. "Magnetic structures and properties of $V_{1-t}Mn_tAs$". *Acta Chem. Scand.* A30 (1976), pp. 8–14.

[106]   K. Selte et al. "Magnetic structures and properties of $Mn_{1-t}Co_tAs$". *Acta Chem. Scand.* A30 (1976), pp. 468–474.

[107]   K. Selte et al. "Magnetic structures of $Mn_{0.95}Fe_{0.05}As$". *Acta Chem. Scand.* A30 (1976), pp. 671–672.

[108]   S. Haneda et al. "High spin-low spin transition in $MnAs_{1-x}P_x(x=0.075)$". *J. Phys. Soc. Jpn* 42 (1977), pp. 31–35.

[109]   I. L. A. Delphin et al. "Structural and magnetic properties of $Cr_{1-t}Ni_tAs$, $Mn_{1-t}Ni_tAs$ and $Fe_{1-t}Ni_tAs$". *Acta Chem. Scand.* A32 (1978), pp. 179–185.

[110]   K. Selte et al. "Magnetic structures and properties of $Mn_{1-t}Cr_tAs(0 < t \leqslant 0.40)$". *Acta Chem. Scand.* A32 (1978), pp. 653–657.

[111]   H. Fjellvåg et al. "Magnetic properties of transition metal substituted MnP". *J. Phys. Chem. Solids* 45 (1984), pp. 709–718.

[112]   H. Fjellvåg et al. "Structural and magnetic properties of $Mn_{1-t}Cr_tAs_{1-x}P_x$". *Acta Chem. Scand.* A42 (1988), pp. 214–225.

[113]   E. E. Rodriguez et al. "Noncollinear spin-density-wave antiferromagnetism in FeAs". *Phys. Rev. B* 83.134438 (2011).

[114]   W. Wu et al. "Superconductivity in the vicinity of antiferromagnetic order in CrAs". *Nat. Commun.* 5.5508 (2014).

[115]   H. Kotegawa et al. "Superconductivity of 2.2K under pressure in helimagnet CrAs". *J. Phys. Soc. Jpn* 83.093702 (2014).

[116]   L. Keller et al. "Pressure dependence of the magnetic order in CrAs: A neutron diffraction investigation". *Phys. Rev. B* 91.020409(R) (2015).

[117]   N. F. Berk and J. R. Schrieffer. "Effect of ferromagnetic spin correlations on superconductivity". *Phys. Rev. Lett.* 17 (1966), pp. 433–435.

[118]   Y. Feng et al. "Pressure-Tuned Spin and Charge Ordering in an Itinerant Antiferromagnet". *Phys. Rev. Lett.* 99.137201 (2007).

[119]   Y. Feng et al. "Order parameter fluctuations at a buried quantum critical point". *Proc. Natl. Acad. Sci.* 109 (2012), pp. 7224–7229.

[120] J. Wang et al. "Pressure tuning of competing magnetic interactions in inter-metallic $CeFe_2$". *Phys. Rev. B* 86.014422 (2012).

[121] Y. Feng et al. "Direct probe of Fermi surface evolution across a pressure-induced quantum phase transition". *Phys. Rev. B* 91.155142 (2015).

[122] D. F. McMorrow et al. "X-ray scattering study of the interplay between magnetism and structure in CeSb". *J. Phys.: Condens. Matter* 9 (1997), pp. 1133–1148.

[123] H. C. Walker et al. "Femtoscale magnetically induced lattice distortions in multiferroic $TbMnO_3$". *Science* 333 (2011), pp. 1273–1276.

[124] L. Dobrzynski and A. F. Andresen. "On the magnetic double helical structure in MnP- and MnAs-based alloys". *J. Magn. Magn. Mater.* 82 (1989), pp. 67–76.

[125] T. Yamazaki et al. "Novel Magnetic Chiral Structures and Unusual Temperature Hysteresis in the Metallic Helimagnet MnP". *J. Phys. Soc. Jpn* 83.054711 (2014).

[126] N. Doiron-Leyraud et al. "Fermi-liquid breakdown in the paramagnetic phase of a pure metal". *Nature* 425 (2003), pp. 595–599.

[127] T. Chatterji et al. "The ground state of NaV_2O_5". *Solid State Commun.* 108 (1998), pp. 23–26.

[128] T. Chatterji et al. "High-energy non-resonant X-ray magnetic scattering from $EuAs_3$". *Solid State Commun.* 131 (2004), pp. 713–717.

[129] P. G. Perkins, A. K. Marwaha, and J. J. P. Stuart. "The band structure and magnetic properties of some transition-metal phosphides. II. V, Cr and Mn monophosphides". *Theoret. Chim. Acta.* 59 (1981), pp. 569–583.

[130] K. Tajima, Y. Ishikawa, and H. Obara. "Neutron scattering studies of the ferro to spiral transition in MnP". *J. Magn. Magn. Mater.* 15–18 (1980), pp. 373–374.

[131] A. Schröder et al. "Onset of antiferromagnetism in heavy-fermion metals". *Nature* 407 (2000), pp. 351–355.

[132] O. Stockert et al. "Two-Dimensional Fluctuations at the Quantum-Critical Point of $CeCu_{6-x}Au_x$". *Phys. Rev. Lett.* 80.5627 (1998).

[133] B. Roessli et al. "Chiral Fluctuations in MnSi above the Curie Temperature". *Phys. Rev. Lett.* 88.237204 (2002).

[134] Y. Shen et al. "Structural and magnetic phase diagram of CrAs and its relationship with pressure-induced superconductivity". *Phys. Rev. B* 93.060503(R) (2016).

[135] P. Monthoux and G. G. Lonzarich. "Magnetic interactions in a single-band model for the cuprates and ruthenates". *Phys. Rev. B* 71.054504 (2005).

[136] M. Sigrist. "Introduction to unconventional superconductivity". *AIP Conf. Proc.* 789 (2005), pp. 165–243.

[137] P. W. Anderson et al. "The Physics Behind High-Temperature Superconducting Cuprates: The "Plain Vanilla" Version Of RVB". *J. Phys. Condens. Matter* 16 (2004), R755–R769.

[138] B.J Kim et al. "Phase-Sensitive Observation of a Spin-Orbital Mott State in Sr_2IrO_4". *Science* 323 (2009), pp. 1329–1332.

[139] S. Yip. "Noncentrosymmetric superconductors". *Annu. Rev. Condens. Matter Phys.* 5 (2014), pp. 15–33.

[140] S. Sachdev. "Kagomé and triangular-lattice Heisenberg antiferromagnets: Ordering from quantum fluctuations and quantum-disordered ground states with unconfined bosonic spinons". *Phys. Rev. B* 45.21 (1992).

[141] B. S. Shastry and B. Sutherland. "Exact ground state of a quantum antiferromagnt". *Physica B* 108.1069 (1982).

[142] J. S. Gardner, M. J. P. Gingras, and J. E. Greedan. "Magnetic pyrochlore oxides". *Rev. Mod. Phys.* 82.53 (2010).

[143] G. Ferey et al. "Magnetic pyrochlore oxides". *Rev. Chim. Miner.* 23.474 (1986).

[144] E. Lhotel et al. "Fluctuations and All-In–All-Out Ordering in Dipole-Octupole $Nd_2Zr_2O_7$". *Phys. Rev. Lett.* 115.197202 (2015).

[145] K. Tomiyasu et al. "Emergence of Magnetic Long-range Order in Frustrated Pyrochlore $Nd_2Ir_2O_7$ with Metal–Insulator Transition". *J. Phys. Soc. Jpn.* 81.034709 (2012).

[146] H. Sagayama et al. "Determination of long-range all-in-all-out ordering of Ir^{4+} moments in a pyrochlore iridate $Eu_2Ir_2O_7$ by resonant x-ray diffraction". *Phys. Rev. B* 87.100403(R) (2013).

[147] W. G. Witczak-Krempa et al. "Correlated quantum phenomena in the strong spin-orbit regime". *Annu. Rev. Condens. Matter Phys.* 5 (2014), pp. 57–82.

[148] D. Mandrus et al. "Continuous metal-insulator transition in the pyrochlore $Cd_2Os_2O_7$". *Phys. Rev. B* 63.195104 (2001).

[149] K. Matsuhira et al. "Metal–Insulator Transition in Pyrochlore Iridates $Ln_2Ir_2O_7$ (Ln = Nd, Sm, and Eu)". *J. Phys. Soc. Jpn.* 76.043706 (2007).

[150] K. Matsuhira et al. "Metal–Insulator Transition in Pyrochlore Oxides $Ln_2Ir_2O_7$". *J. Phys. Soc. Jpn.* 80.094701 (2011).

[151] K. Ueda et al. "Pressure and magnetic field effects on metal-insulator transitions of bulk and domain wall states in pyrochlore iridates". *Phys. Rev. B* 92.121110 (2015).

[152]   Z. Tian et al. "Field-induced quantum metal–insulator transition in the py-rochlore iridate $Nd_2Ir_2O_7$". *Nat. Phys.* 12 (2016), pp. 134–138.

[153]   M. Sakata et al. "Suppression of metal-insulator transition at high pressure and pressure-induced magnetic ordering in pyrochlore oxide $Nd_2Ir_2O_7$". *Phys. Rev. B* 83.041102(R) (2011).

[154]   F. F. Tafti et al. "Pressure-tuned insulator to metal transition in $Eu_2Ir_2O_7$". *Phys. Rev. B* 85.205104 (2012).

[155]   T. Kondo et al. "Quadratic Fermi node in a 3D strongly correlated semimetal". *Nat. Commun.* 6.10042 (2015).

[156]   E.-G. Moon et al. "Non-Fermi-Liquid and Topological States with Strong Spin-Orbit Coupling". *Phys. Rev. Lett.* 111.206401 (2013).

[157]   H. Shinaoka et al. "Pyrochlore Iridates: All-in–All-out Magnetic Ordering and Non-Fermi-Liquid Properties". *Phys. Rev. Lett.* 115.156401 (2015).

[158]   J.J. Ishikawa, E.C.T. O'Farrell, and S. Nakatsuji. "Continuous transition be-tween antiferromagnetic insulator and paramagnetic metal in the pyrochlore iridate $Eu_2Ir_2O_7$". *Phys. Rev. B* 85.245109 (2012).

[159]   N. A. Bogdanov et al. "Magnetic state of pyrochlore $Cd_2Os_2O_7$ emerging from strong competition of ligand distortions and longer-range crystalline anisotropy". *Phys. Rev. Lett.* 110.127206 (2013).

[160]   M. Hanawa et al. "Structural phase transition in the superconducting py-rochlore oxide $Cd_2Re_2O_7$". *J. Phys. Chem. Solids* 63 (2013), pp. 1027–1030.

[161]   K. Arai et al. "Structural transition in the pyrochlore superconductor $Cd_2Re_2O_7$ observed by Re nuclear quadrupole resonance". *J. Phys.: Condens. Matter.* 14 (2002), pp. L461–L466.

[162]   Z. Hiroi et al. "High-Pressure Study on the Superconducting Pyrochlore Oxide $Cd_2Re_2O_7$". *J. Phys. Soc. Jpn.* 71 (2002), pp. 1553–1557.

[163]   G. Schuck et al. "Crystal growth, structure, and superconducting properties of the β-pyrochlore KOs_2O_6". *Phys. Rev. B* 73.144506 (2006).

[164]   Y. Okamoto et al. "Breathing Pyrochlore Lattice Realized in A-Site Ordered Spinel Oxides $LiGaCr_4O_8$ and $LiInCr_4O_8$". *Phys. Rev. Lett.* 110.097203 (2013).

[165]   Y. Tanaka et al. "Novel Phase Transitions in the Breathing Pyrochlore Lat-tice: ^{7}Li-NMR on $LiInCr_4O_8$ and $LiGaCr_4O_8$". *Phys. Rev. Lett.* 113.227204 (2014).

[166]   Y. Okamoto et al. "Magnetic Phase Diagram of the Breathing Pyrochlore Antiferromagnet $LiGa_{1-x}In_xCr_4O_8$". *J. Phys. Soc. Jpn.* 84.043707 (2015).

[167] T. Haku et al. "Low-energy excitations and ground-state selection in the quantum breathing pyrochlore antiferromagnet $Ba_3Yb_2Zn_5O_{11}$". *Phys. Rev. B* 93.220407(R) (2016).

[168] O. Benton and N. Shannon. "Ground State Selection and Spin-Liquid Behaviour in the Classical Heisenberg Model on the Breathing Pyrochlore Lattice". *J. Phys. Soc. Jpn.* 84.104710 (2015).

[169] L. Savary et al. "Quantum spin ice on the breathing pyrochlore lattice". *Phys. Rev. B* 94.075146 (2016).

[170] H. Tsunetsugu. "Theory of antiferromagnetic Heisenberg spins on a breathing pyrochlore lattice". *Prog. Theor. Exp. Phys.* 2017.033I01 (2017).

[171] H. C. Gupta et al. "Lattice dynamic investigation of the zone center wavenumbers of the cubic $A_2Ti_2O_7$ pyrochlore". *J. Raman Spectrosc.* 32 (2001), pp. 41–44.

[172] S. C. V. Raman and G. R. Rendall. "Birefringence patterns in diamond". *Proc. Indian Acad. Sci.* A19 (1944), pp. 265–273.

[173] H. Jasbeer et al. "Birefringence and piezo-Raman analysis of single crystal CVD diamond and effects on Raman laser performance". *J. Opt. Soc. Am. B* 33.3 (2016).

[174] C. A. Kendziora et al. "Goldstone-mode phonon dynamics in the pyrochlore $Cd_2Re_2O_7$". *Phys. Rev. Lett.* 95.125503 (2005).

[175] T. Hasegawa et al. "Raman Scattering in KOs_2O_6". *Phys. Rev. B* 77.064304 (2008).

[176] J. Schoenes et al. "Phonons and crystal structures of the β-pyrochlore superconductors KOs_2O_6 and $RbOs_2O_6$ from micro-Raman spectroscopy". *Phys. Rev. B* 77.134515 (2008).

[177] S. Saha et al. "High-pressure Raman and x-ray study of the spin-frustrated pyrochlore $Gd_2Ti_2O_7$". *Phys. Rev. B* 74.064109 (2006).

[178] S.-W. Han, J. S. Gardner, and C. H. Booth. "Structural properties of the geometrically frustrated pyrochlore $Tb_2Ti_2O_7$". *Phys. Rev. B* 69.024416 (2004).

[179] D. V. S. Saha S.and Muthu et al. "Low-temperature and high-pressure Raman and x-ray studies of pyrochlore $Tb_2Ti_2O_7$: Phonon anomalies and possible phase transition". *Phys. Rev. B* 79.134112 (2009).

[180] Y. Feng et al. "Magnetism, structure, and charge correlation at a pressure-induced Mott-Hubbard insulator-metal transition". *Phys. Rev. B* 83.035106 (2011).

[181] Yishu Wang, Yejun Feng, J.-G. Cheng, W. Wu, J. L. Luo, and T. F. Rosenbaum. "Spiral Magnetic Order and Pressure-Induced Superconductivity in Transition Metal Compouns". *Nature Communications* 7.13037 (2016). DOI: 10.1038/ncomms13037.

[182] H. Takatsu et al. "Comparative study of low-temperature x-ray diffraction experiments on $R_2Ir_2O_7$ (R = Nd, Eu, and Pr)". *Phys. Rev. B* 90.235110 (2014).

[183] M. J. Harris et al. "Geometrical frustration in the ferromagnetic pyrochlore $Ho_2Ti_2O_7$". *Phys. Rev. Lett.* 79.13 (1997).

[184] S. T. Bramwell and M. J. Harris. "Frustration in Ising-type spin models on the pyrochlore lattice". *J. Phys.: Condens. Matter.* 10 (1999), pp. L215–L220.

[185] Y. Tokiwa et al. "Quantum criticality in a metallic spin liquid". *Nat. Mater.* 13 (1999), pp. 356–359.

[186] R. Schaffer et al. "Recent progress on correlated electron systems with strong spin-orbit coupling". *Rep. Prog. Phys.* 79.094504 (2016).

[187] J. I. Yamaura and Z. Hiroi. "Low temperature symmetry of pyrochlore oxide $Cd_2Re_2O_7$". *J. Phys. Soc. Jpn.* 71 (2002), pp. 2598–2600.

[188] T. Bzdusek, A. Rüegg, and M. Sigrist. "Weyl semimetal from spontaneous inversion symmetry breaking in pyrochlore oxides". *Phys. Rev. B* 91.165105 (2015).

[189] C. H. Sohn et al. "Optical spectroscopic studies of the metal-insulator transition driven by all-in–all-out magnetic ordering in 5d pyrochlore $Cd_2Os_2O_7$". *Phys. Rev. Lett.* 115.266402 (2015).

[190] J. W. Harter et al. "A parity-breaking electronic nematic phase transition in the spin-orbit coupled metal $Cd_2Re_2O_7$". *Science* 356 (2017), pp. 295–299.

[191] V. Kozii and L. Fu. "Odd-Parity Superconductivity in the Vicinity of Inversion Symmetry Breaking in Spin-Orbit-Coupled Systems". *Phys. Rev. Lett.* 115.207002 (2015).

[192] Y. Wang et al. "Topological superconducting phases from inversion symmetry breaking order in spin-orbit-coupled systems". *Phys. Rev. B* 93.134512 (2016).

[193] S. Calder et al. "Spin-orbit-driven magnetic structure and excitation in the 5d pyrochlore $Cd_2Os_2O_7$". *Nat. Commun.* 7.11651 (2016).

[194] A. E. Taylor et al. "Spin-Orbit Coupling Controlled J = 3/2 Electronic Ground State in 5d^3 Oxides". *Phys. Rev. Lett.* 118.207202 (2017).

[195] H. Shinaoka, Miyake T., and S. Ishibashi. "Noncollinear magnetism and spin-orbit coupling in 5d pyrochlore oxide $Cd_2Os_2O_7$". *Phys. Rev. Lett.* 108.247204 (2012).

[196] I. M. Lifshitz. "Anomalies of electron characteristics of a metal in the high pressure region". *Sov. Phys. JETP* 11 (1960), pp. 1130–1135.

[197] A. Kitaev. "Anyons in an exactly solved model and beyond". *Ann. Phys.* 321 (2006), pp. 2–111.

[198] J. G. Rau, E. K.-H. Lee, and H.-Y. Kee. "Spin-Orbit Physics Giving Rise to Novel Phases in Correlated Systems: Iridates and Related Materials". *Annu. Rev. Condens. Matter Phys.* 7 (2016), pp. 195–221.

[199] I. Tüttö and A. Zawadowski. "Theory of Raman scattering of superconducting amplitude modes in charge-density-wave superconductors". *Phys. Rev. B* 45.4842 (1992).